行政院國家科學委員會專題研究計畫成果報告

雙 Tsuji 燃燒器火燄交互作用之實驗與數值分析（1/2）

The Theoretical and Experimental Studies on Flame Interaction of Dual Tsuji Burners (1/2)

計畫編號 NSC 90-2212-E-009-048

執行期限九十年八月一日至九十一年七月三十一日

主持人：陳俊勳教授　　交通大學機械系教授

中文摘要

本計畫主要針對多孔單圓柱上之火焰吹離現象作一完整的數值模擬及實驗觀測。在數值模擬中，本研究將四步化學反應機構導入陳俊勳及翁芳柏兩位教授先前所發展的燃燒模式中。至於實驗儀器方面則包括了風洞及多孔燒結之圓柱形燃燒器，然後吾人就可利用這些儀器來觀察圓柱形燃燒器上的火焰行為，而所探討的參數則包括了進氣速度與注油面積。另一方面，吾人可用數位攝影機將火焰結構及其轉變過程錄下，然後便可將前半面圓柱噴油情況下的火焰依其特性分成四個區域（I-IV），而在全圓柱噴油下則只能分成兩區（V 及 VI）。在第 I 至 III 區中，當進氣速度等於 0.41m/sec 時可在圓柱形燃燒器上形成一個包封火焰，至於火焰所呈現的顏色則是這些區域間的主要差異。在第 IV 及第 V 區中，當進氣速度增加時，包封、尾流、吹離及晚期尾流火焰就會依次出現，另外，由於在全圓柱注油時燃料可以直接噴入吹離火焰中，因此其出現區間遠較前半圓柱噴油時為大。至於第 VI 區的吹離火焰則是緊跟在包封火焰後隨即出現，且在其兩者間並無尾流火焰的存在，之後當進氣速度繼續增加時，尾流火焰仍會接在吹離火焰後出現。另一方面，在數值模擬中，包封擴散火焰、尾流火焰、吹離火焰和尾流火焰在火焰完全熄滅前會隨著進氣速度的增加而依序出現，而當進氣速度為 1.05m/sec 時可產生一 1.7D 的最大吹離高度，且此高度可一直保持至進氣速度達到 1.09m/sec 時，然後吹離

高度就會隨著進氣速度的增加而逐漸降低，而此一過程即可視為回火。再者，吾人可發現當這些吹離火焰出現時，於圓柱形燃燒器的後方並無迴流的產生，至於當進氣速度介於 1.13 至 1.15m/sec 之間時會出現一個從吹離火焰轉變到尾流火焰的過渡過程，然後當進氣速度達到 1.16m/sec 後尾流火焰又會再度出現，而當進氣速度超過 2.12m/sec 時火焰便會熄滅。另外，吾人亦會針對火焰吹離及落回之現象作一詳細的解釋。最後，吾人會將實驗所得結果與計算結果相比較以確認兩者之趨勢是一致的。

關鍵詞：Tsuji 燃燒器、吹離火焰、逆流擴散火焰、四步化學反應機構、進氣速度

ABSTRACT

This project aims at simulating and observing the flame lift-off phenomena over a porous cylinder (Tsuji burner). In the numerical simulations, this investigation applies a four-step chemical kinetics mechanism to implement the original combustion model developed by Chen and Weng (1990). The experiment builds apparatus, comprised of a wind tunnel and a porous sintered cylindrical burner, to observe flame behaviors over a cylindrical burner. The parametric studies are based on the variation of the inflow velocity and the fuel ejection area. The flame configurations and transition processes are recorded by digital video. The flame characteristics can be categorized into four regions (I-IV) in the front half cylinder fuel-ejection case and two regions (V and VI) in the full cylinder fuel-ejection case. In regions I, II, and III, at an initial inflow velocity of 0.41 m/s, an envelope flame is established around the cylindrical burner. The main difference among these regions is the flame colors. In regions IV and V, as the inflow velocity increases, envelope, wake, lift-off, and late wake flames appear in that order. Fuel can be directly ejected into the lift-off flame in the case of full cylinder fuel-ejection, so its survival domain is much larger than that in the case of front half cylinder fuel-ejection. In region VI, the lift-off flame appears directly following the envelope flame, and no wake flame is observed between them. Then, as the inflow velocity increases, the wake flame again appears after the lift-off flame. At the simulation, as U_{in} increases, the envelope diffusion flame, wake flame, lift-off flame, and wake flame appear in order before complete extinction. The maximal lift-off height is 1.7D when U_{in} is 1.05 m/sec, and this height is maintained up to U_{in} =

1.09 m/sec. Then, the height declines gradually as the inflow velocity increases, which process can be regarded as flashback. No recirculation flow exists behind the cylindrical burner for these lift-off flames. A transition from lift-off to wake flame occurs between 1.13 to 1.15 m/sec. The wake flame reappears at U_{in} = 1.16 m/sec. The flame is extinguished completely when U_{in} > 2.12 m/sec. The flame' s lifting and dropping back is explained. Finally, the experimental results compare with the computational results to reveal that their trends are the same.

Keywords: Tsuji burner, lift-off flame, counterflow diffusion flame, four-step chemical kinetics mechanism, inflow velocity

CONTENTS

LIST OF TABLES

LIST OF FIGURES

NOMENCLATURE

A Cross-sectional area of the test section

A_{Burner} Surface area of the half cylinder

a Length of cross-sectional area of the test section

$\overline{B}$ Frequency factor for gas phase reaction

b Width of the cross-sectional area of the test section

$\overline{C}$ Mole fraction

$\overline{C}_p$ Mean specific heat at constant pressure

D Cylinder diameter

D_i Inner diameter of the cylinder

D_o Outer diameter of the cylinder

$\overline{D}$ Dimensional species diffusivity

Da Damkohler number

E Activation energy

$-f_w$ Nondimensional fuel-ejection rate

H Flame lift-off height

h Enthalpy

k_s Flame stretch rate

$\overline{K}$ Equilibrium constant

$\overline{k}$ Rate constant

L_c Length of the cylinder

Le Lewis number, $\overline{\alpha}/\overline{D}$

M Molecular weight

M_{air} Air molecular weight at STP condition

M_T Third-body

N Number of chemical species

$\overline{P}$ Pressure

Pr Prandtl number, $\overline{\nu}/\overline{\alpha}$

Q_{air} Flux of the air

Q_{fuel} Flux of the fuel

R Cylinder radius

R^0 Universal gas constant

Re Reynolds number

S Fuel-ejection area

$\overline{T}$ Temperature

$\overline{T}_a$ Ambient temperature

T_w Nondimensional wall temperature

T^* Reference temperature

t Time

U_{in} Inflow (air) velocity

$\bar{u}$ Velocity in x-direction

$\bar{V}$ Diffusion velocity

$\bar{v}$ Velocity in y-direction

v_w Fuel ejection velocity on cylinder surface

$\bar{x}$ Distance in x-direction

Y Mass fraction of species

$\bar{y}$ Distance in y-direction

z Third-body efficiency

Greek

α^* Thermal diffusivity at T^*

ì Dynamic viscosity

μ^* Dynamic viscosity at T^*

ñ Density

ρ^* Density at T^*

ρ_{air} Density of air

$\dot{w}_i$ Reaction rate

ν Kinematic viscosity

ë Thermal conductivity

$ë^*$ Thermal conductivity at T^*

Overhead

¯ Dimensional quantities

Superscript

* Reference state

Subscript

CH_4 Fuel

O_2 Oxidizer

H_2O Water vapor

CO_2 Carbon dioxide

CO Carbon monoxide

N_2 Nitrogen

H_2	Hydrogen
H	Hydrogen radical
w	Surface of the porous cylinder
a	Ambient
rc	Reference
n, t	Normal and tangential to cylinder surface
i	Species, it may represent CH_4, O_2, CO_2, H_2O, CO, H_2, N_2, or H

CHAPTER 1 INTRODUCTION

1.1 Motivation

This work is motivated by the findings on the appearance of a lift-off flame over a Tsuji burner within a certain range of incoming flow velocity in the recent experimental works of Wang (1998). He concentrated mainly on elucidating the flame structures as a function of distance between a pair of Tsuji burners (dual porous cylindrical burners). To the author's best knowledge, this is the only experiment in which a lift-off flame was observed over a porous cylindrical burner. Although Gollahalli and Brzustowski's experiments (1973) also determined a lift-off flame, the burner was a porous sphere rather than a cylindrical one. Chen (1993), Jiang et al. (1995), Huang (1995), Chiu and Huang (1996), and Huang and Chiu (1997) numerically addressed droplet gasification and combustion problems in a forced convection environment. All of them identified the flame lift-off phenomena above a fuel droplet. These phenomena suggest the possibility of a lift-off flame's existing over a Tsuji burner.

The two-dimensional combustion model developed by Chen and Weng (1990) simulates the stabilization and extinction of a flame over a porous cylindrical burner. Their model employs the one-step overall chemical reaction mechanism. According to their results, the envelope, side, and wake flames appear in order, as the incoming flow velocity was gradually increased. When a limiting value is reached, the flame is completely blown-off from the porous cylinder without the appearance of any lift-off flame. Apparently, this prediction contradicts the

experimental observation of Wang (1998), mentioned previously, perhaps because of simplified combustion chemistry. Therefore, this study presents a multi-step chemical reaction mechanism to incorporate the original combustion model and further examine the corresponding flame behaviors over a Tsuji burner. Besides, a corresponding experimental set-up, shown in Fig. 1, is built to investigate the counterflow flame behaviors over a Tsuji burner and thereby duplicate the appearance of the lift-off flame. To compromise with the complexity of multi-dimensional and irregular flow field, a four-step methane oxidation chemical kinetics (Paczko et al. [1986], Peters and Kee [1987], Seshadri and Peters [1990], and Rogg [1991 and 1993]) is adopted here without loss of the important role of the chemistry in this reacting flow.

1.2 Literature Survey

Tsuji and Yamaoka (1967, 1969, and 1971) and Tsuji (1982) conducted a series of experiments on the counterflow diffusion flame in the forward stagnation region of a porous cylinder. The corresponding extinction limits, aerodynamic effects as well as temperature and stable-species-concentration fields of this flame were studied in detail. They identified two flame extinction limits. The blow-off, caused by a large velocity gradient (flame stretch), occurs because of chemical limits on the combustion rate in the flame zone. Substantial heat losses cause thermal quenching at a low fuel-ejection rate. However, no lift-off flame phenomenon was reported.

The primary configuration in Chen and Weng's numerical study (1990) included a flame over a porous cylinder. That study used the two

dimensional, complete Navier-Stokes momentum, energy, and species equations with one-step finite-rate chemical kinetics. Their parametric studies were based on the Damkohler number (Da), a function of flow velocity, and the dimensionless fuel-ejection rate ($-f_w$), respectively. As Da was decreased, the envelope, side, and wake flames appeared in order. However, reducing $-f_w$ caused the envelope flame to directly become a wake flame, and no side flame was observed.

Sung et al. (1995) utilized a non-intrusive laser-based technique to elucidate the extinction of a laminar diffusion flame over a Tsuji burner. A laminar diffusion flame, unlike a premixed flame, is sensitive to variation in the imposed strain rate. It becomes thinner with an increasing rate, leading to an increase of reactant leakage, progressively reducing flame temperature, and eventually causing extinction of laminar diffusion flame. Zhao et al. (1997) utilized USED CARS to measure the temperature distribution in the forward stagnation and wake regions of a methane/air counterflow diffusion flame. A pyrolysis zone of methane is observed on the fuel-rich side of the stagnation region. The temperature of the flame in the wake region was found to exceed that in the stagnation region, implying that some intermediate products were not completely burnt in the latter region.

Considerable progress has been made during the preceding two decades in predicting the structure of steady counterflow diffusion flames using complicated mechanisms of reaction. The GAMM at Heidelberg was the most famous workshop, and it included five different groups. Dixon-Lewis et al. (1984) used one-dimensional complex chemical

reaction mechanisms, with detailed transport properties, to predict the structure of the counterflow diffusion flame in the front stagnation region of a Tsuji burner. Their computed results did not fully match Tsuji and Yamaoka's measurements (1971). They claimed that the reason for the discrepancies was the overall system's failing to behave as a straightforward boundary layer flow, and that a full solution requires a two-dimensional flow treatment.

Dreier et al. (1986) and Sick et al. (1990) made CARS measurements and one-dimensional calculations to elucidate the counterflow diffusion flame over a porous cylinder. Their chemical reaction mechanism involved 250 elementary steps (including reverse reactions) and 39 species. As in the last reference, they found that discrepancies between experimental and computational results followed from applying boundary layer approximations. Apparently, the flow field must be completely represented in two dimensions.

Wohl et al. (1949) stated that, as the burning velocity of the premixed flame equals the speed of the local fluid at which the laminar flame velocity is maximum, the diffusion flame can be lifted. Vanquickenborne and Van Tiggelen (1966) developed this idea further. This theory is fundamentally based on complete molecular-scale mixing, which occurred in the unburnt flow upstream from the flame stabilization point. Kalghatgi (1984) introduced the following relationship to explain the occurrence of lift-off flames.

$$\frac{\rho_e S_{L,\max} h}{\mu_e} = 50\left(\frac{\nu_e}{S_{L,\max}}\right)\left(\frac{\rho_e}{\rho_\infty}\right)^{1.5},$$

where $S_{L,\ max}$ is the maximum laminar flame velocity, occurring near stoichiometric conditions for hydrocarbons. The flame structure in the stabilization region was fuel/air fully premixed.

1.3 Scope of the Present Study

This study modifies the combustion model of Chen and Weng (1990). The modification involves adopting a four-step chemical reaction mechanism and a finer distribution of grid size to catch up the flame lift-off phenomena over a Tsuji burner immersed in a uniform air stream by ejecting methane uniformly from the surface of a cylinder. Besides, this work sets up an apparatus for duplicating the lift-off flames and examines the appearances of the flames. The main configuration is similar to that employed in the experiments of Tsuji and Yamaoka (1967, 1969, and 1971). The parameters of interest are the inflow air velocity (U_{in}) and fuel-ejection area (S) of the cylindrical burner. This work aims to determine under which conditions the lift-off flame can exist, and then to analyze the detail of the structure of such a flame. A physical interpretation is presented to clarify the mechanisms of the flame's lifting and dropping back. This work also involves flow visualization of the flame behaviors recorded by a digital video. These data are directly compared with the corresponding numerical simulation, and vice versa.

CHAPTER 2 MATHEMATICAL MODEL

The proposed mathematical model, including assumptions, normalization procedure, and the corresponding solution methodology, including a grid generation technique and algorithm, are similar to those developed by Chen and Weng (1990). The major improvements are that the chemical kinetics adopts a four-step mechanism rather than a one-step mechanism, and the grid cell is much smaller due to the current availability of far superior computational tools. Consequently, this section emphasizes the description of the four-step chemical kinetics mechanism, the corresponding formulae and boundary conditions.

2.1 Nondimensional Conservation Equations

Table I summarizes the nondimensional continuity, x-momentum, y-momentum, and energy conservation equations used in this work. For the details of the normalization procedure, please refer to Chen and Weng (1990). The dimensional energy and species equations and the representations of corresponding properties are as follows.

Energy equation

$$\bar{\rho}\bar{u}\frac{\partial \bar{T}}{\partial x}+\bar{\rho}\bar{v}\frac{\partial \bar{T}}{\partial y}=\frac{1}{\bar{C}_p}\left\{\frac{\partial}{\partial x}\left[\bar{\lambda}\frac{\partial \bar{T}}{\partial x}\right]+\frac{\partial}{\partial y}\left[\bar{\lambda}\frac{\partial \bar{T}}{\partial y}\right]\right\}-\frac{1}{\bar{C}_p}\sum_{i=1}^{N}\bar{h}_i\bar{\dot{w}}_i \qquad (1)$$

Species equation

$$\bar{\rho}\bar{u}\frac{\partial Y_i}{\partial x}+\bar{\rho}\bar{v}\frac{\partial Y_i}{\partial y}=\frac{\partial}{\partial x}\left[\bar{\rho}\bar{D}_i\frac{\partial Y_i}{\partial x}\right]+\frac{\partial}{\partial y}\left[\bar{\rho}\bar{D}_i\frac{\partial Y_i}{\partial y}\right]+\bar{\dot{w}}_i,\ \text{i=1, 2.,.N-1} \qquad (2)$$

where i represents CH_4, O_2, CO_2, H_2O, CO, H_2, and H, and the mass fraction of nitrogen, an inert gas, is given by,

$$Y_{N_2} = 1 - \sum_{i=1}^{N-1} Y_i \tag{3}$$

The equation of state of an ideal gas is used to close Eqs. (1) and (2):

$$\frac{\overline{P}}{\overline{r}} = R^{\circ}\overline{T}\sum_{i=1}^{N}\frac{Y_i}{\overline{M}_i} \tag{4}$$

The above equation is rewritten to express $\overline{r}$ as,

$$\overline{r} = \frac{\overline{P}}{R^{\circ}\overline{T}\sum_{i=1}^{N}\frac{Y_i}{\overline{M}_i}} \tag{5}$$

Rogg' s approximation (1993) is adopted to express the diffusion flux:

$$\overline{r}\overline{D}_i\frac{\partial Y_i}{\partial \overline{x}} = \frac{\overline{l}/\overline{C}_p}{Le_i}\frac{\partial Y_i}{\partial \overline{x}} \tag{6}$$

The Lewis numbers used in this numerical calculation are (Seshadri and Peters [1990] and Bilger et al. [1991]),

$$Le_{CH_4} = 0.97,\quad Le_{O_2}=1.11,\quad Le_{H_2O}=0.83,\quad Le_{CO_2}=1.39,$$

$$Le_{H_2}=0.3,\quad Le_{H}=0.18,\quad Le_{CO}=1.1,\quad Le_{N_2}=1.0 \tag{7}$$

A new correlation is introduced to express $\frac{\overline{l}}{\overline{C}_p}$ in Eq. (6) (Seshadri and Peters [1990] and Rogg [1991]).

$$\frac{\overline{l}}{\overline{C}_p} = 2.58\times10^{-5}\left(\frac{T}{298}\right)^{0.7} \tag{8}$$

The mean specific heat at constant pressure, $\overline{C}_p$, can be written as (Kee et al., 1999A),

$$\overline{C}_p = \sum_{i=1}^{N}\overline{C}_{p_i}Y_i \tag{9}$$

NASA thermochemical polynomials (Andrews and Biblarz [1981] and Kee et al. [1999B]) are used to estimate the specific enthalpy, $\overline{h}_i$, and the specific heat, $\overline{C}_{p_i}$, for each species,

$$\overline{C}_{p_i} = a_{1,i} + a_{2,i}\overline{T} + a_{3,i}\overline{T}^2 + a_{4,i}\overline{T}^3 + a_{5,i}\overline{T}^4 \tag{10}$$

$$\overline{h}_i = a_{1,i}\overline{T} + \frac{a_{2,i}}{2}\overline{T}^2 + \frac{a_{3,i}}{3}\overline{T}^3 + \frac{a_{4,i}}{4}\overline{T}^4 + \frac{a_{5,i}}{5}\overline{T}^5 + a_{6,i} \tag{11}$$

The Prandtl number is defined as,

$$\Pr = \frac{\overline{m}\overline{C}_p}{\overline{l}} = \frac{\overline{m}}{\overline{l}/\overline{C}_p} \tag{12}$$

Thus, the dynamic viscosity can be expressed as,

$$\overline{m} = \Pr \times \frac{\overline{l}}{\overline{C}_p} \tag{13}$$

In this work, Pr = 0.75 is selected following Smooke and Giovangigli (1991), and Eq. (8) is introduced as follows.

$$\overline{m} = 0.75 \times 2.58 \times 10^{-5} \left(\frac{\overline{T}}{298} \right)^{0.7} \tag{14}$$

The dynamic viscosity can thus be expressed as,

$$\overline{m} = 3.586985197 \times 10^{-7} \times \overline{T}^{0.7} \tag{15}$$

2.2 Chemical Kinetics

The four-step chemical reaction mechanism used in this study is reduced from a 58-step C_1 mechanism that was used by Miller et al. (1984). The four-step reaction (Paczko et al. [1986], Peters and Kee [1987], and Rogg [1993]), involving seven reacting species and nitrogen, are presented below.

$CH_4 + H_2O + 2H \quad CO + 4H_2$ (I)

$CO + H_2O \quad CO_2 + H_2$ (II)

$2H + M_T \quad H_2 + M_T$ (III)

$3H_2 + O_2 \quad 2H_2O + 2H$ (IV)

The mass production rate for each species (Rogg, 1991) can be expressed as,

$$\overline{\dot{w}_{CH_4}} = -\overline{M}_{CH_4}\overline{\dot{w}_I} \tag{16}$$

$$\overline{\dot{w}_{O_2}} = -\overline{M}_{O_2}\overline{\dot{w}_{IV}} \tag{17}$$

$$\overline{\dot{w}_{CO_2}} = \overline{M}_{CO_2}\overline{\dot{w}_{II}} \tag{18}$$

$$\overline{\dot{w}_{H_2O}} = -\overline{M}_{H_2O}\left(\overline{\dot{w}_I} + \overline{\dot{w}_{II}} - 2\overline{\dot{w}_{IV}}\right) \tag{19}$$

$$\overline{\dot{w}_{CO}} = \overline{M}_{CO}\left(\overline{\dot{w}_I} - \overline{\dot{w}_{II}}\right) \tag{20}$$

$$\overline{\dot{w}_{H_2}} = \overline{M}_{H_2}\left(4\overline{\dot{w}_I} + \overline{\dot{w}_{II}} + \overline{\dot{w}_{III}} - 3\overline{\dot{w}_{IV}}\right) \tag{21}$$

$$\overline{\dot{w}_H} = -\overline{M}_H\left(2\overline{\dot{w}_I} + 2\overline{\dot{w}_{III}} - 2\overline{\dot{w}_{IV}}\right) \tag{22}$$

$$\overline{\dot{w}_{N_2}} = 0 \tag{23}$$

The rates of reactions (I) (IV) (Peters and Kee, 1987) are derived as follows.

$$\overline{\dot{w}_I} = \overline{\dot{w}_1} + \overline{\dot{w}_2} \tag{24}$$

$$\overline{\dot{w}_{II}} = \overline{\dot{w}_9} \tag{25}$$

$$\overline{\dot{w}_{III}} = \overline{\dot{w}_6} + \overline{\dot{w}_8} + \overline{\dot{w}_{14}} + \overline{\dot{w}_{15}} \tag{26}$$

$$\overline{\dot{w}_{IV}} = \overline{\dot{w}_{10}} + \overline{\dot{w}_{16}} \tag{27}$$

in which $\overline{\dot{w}_1}$, $\overline{\dot{w}_2}$, $\overline{\dot{w}_6}$, $\overline{\dot{w}_8}$, $\overline{\dot{w}_9}$, $\overline{\dot{w}_{10}}$, $\overline{\dot{w}_{14}}$, $\overline{\dot{w}_{15}}$, and $\overline{\dot{w}_{16}}$ can be obtained from Peters and Kee (1987):

$$\overline{\dot{w}_1} = \overline{k}_1\overline{C}_{CH_4}\overline{C}_H \tag{28}$$

$$\overline{\dot{w}_2} = \frac{\overline{k}_2}{\overline{K}_{C12}}\frac{\overline{C}_{H_2O}}{\overline{C}_{H_2}}\overline{C}_{CH_4}\overline{C}_H \tag{29}$$

$$\overline{\dot{w}_6} = \frac{\overline{k}_1 + \overline{k}_2 \dfrac{\overline{C}_{H_2O}}{\overline{C}_{H_2}\overline{K}_{C12}}}{\overline{k}_6\overline{C}_H + \overline{k}_7\overline{C}_{M_T} + \overline{k}_8\overline{C}_{O_2}} \overline{k}_6 \overline{C}_{CH_4} \overline{C}_H{}^2 \tag{30}$$

$$\overline{\dot{w}_8} = \frac{\overline{k}_1 + \overline{k}_2 \dfrac{\overline{C}_{H_2O}}{\overline{C}_{H_2}\overline{K}_{C12}}}{\overline{k}_8\overline{C}_{O_2} + \overline{k}_6\overline{C}_H + \overline{k}_7\overline{C}_{M_T}} \overline{k}_8 \overline{C}_{O_2} \overline{C}_{CH_4} \overline{C}_H \tag{31}$$

$$\overline{\dot{w}_9} = \frac{\overline{k}_9}{\overline{K}_{C12}} \overline{C}_H \left(\frac{\overline{C}_{CO}\overline{C}_{H_2O}}{\overline{C}_{H_2}} - \frac{\overline{C}_{CO_2}}{\overline{K}_{II}} \right) \tag{32}$$

$$\overline{\dot{w}_{10}} = \overline{k}_{10} \overline{C}_H \left(\overline{C}_{O_2} - \frac{\overline{C}_H{}^2 \overline{C}_{H_2O}{}^2}{\overline{C}_{H_2}{}^3 \overline{K}_{IV}} \right) \tag{33}$$

$$\overline{\dot{w}_{14}} = \overline{k}_{14} \overline{C}_H \overline{C}_{O_2} \overline{C}_{M_T} \tag{34}$$

$$\overline{\dot{w}_{15}} = \frac{\overline{k}_{15}}{\overline{K}_{C12}} \frac{\overline{C}_{H_2O}}{\overline{C}_{H_2}} \overline{C}_H{}^2 \overline{C}_{M_T} \tag{35}$$

$$\overline{\dot{w}_{16}} = \overline{k}_{16} \frac{\overline{\dot{w}_8} + \overline{\dot{w}_{14}}}{\overline{k}_{16} + \overline{k}_{17} + \overline{k}_{18} \dfrac{\overline{C}_{H_2O}}{\overline{C}_{H_2}\overline{K}_{C12}}} \tag{36}$$

where,

$$\overline{C}_i = \frac{\overline{\rho} \overline{Y}_i}{\overline{M}_i} \tag{37}$$

$$\overline{C}_{M_T} = \sum_{i=1}^{N} z_i \overline{C}_i \tag{38}$$

The third-body efficiencies for each species (Peters and Kee, 1987) are z_H =1, z_{H_2} =1, z_{O_2} =0.4, z_{H_2O} =6.5, z_{CO} =0.75, z_{CO_2} =1.5, z_{CH_4} =6.54, and z_{N_2} =0.4.

Table II (Warnatz, 1984) shows the rate constants used in Eqs. (28-36). However, some equilibrium constants, such as those in Eqs. 29-33, 35, and 36, are using the ones proposed by Peters and Kee (1987).

$$\overline{K}_{C12} = 0.2657 \overline{T}^{-0.0247} \exp\left(\frac{15130}{R^\circ \overline{T}} \right) \tag{39}$$

$$\overline{K}_{II} = 3.828 \times 10^{-5} \overline{T}^{0.8139} \exp\left(\frac{9839}{R^\circ \overline{T}} \right) \tag{40}$$

$$\overline{K}_{IV} = 11.687\overline{T}^{-0.2467} \exp\left(\frac{11396}{R^{\circ}\overline{T}}\right) \tag{41}$$

Finally, all $\overline{\dot{w}}_i$ s are divided by $\frac{r^{*}U_{in}}{R}$ to yield the nondimensional value, $\dot{w}_i$, for each species.

2.3 Nondimensional Boundary Conditions

The domain of interest can be reduced to a half plane because the two-dimensional flame is assumed to be symmetric with respect to the stagnation streamline ($y = 0$), and Fig. 2 illustrates the boundary conditions.

The surface temperature of the cylindrical burner is maintained constant. The fuel is uniformly ejected from the front half surface of the porous cylinder. Thus, the boundary conditions along the surface are,

$$\mathrm{v_t}=0, \quad \mathrm{v_n}=-\mathrm{f_w}(2/\mathrm{Re})^{0.5}, \quad \mathrm{T_w}=\text{given}, \quad \dot{\mathrm{m}}_\mathrm{w}=\mathrm{v_n}\rho_\mathrm{w} \tag{42}$$

$$\dot{\mathrm{m}}_\mathrm{w}\mathrm{Y_{fw}} = \dot{\mathrm{m}}_\mathrm{w} + \frac{1}{\mathrm{Re\,Pr\,Le}}\mu\frac{\partial \mathrm{Y_f}}{\partial \mathrm{n}}\Big|_\mathrm{w} \tag{43}$$

$$\dot{\mathrm{m}}_\mathrm{w}\mathrm{Y_{ow}} = \frac{1}{\mathrm{Re\,Pr\,Le}}\mu\frac{\partial \mathrm{Y_o}}{\partial \mathrm{n}}\Big|_\mathrm{w} \tag{44}$$

$$\dot{m}_w Y_{iw} = \frac{1}{\mathrm{Re\,Pr}\,Le_i}\dot{m}\frac{\partial Y_o}{\partial n}\Big|_w \quad , \tag{45}$$

where i=CO_2, H_2O, H_2, N_2, H, and CO. If the surface is non-blowing, then the boundary conditions become,

$$\mathrm{v_t}=0, \quad \mathrm{v_n}=0, \quad \mathrm{T_w}=\text{given}, \quad \dot{\mathrm{m}}_\mathrm{w}=0 \tag{46}$$

$$\frac{\partial \mathrm{Y_f}}{\partial \mathrm{n}}\Big|_\mathrm{w}=0, \quad \frac{\partial \mathrm{Y_o}}{\partial \mathrm{n}}\Big|_\mathrm{w}=0, \quad \frac{\partial Y_i}{\partial n}\Big|_w=0 \tag{47}$$

2.4 Numerical Algorithm

The configuration of the flow field, as depicted in Fig. 2, is irregular. Therefore, a body-fitted coordinate system, generated by a grid generation approach, is employed. Accordingly, the physical domain is transformed into a computational domain that consists of the equally spaced, square grids. Weng (1989) detailed the procedure, which is not presented here.

The computational domain is selected to be x_{in} = -7, x_{out} = 13, and y_{wall} = 4. The upstream and downstream positions are determined via several numerical experiments to meet the requirement that applying boundary conditions at these positions should not impact the flame structures. Then, a set of numerical tests is conducted to ensure further that the resultant solutions are grid-independent. Table III presents test results. The cases shown in the first column are the same as those in Fig. 25, which will be discussed later. If the number of cells exceeds 218×115, then the variation of resultant peak temperature, the variable most sensitive to the size of the grid, over the entire computational domain becomes insignificant by the increasing number of grid cells. Therefore, this work uses 218x115 grid cells. The grid is much finer than that, 112×51, used in the earlier study (Chen and Weng, 1990).

CHAPTER 3 Experimental Apparatus Setup

Basically the experimental setup is incorporated with the present combustion model. The experimental setup consists of three major elements in the apparatus, which are the wind tunnel, the porous sintered cylindrical burner and measurement instrumentations. They are described in detail as follows.

3.1 Wind Tunnel

According to the simulation, the tunnel is used to provide a laminar, uniform oxidizer flow to the porous cylindrical burner, and the fuel is injected from the surface of the burner. It is open-circuit and oriented vertically upwards. A schematic configuration of the wind tunnel is shown in Fig. 3. There are five components in the wind tunnel: (1) a blower, (2) a diffuser, (3) flow straightener, (4) a contraction, and (5) a test section. Concepts of making wind tunnel mainly are from Yang et al. (1999).

3.1.1 Blower

The airflow in the tunnel is provided by a variable-speed (frequency controlled) blower (Type TB-201, C-F Company), whose outlet is connected to the main part of the wind tunnel via a flexible 60 cm long and 10 cm diameter plastic ductwork, which the end is coupled to a diameter 346 mm and 75 cm long cylinder, which is designed according as AMCA 210-85 standard (shown in Figs. 4 and 5). The blower is driven by a frame motor, which is controlled by an inverter drive. A

frequency converter (Type M36V2P07, DYNAGEN, J-C Company) is used to control the rotational speed of blower to get the desired velocity. The frequency of the blower and corresponding velocity in test section shown in Fig. 6. In order to avoid the influence of vibration, the base of wind tunnel and blower are separated (shown in Fig. 7).

3.1.2 Diffuser

A 30 cm long diffuser has an inlet cross-section area of 12x12 cm^2 and the outlet one is 40x40 cm^2. The expansion ratio based on area is 1:11.

3.1.3 Flow Straightener

The airflow from diffuser section is really unstable before entering into contraction section. The flow straightener is used to make it more stable. The flow straightener section, which serves to insure that the flow to test section is laminar and uniform over the entire cross-section, consists of honeycomb and screen. The screen is mounted to decrease disturbances and make flow uniform. The honeycomb is added to utilities of the screen, like reducing turbulence effect. With appropriate combinations of screen and honeycomb characteristics and putting them at optimum position, it can achieve the goals mentioned above.

3.1.4 Contraction Section

The test section cross-section area 24x4 cm^2, therefore the contraction ratio over the contraction section is 16.6:1. Its purpose is to promote a uniform field in the test section. The design criteria are

demanded to shorten the duct and reduce boundary layer thickness along the wall as possible.

3.1.5 Test Section

The test section has a cross section area of 24x4 cm^2 and a length of 30 cm. It is made up four sides. In the front and two connecting sides, they are equipped with quartz-glass plates for observation windows. The rear side is made of stainless steel plate for supporting the burner to insert. The downstream of the test section is connected to a diffuser (500 mm), which can reduce the amount of exhaust gases from test section. The vent follows after the diffuser to outdoor. The rear part of the vent can resist high temperature by adhered fins to inside the vent as heat exchanger. The outside of vent is connected with water-cooling system, including cooler, water tank and pump (shown in Fig. 8). The front part of inside the vent is also very important since a series of instruments are set up to measure the heat release rate (see Sec. 3.3.6).

Measurement in the test section is to confirm the velocity uniform and stable. There are four sets of pitot tubes and a fixed static pressure hole in the front of the burner of the test section (see Figs. 9 and 10). Change different connection in four pitot tubes in order (fixed the static pressure hole) under the same inflow velocity after a long time. If the pressure difference is closely equal, it means that the flow is uniformity and stabilization (see Fig. 11).

3.2 Porous Sintered Cylindrical Burner

3.2.1 Burner Structure

The requirement of experimental burner has to be able to sustain the high temperature. It is designed to have inner and outer parts, respectively. The outer part of burner is a replaceable porous sintered stainless steel (20, 40, 70 μm pores, respectively) with a length of 40 ± 0.5 mm. Its inner diameter is 20 ± 0.5 mm, and an outer diameter 30 ± 0.5 mm (see Figs. 12 and 13). The advantage of this design is that the burner replacement can be easily performed whenever clogging or damage on the porous burner surface occurs due to burning for a long time. The inner of the burner is a cylindrical brass rod (see Fig. 14) with an internal water-cooling groove and fuel supply groove. The outer part is screwed on the inner part. The internal water flow is used to cool the burner to prevent damage from the porous surface structure. The cooling device of the burner includes a water tank, pump, cooler and connected-piping (shown in Fig. 8).

3.2.2 Burner Equipped to Test Section

There are two parameters (half fuel-ejection surface and full fuel-ejection surface respectively) to be measured. Therefore, for the front half side cylinder surface fuel-ejection condition, coating several thin layers of high temperature resistant paint on the backward portion of the burner surface in order to prevent the fuel ejection into the wake region.

(1) The painted surface needs to dry at least 2 hours.

(2) Screwing the burner into the insert and mounting the burner closely to the wall of test section. Connecting the cooling water and fuel pipelines to the burner.

(3) Noticing to adjust the burner so that the uncoated burner surface is facing the direction of the airflow.

(4) In addition, it's important to test whether there is any leakage from the painting surface of the burner. Instead of fuel pipe to air or nitrogen piping, and then immerse the burner into a water container and open a valve to let gas flow to observe whether there are bubbles from the painted surface.

Methane (CH_4, 99.99%) is used as the fuel, and its flow is controlled and measured by a flow meter. A digital mass flow controller (Type MC-2100E, LINTEC, shown in Fig. 15) is controlled by high capability of microprocessor inside. The sensor flow rate signals and command signals are digitized by 16 bit A/D converter to process and operate inside CPU (including: temperature compensation, linearity compensation and control signals operations), and then transformed flow rate signals and command signals into analog signals by 16 bit D/A converter. The fuel ejection velocity is calculated by dividing the fuel volumetric flow by the available fuel ejection area of the burner surface.

3.3 Measurement Instrumentations

3.3.1 Nozzle of the AMCA 210-85 Standard

The measurement of inlet velocity at the test section adopts the AMCA 210-85 standard of nozzle-method to measure volume flow rate and then to deduce flow velocity. The standard is adopted to establish uniform methods for laboratory testing of fans and other air moving devices by AMCA (Air Movement & Control Association Inc.). There

are three nozzles (Ø 10, 15, and 30 mm) and four sets of pitot tubes distributed equally inside the cylinder (shown in Fig. 5), which are incorporated to measure local velocity of the cylinder. Then it can get total volume flow rate to deduce velocity of test section by dividing cross section area of test section. The precision is within 3% when velocities are ranged from 0.21 m/sec to 3.3m/sec precision, but it becomes 5% as the velocity is smaller than 0.21 m/sec.

3.3.2 Digital Video

A digital video (Type DCR-TRV17, SONY) is used to record the flame profiles, such as envelope, side, wake flame, and flame lift-off. It is fixed on appropriate position to catch flame variations. The special function applied is night-shoot to record various flames in the dark laboratory. All imagines recorded on the tape of the cassette have to transmit to computer to process. The digital video is connected to computer by IEEE 1394 card, and then imagines processed by Ulead Video Studio software to show a series of flame structures in different velocity regime.

3.3.3 Thermocouples

K-type thermocouple (wire diameter, 1 mm; compensation wire diameter, 0.65 mm) is used to measure the temperature in order to get the corresponding density in the exhausted duct. It is made of Ni-Cr/Al-Ni alloy material, compensation time 1 second and measured temperature up to 1200 ℃. The measured signals are connected to data acquisition device (PC Recorder, M-SYSTEM) to transform analog signals into

digital signals by series port RS-232 to computer with MSRS32-E software.

3.3.4 Pressure Transducer

Pressure drop received from bi-directional pitot tube (see Figs. 16 and 17) in the vent is converted into micro-voltage signal by pressure transducer. Via this procedure, the averaged velocity in the duct can be calculated. And pitot tubes in the test section and in front of the nozzles of the cylinder are also measured by the pressure transducer (Type PF-MPS2, POUNDFUL).

3.3.5 Oxygen Analyzer and Pretreatment System

Oxygen analyzer (Mode 755A O_2 Analyzer, shown in Fig. 18) is used to measure oxygen consumption in the vent. It should be calibrated and zeroed before testing, using 99.99% pure nitrogen as the zero gas and the air as the span gas, which is composed of 21% oxygen and 79% nitrogen (all gases produced by J-R Gas Company). Exhausted gas should be filtered and cooled completely in the pretreatment section to avoid high temperature and other suspended grains to damage the analyzer. It may reduce oxygen concentration and result data unstable. The pretreatment system is constructed of two sets of series glass wool filter, a membrane filter, and a cooler and micro pump to introduce gas inlet (shown in Fig. 19). The whole schematic piping arrangement of pretreatment system is shown in Fig. 20. The measured signals are connected to data acquisition device (PC Recorder, M-SYSTEM) to

transform analog signals into digital signals by series port RS-232 to computer with MSRS32-E software.

3.3.6 Heat Release Rate Measurements

The flame strength is quantified by the heat release rate. Such measurement is carried out in the exhausted duct, which includes: (1) K-type thermocouple, (2) a robust bi-directional probe connected to pressure transducer and (3) a gas sampling probe connected to the oxygen analyzer with the pretreatment section (shown in Fig. 21). These instruments are used to measure the temperature, velocity and oxygen concentration of oxygen of product gas, respectively. All the sampling gases are first introduced to the pretreatment section for cooling and filtering before they go into the oxygen analyzer. The whole schematic configuration can be seen in Fig. 22. The signals will be collect via a data acquisition system, and then these data are handled by 586-PC to calculate the heat release rate.

3.4 Procedure of the Experimental Operation

(1) Calibrate the instruments to make sure the stabilization and accuracy of their performance before performing the experiment.

(2) It usually takes times for completion of warm-up for the apparatuses that include blower, mass flow controller and O_2 analyzer.

(3) The blower has to be operated for 30 minutes until the flow uniformity and stabilization are achieved. Stabilization depends on pressure difference (four pitot tubes vs. 1 fixed static pressure

hole) in front of the burner in the test section is stable.

(4) The digital mass flow controller needs to be operated for 15-30 minutes because of thermal-sensor type to let flow more accurate.

(5) Check if any fuel gases leak from pipelines by suds. It's very important procedure for this achromatic, flavorless, toxic and flammable fuel.

(6) Turn on the flow of cooling system to the burner and vent.

(7) Start the computer program (software: MSRS32-E) used to collect desired data via a data acquisition system (PC Recorder), and then these data are handled by 586-PC using software to calculate the heat release rate.

(8) Turn on the ignition device, which is produced spark by the way of 3000 volt high voltage. Turn it off until the flame is established. Note that remember to ignite first before let the fuel input, or it may be exploded.

(9) Open the valve of methane fuel vase and keep inlet pressure up to 8 psi, then turn on the stop valve of mass flow controller. The alarm light of mass flow controller displays green that means fuel passes pipelines to the burner. Set the fuel flow rate to the desired amount in liters per minutes. First choose a certain fixed value of fuel supply to the burner, and then increase slowly the airflow velocity in order to get various flame types. It means that change the inflow velocity as a parameter under a fixed fuel ejection rate.

(10) In the low velocity regime, the envelope flame is expected to

appear. Once the flame is established, permit several minutes for the flame to stabilize or adjust the blower speed if necessary. Next, gradually increase the inflow velocity to get the other types of flames. After that, change another value of fixed fuel ejection rate to continue this step. Then it can gain profiles of different fuel flow rate as increasing inflow velocity.

(11) Digital video is fixed to position to get the same observation view of test section to catch all images from testing.

(12) Using the front half side fuel-ejection of cylinder surface instead of full side fuel-ejection burner to repeat the procedure from (8)-(10) steps.

(13) Also change the fuel ejection rate as a parameter under a fixed flow velocity. Carry out the similar procedure as the above.

3.5 Uncertainty Level Analysis in the Experiment

Uncertainty analysis is carried out to estimate the uncertainty levels in the experiment. Formulae for evaluating the uncertainty levels in the experiment can be found in several papers (Kline and Mcclintock [1953] and Moffat [1982]) and textbooks (Holman [1989], Fox and McDonald [1994], and Figliola and Beasley [1995]). Accordingly, Table IV summarizes the results of all uncertainty analyses.

3.6 Experimental Repeatability

The procedures for changing the airflow velocities at different fuel ejection velocities were performed three times to ensure experimental repeatability, coincidence, and accuracy. The transition velocity, which

transforms an envelope flame into a wake flame, is a critical value to investigate the flame behaviors. Table V presents the transition velocities for flame transformation from an envelope flame into a wake flame in the front half cylinder fuel-ejection system as a function of fuel ejection velocity. The table records three measured data, their average, and the error at each fuel ejection velocity. The error is defined as the ratio of the absolute difference between the maximum and minimum values of the three data to their average. Generally, the errors are within an acceptable range (maximum of 6.82%) and the repeatability is quite good except at three points, v_w = 1.12 cm/s, 1.23 cm/s, and 1.68 cm/s. These points are near the two demarcation lines, between region I (v_w = 0.9 ~ 1.12 cm/s) and II (v_w = 1.23 ~ 1.57 cm/s), and region II and III (v_w = 1.68 ~ 2.8 cm/s). The errors are inevitably large at these critical points. The flame transition processes and their corresponding characteristics are detailed below.

CHAPTER 4 RESULTS AND DISCUSSION

I. Simulation Part

The gaseous fuel used is methane (CH_4) and the ambient oxidizer is air. The basic thermodynamic and transport property data, summarized in Table VI, are taken from Chen and Weng (1990) to enable a fair comparison later.

4.1 Comparison with Related Experiments and Simulations

The present combustion model is first validated by comparing the predicted results with the pertinent measurements of Tsuji (1982) and the simulation results of Chen and Weng (1990). Then, the predictions are compared with the measurements and calculations of Dreier et al. (1986).

Figure 23 presents the comparison, by plotting the blow-off limit as functions of $-f_w$ (nondimensional fuel ejection rate) and $2U_{in}/R$ (flame stretch rate, k_s). Notably, this line in Tsuji's experiment (1982) represents a demarcation line at which the flame is transformed from an envelope flame to a wake flame instead of being extinguished. The predictions of this report are quite close to Tsuji's experiments (1982) in the regions of high fuel-ejection rate and low stretch rate. Generally, the prediction is much better than that of Chen and Weng (1990), implying that the prediction that is based on a four-step chemical mechanism is indeed better than the one that uses a one-step overall chemical mechanism. However, in the domain of $0.2 < -f_w < 0.77$ and $91 < 2U_{in}/R < 376$, a significant discrepancy exists between the present predictions and Tsuji's measurements (1982). Notably, this domain is

located at a transition from the very small fuel ejection rate to the large flame stretch rate. The discrepancy may be attributable to two factors stated in Chen and Weng (1990): the first is the three dimensional effect in the experimental configuration and the other one is a chemical effect. The blow-off that results from a low fuel ejection rate is very close to that obtained experimentally because it is governed mainly by the thermal quenching of the cylinder surface. The geometric effect should be minor in this branch. However, aerodynamic and chemical limitations greatly affect the blow-off mechanism due to flame stretch. For a given $2U_{in}/R$ (~ 376), in the higher $-f_w$ regime (> 0.77), the four-step chemical effect seems appropriate even if the fluid flow dominates, whereas it does not suffice to describe the reactions in the regime of lower $-f_w$, such as $0.2 < -f_w < 0.77$. Better agreement with measurements initiates from $-f_w = 0.5$ and $2U_{in}/R = 128$, which occurs much earlier than that of Chen and Weng (1990), and continuously improves thereafter.

Figure 24 compares the predictions in this study to the measurements and calculations of Dreier et al. (1986). This figure depicts the temperature distribution along the forward stagnation line, where the forward stagnation point is at x = 0. The presented combustion model reproduces the data measured in the experiment, and the agreement is much better than that of their own numerical computation. The temperature profile on the oxidizer side predicted in this study shifts to the left of the experimental data by around 0.2mm; the shift is approximately 0.5mm on the fuel side. Considering the experimental uncertainties, the agreement can be regarded as excellent.

Now, Table VII and Fig. 25 directly compare with the results of Chen and Weng's simulations (1990). Table VII depicts the inflow velocity range for flames with different appearances. Notably, no side flame exists in this study, whereas neither lift-off nor subsequent late wake flames appeared in Chen and Weng (1990). Apparently, the application of a four-step mechanism shows its influence on flame structures. This table reveals that applying a one-step overall chemical reaction can yield a stronger flame if still survives, implying that the corresponding gross reaction rate is higher. However, the velocity range of flame that exists in this work can be sustained to a higher inflow velocity, indicating that the intermediate species generated in the multi-step reactions may play important roles near the extinction limit.

A case in the envelope flame is selected to demonstrate flame structures using different chemical mechanisms, because finding the same type of flame in both cases simultaneously at the same inflow velocity and blowing rate is difficult; see Table VII. The inflow velocity and $-f_w$ are fixed at 0.75m/sec and 0.5, respectively.

Figures 25-A1 and 25-B1 are the combinations of resultant isotherms and streamlines for Chen and Weng's (1990) and the present works, respectively. The flame is seen to be smaller and the flame temperature is lower in this study. The maximum temperature is approximately 1860K, but it is about 2300K in the last reference. As mentioned previously, if an envelope flame can exist, the net reaction rate is lower by using a multi-step chemical kinetics.

The streamline patterns in both studies (Figs. 25-A1 and 25-B1) are very similar since the flame, but not chemistry, directly influences fluid

flow. The recirculation flow region behind the cylinder in Chen and Weng (1990) is smaller than that in this study because the stronger flame in their work generated a higher pressure due to thermal expansion, which depresses the recirculation zone behind the cylinder further.

Figures 26-A1 and 26-B1 present the methane and oxygen mass fraction distributions. Since the reaction rate is slower in this study, the amount of unreacted fuel (CH_4) is expected to be greater, and this fuel can be carried further downstream by convection and diffusion. Again, this study involves seven reacting species, whereas Chen and Weng (1990) considered only two. Accordingly, the mass fraction of fuel in this work is further diluted since more species are used.

The above three comparisons indicate that the proposed combustion model, which considers a four-step chemical mechanism, can generate a satisfactory solution for the various structures of flames over a single Tsuji burner. The parametric studies are presented below after these comparative works.

4.2 Parametric Studies

The varying parameters are the oxidizer flow velocity (U_{in}) and the fuel ejection area (S), respectively, under the specified $-f_w = 0.5$ and R = 1.5 cm. The variation of fuel ejection area (S) is indicated by angle. For example, 180° implies that the fuel ejection area covers the forward half of cylindrical surface, and 360° covers the whole surface.

4.2.1 Effects of Oxidizer Flow Velocity (U_{in}) at S=180 °

Increasing U_{in} augments the flame stretch rate, k_s, defined as $2U_{in}/R$. The inflow velocity varies from 0.75 m/s to 2.12 m/s, and Figs. 25, 26, and 27 are used to illustrate the variations and structures of the corresponding flame. Figure 25 displays a series of combinations of isotherms and streamline distributions as a function of U_{in} or k_s. Figure 26 presents the combinations of fuel and oxidizer mass fractions, and Fig. 27 plots the fuel reactivity distributions. In Fig. 27, this work adopts the $\bar{\dot{w}}_{CH_4} = 10^{-4} \frac{g}{cm^3 \cdot \sec}$ contour line as a flame boundary, as presented by Nakabe et. al. (1994).

Figures 25 and 27 show that as the inflow velocity increases, the envelope flame (Fig. 25-B1), wake flame (Figs. 25-B2 and 25-B3), lift-off flame (Figs. 25-B4~B9), and wake flame (Figs. 25-B10 and 25-B11) appear in order before the flame is completely extinguished. Three types of flame exist in the flow field; they are envelope, wake, and lift-off flames. However, the wake flames can be further classified into two categories, transformed from envelope flame or transformed from lift-off flame. Notably, no side flame, which was identified in Chen and Weng (1990), appears in the flow field. This work emphasizes the transition from wake to lift-off and then to wake flame.

4.2.1.1 Envelope Diffusion Flame

An envelope flame surrounds the porous cylinder in the low-speed flow regime. Its velocity is under 0.9m/sec (see Table VII). Case B1 in Fig. 25 belongs to this category.

As shown in Fig. 25-B1, an envelope flame seems to be situated around the front porous cylinder and spreads downstream. The active

reaction zone in Fig. 27-B1 also exhibits this feature. Such a flame is identified as a diffusion flame, whose fuel side can be distinguished from the oxidizer one, as shown in Fig. 26-B1.

In Fig. 25-B1, the maximum temperature along the stagnation streamline (y=0) is about 1860K at x=-1.455. The isotherms above 600K (indicated by dark blue lines) in front of the burner are almost parallel to the cylindrical surface, because of the uniform fuel-ejection rate. The fact is confirmed by Fig. 27-B1, too. Therefore, the flame stand-off distance can be regarded as constant along the fuel supply surface. This uniform fuel supply, in an opposite direction to the flow of the oxidizer, makes the concentration of isotherms on the oxidizer side denser than that on the fuel side in front of the cylinder. Just behind the fuel supply surface, the isotherms are no longer parallel to the surface but are dispersed. The isotherms on the fuel side shift inward at the back of cylinder and reach the line of symmetry to form a closed loop, since no blowing is applied over there. The recirculation flow in the wake region somewhat distort some intermediate isotherms near the rear stagnation area, such as those of T=900, 1200, and 1500K, as depicted in Fig. 25-B1. The isotherms on the oxidizer side initially move outward, and then spread to the wake. Far downstream, where the influence of the flow recirculation is negligible, the temperature gradient in the cross-stream direction is found to exceed greatly that in the direction of the stream.

4.2.1.2 Wake Flame

Increasing the inflow velocity up to 0.9 m/sec (case B2) breaks the flame front away from the front stagnation streamline. The flame front

retreats along the surface until a certain condition is met that it can be stabilized on the rear part of the cylinder; see Figs. 25-B2, 25-B3, 27-B2, and 27-B3. This kind of flame is defined as a wake flame. The wake flames in cases B2 and B3 are generated by the break-up of the envelope flame due to the flame stretch effect, as described below. Such a wake flame exists for between 0.9 and 1.04 m/sec; see Table VII. Two other cases, B10 and B11, are also categorized as a wake flame but with a different formation procedure. These will be discussed after the lift-off flame is described.

As shown in Figs. 25-B2, 25-B3, 27-B2, and 27-B3, the wake flame front does not touch the cylinder surface and it is positioned in front of the rear stagnation point; instead, the quenching effect of a cold wall produces a reaction-frozen zone between the flame and the surface. The break-up of the envelope flame in the porous section of the cylinder causes a fuel-air mixture to exist in that region. The mixture is generated from the impingement of fuel and oxidizer streams. Then, the mixture moves downstream by convection, and is ignited by the reversed hot combustion gas products in the vortex region, as shown in Figs. 26-B2 and 26-B3. The location of the flame front is near the top of the recirculation flow. The recirculation flow not only brings hot gases from downstream to upstream to ignite the mixture but also stabilizes the flame. This behavior resembles that of the bluff-body flame holder in afterburner and ramjet systems.

Figures 26-B2 and 26-B3 indicate that the air and fuel are well mixed before entering the reaction zone, since the flame front is away from the porous section and no fuel is ejected from the rear surface. The

mixture also has time to diffuse to some extent. Consequently, the wake flame front is flat and broadened and presents a premixed flame feature.

4.2.1.3 Lift-off Flame

Unlike that described by Chen and Weng (1990), the wake flame is observed to lift rather than blow-off when the inflow velocity is further increased. When the inflow velocity is raised from 1.04 m/sec (Fig. 25-B3) slightly to 1.05 m/sec (Fig. 25-B4), the wake flame is suddenly transformed into a lift-off flame, which exists between 1.05 and 1.15 m/sec.

Figures 25-B4~B9 indicate that the lift-off flame fronts are not attached to but far from the rear surface of the cylindrical burner. More explicitly, the flame front is behind the rear stagnation point; see Figs. 27-B4~B9. The lift-off height is defined as the stream-wise distance between the rear stagnation point of the cylinder and the flame front, which is the lowest point of the $\bar{\dot{w}}_{CH_4} = 10^{-4} \frac{g}{cm^3 \cdot \sec}$ contour line, as marked in Fig. 27-B4. The lift-off height is found to be 1.7D when the inflow velocity (U_{in}) is 1.05 m/sec (Fig. 27-B4). Thus height retained up to U_{in} = 1.09 m/sec. The height then declines gradually as the inflow velocity increases. At U_{in} = 1.10 m/sec, the height is 1.5D (Fig. 27-B5). The height becomes 1D when U_{in} = 1.12 m/sec (Fig. 27-B6). Notably, no recirculation flow occurs behind the cylindrical burner for these lift-off flames; see Figs. 25-B4 to 25-B6. When U_{in} reaches 1.13 m/sec, as shown in Fig. 25-B7, the vortex begins to reappear. However, the flame front remains behind the rear stagnation point with a lift-off height of 0.6D. Cases B8 and B9 involve similar flame behaviors except that

the lift-off height is reduced to 0.2D. Strictly, the flame in the last three cases (B7, B8, and B9) can be regarded as a transition from the lift-off to the wake flames. Consequently, it exhibits part features of both of these flames. Finally, when the inflow velocity reaches 1.16 m/sec, the wake flame fully reappears (Figs. 25-B10 and 27-B10).

Figure 27 reveals that the active chemical reaction zone of the envelope or wake flame in the half plane originates from the forward stagnation line or the rear surface of the cylinder; is concentrated in a strip, and then extends downstream. A lift-off flame begins the reaction far from the rear surface, and exhibits a V-shaped reaction zone, where the inner branch shifts inward and meets the symmetric line at $y = 0$ and the outer one extends downstream. However, a reaction-frozen zone exists between the burner and the flame front. During the transition stage from the lift-off flame to the wake flame, shown in Figs. 27-B7, 27-B8, and 27-B9, the inner reaction zone retreats from the symmetrical line and shrinks upstream. Meanwhile, the flame front moves upstream and toward the rear surface of the cylindrical burner. Eventually, it disappears when the wake flame is formed again.

As shown in Figs. 26-B4 to B6, a fuel-air mixture exists between the burner and the flame front for a lift-off flame, since the reaction ceases due to the relatively low temperature, between 385K and 400K, there. However, the oxidizer still cannot penetrate into the area just behind the rear surface of the cylinder. As expected, the bottom area of the V-shaped reaction zone exhibits features of a premixed flame.

A transformation process from wake to lift-off flame is described as follows. The balance between the local flow velocity and the flame speed governs the position of wake flame front, a premixed flame. Even near the upper limit of the wake flame (U_{in} = 1.04 m/sec), the flame front in Fig. 27-B3 is not wholly hidden behind the rear surface of the cylinder. Restated, it still can see the incoming cold air stream. As soon as the inflow velocity exceeds the local flame speed, the flame front must retreat downstream to a new stable position. However, it cannot move downward into the recirculation zone since it is full of combustion products. Accordingly, the flame front must now leave the surface and move further downstream. At this moment, no recirculation flow exists. In Chen and Weng (1990), using a one-step overall chemical reaction, it blew-off directly. In this study, however, the intermediate products generated in the four-step reactions apparently sustain the combustion to stabilize the flame front behind the burner and form the lift-off flame, as confirmed by the mass fraction distribution of species H_2 as shown in Fig. 28. The first appeared lift-off flame has the greatest lift-off height. As stated above, a reaction-frozen zone exists between the flame front and the burner. The zone around the line of symmetry is full of gas fuel brought from upstream by convection. Increasing the inflow velocity provides more oxidizer to mix with the unreacted fuel in the reaction-frozen zone to form a flammable mixture in front of the flame front. Therefore, the flame front can propagate upstream with a higher flame speed. The reduction in the lift-off height is not so abrupt because it is resulted from a stronger opposed flow. The flashback process continues as the inflow velocity increases until the lift-off flame front

reaches the rear surface of the burner to form a wake flame again. The critical velocity for forming the wake flame from lift-off is 1.16 m/sec. As mentioned previously, a transition, illustrated by Figs. 27-B7, B8, and B9, occurs between these two flames. Finally, the wake flame can be maintained up to U_{in} = 2.12 m/s, beyond which, the flame is extinguished completely.

The whole process from the envelope to wake, then lift-off, and wake flame again, is verified by the present experimental observation, using a flow visualization technique. Figure 29 displays the corresponding photographs. The experiment is performed to reproduce the predicted flame features obtained by the present combustion model. Finally, prediction and observation follow exactly the same qualitative trends.

4.2.2 Flame Lift-off Phenomena for Large Fuel-ejection Area

This section discusses the computed results to interpret flame lift-off phenomena over a porous cylinder in a high fuel-ejection area. Cases of fuel-ejection over the front three quarters of the cylinder and that over the whole cylinder are considered.

4.2.2.1 Fuel-Ejection from Front Three Quarters of the Cylinder (S=270)

In the case of fuel-ejection over the front three quarters of the cylinder (Fig. 30), the flame lifts in the inflow velocity range of 1.03 m/sec to 1.31 m/sec. The mean flame lift-off height is between 1D to 1.5D, and is similar to that in the case of fuel-ejection over the front half

of the cylinder. The flame lift-off processes are also consistent with those in the case of fuel-ejection from the front half of the cylinder: the wake flame suddenly jumps into the lift-off flame at 1.03m/sec inflow velocity. Then the lift-off flame is sustained at a height of about 1.3D height (Fig. 30-C3) above the Tsuji burner, until the inflow velocity exceeds 1.25 m/sec, when the flame lift-off height is 0.7D. When the inflow velocity is between 1.25 m/sec and 1.32 m/sec, the flame lift-off height gradually falls to zero as the inflow velocity increases. Thus the lift-off flame drops back to a wake flame when the inflow velocity reaches 1.32 m/sec (Fig. 30-C4). Therefore, the flame lift-off range in the case of fuel-ejection over the front three quarters of the cylinder is about three times wider than that in the case of fuel-ejection over the front half of the cylinder.

4.2.2.2 Full Cylinder Surface Fuel-Ejection (S=360 °)

In Fig. 31, the lift-off flame exists at between 1.01 m/sec and 1.39 m/sec inflow velocity range. The average lift-off height of the flame is about 1.3D (Fig. 31-D3), similar to the heights in the front half cylinder and the front three quarter cylinder cases. The wake flame (Fig. 31-D2) is lifted to transform into a lift-off flame when the inflow velocity increases to 1.01 m/sec. The lift-off flame is then sustained at approximately 1.3D above the porous cylinder until the inflow velocity reaches 1.30 m/sec. Gradually increasing the inflow velocity to 1.39 m/sec causes the flame lift-off height slowly to decrease until the lift-off flame is reattached to the porous cylinder. The wake flame reappears (Fig. 31-D4) when the inflow velocity exceeds 1.39 m/sec. In general, a larger fuel-ejection

area gives a wider flame lift-off inflow velocity range (Table VIII). A larger fuel-ejection area yields a higher surviving inflow velocity of the lift-off flame, indicating that the lift-off flame is a premixed flame. However, varying the fuel-ejection area barely influences the flame lift-off height (Table IX).

II. Experimental Part

The combustion experiments adopt three parameters to clarify flame behaviors over a porous cylinder (Tsuji burner). They are inflow (air) velocity (U_{in}) and the fuel ejection velocity (v_w) through two fuel ejection areas (S). The burners have two fuel ejection areas (S) - front half cylinder fuel-ejection (S=180°) and full cylinder fuel-ejection (S=360°). The front half cylinder fuel-ejection (S=180°) burner has several temperature-resistant layers coated onto rear half of the cylinder surface to prevent fuel ejection into the wake region; the fuel ejection area covers the forward cylindrical surface that faces against the incoming flow. The full cylinder fuel-ejection (S=360°) of the burner ejects fuel into the airflow from the entire cylinder. The incoming air velocity ranges from 0.21 m/s to 4.0 m/s. The fuel ejection velocity ranges from 0.9 to 3.14 cm/s for the front half cylinder fuel-ejection burner, and from 1.01 to 1.68 cm/s for the full fuel-ejection burner.

4.3 Front Half Cylinder Fuel-Ejection Burner (S=180°)

4.3.1 Flame Behaviors without Lift-off Phenomenon

Figure 32 graphically defines the flame stand-off distance, flame thickness, attached angle of the wake flame, flame length and flame lift-off height. Those definitions are used to characterize the flame behaviors. The flame stand-off distance and flame thickness are defined in the forward stagnation region of the envelope flame. The flame length is the distance measured from the rear stagnation point of the cylindrical burner to the downstream point of reattachment of the flame

on the line of symmetry. These definitions relate to the data summarized in Table X, which consist four regions described in Fig. 33.

Figure 33 depicts the flame configuration map as functions of inflow and fuel ejection velocities. Each measured point (a mean of three data) on the curve is obtained by fixing the fuel ejection velocity and adjusting the inflow velocity gradually to obtain the specific flame configuration. The curve can be divided into four regions. Each region basically includes an envelope, wake, and lift-off flame or extinction. However, extinction may not be observed because the maximum inflow velocity supplied by a wind tunnel is limited.

In Region I, the fuel ejection velocity is between 0.9 and 1.12 cm/s. If the fuel ejection velocity is below 0.9 cm/s at an initial inflow velocity 0.41 m/s, the flame is unstable and cannot exist because of the quenching effect of the wall. The envelope flames are blue and the subsequent wake flames are the same color, implying that the combustion is fuel-lean burning. Figure 34 shows the sequence of flames, for a fixed fuel ejection velocity of v_w = 1.12 cm/s and U_{in} from 0.41 to 2.06m/s.

At an inflow velocity of 0.41 m/s, a blue envelope diffusion flame is stabilized at a distance of 1.67 mm ahead of the cylinder surface in the forward stagnation region. The thickness of the flame is around 1.7 mm and length of the flame is 2D along the line of symmetry (Fig. 34 (a) and Table X (a)). As the inflow velocity increases to 0.51 m/s, the flame stand-off distance declines to 0.83 mm and the flame length is increased to 2.72D (Fig. 34 (b) and Table X (a)). However, the thickness of the flame is almost constant. An increase in inflow velocity (U_{in}) reduces the Damkohler number (D_a), the ratio of gas residence time to chemical

reaction time. The parameter can indicate a flame stretch effect. Reducing Da by increasing the inflow velocity increases the flame stretch effect.

When inflow velocity is increased to 0.66 m/s, the flame front breaks from the forward stagnation region. The flame front retreats along the cylinder surface until a condition for balance is satisfied. Then, the flame front can stabilize on the rear part of the cylinder. This type of flame is defined as wake flame (Fig. 34 (c)). Increasing the incoming flow velocity reduces the chemical reaction rate in the flame front and thus creates the flame stretch effect. This effect opens up the envelope flame. Since the envelope flame is blown-off from the forward stagnation region, the ejected fuel is mixed with the incoming oxidizer to yield a flammable mixture. The mixture then flows downstream and is subsequently ignited by the hot gas that recirculates behind the cylinder to initiate a reaction that forms the wake flame. The air and fuel are mixed before this mixture enters the reaction zone because the flame front is away from the porous section and no fuel is ejected from the rear surface of the cylinder. Also, the mixture has time to diffuse to some extent. Consequently, the flame front becomes flat and broadened. The wake flame is completely blue, implying that the mixture is in the fuel-lean region. Gradually increasing the inflow velocity shortens the flame length and increases the attached angle (Figs. 34 (c)-(e) and Table X (a)). When the inflow velocity exceeds 2.43 m/s, the flame is completely extinguished from the rear part of the cylinder.

The flame patterns in regions II (v_w from 1.23 to 1.57 cm/s) and III (v_w from 1.68 to 2.8 cm/s), shown in Fig. 33, are the same as those shown

in region I. The variations in flame stand-off distance, flame thickness, attached angle of the wake flame, and flame length with inflow velocity follow the same trend (Tables X (b) and (c)). The major difference is the color of the flames. For example, at a fuel ejection velocity of 1.23 cm/s, the blue envelope flame occurs when the inflow velocity is below 0.76 m/s. Increasing the inflow velocity to 0.76 m/s converts the envelope flame into a wake flame, whose flame front exhibits premixed flame characteristics and its downstream part shows features of a diffusion flame. The downstream diffusion flame zone is separated into an inner luminous yellow zone and an outer blue zone (Fig. 35 (c)). The appearance of the inner yellow zone due to soot production reveals that combustion in the wake flame front and the preceding diffusion flame part do not consume all the fuel, and that the excess fuel allows the downstream burning to become fuel-rich on the fuel side. When the inflow velocity increases to 1.04 m/s, the oxidizer supply rate increases, and mixing improves. Consequently, the combustion is more completed upstream and the whole wake flame is blue (Figs. 35 (e)-(g)).

The difference between regions II and III is that the downstream wake region of the envelope flame in region III is yellow, as illustrated in Figs. 36 (a) and (b). This color indicates that the blowing rate of fuel is so great, especially in the lower inflow velocity regime, that some fuel is not completely burnt out but is convected downstream to make the local burning fuel-rich (Figs. 36 (a)-(b)).

The above experimental observation can be summarized briefly. For a given fuel ejection velocity, the flame stand-off distance decreases and the flame length increases as the velocity of the opposing air

increases, but the flame thickness of the envelope flame is almost constant. The attached angle of a wake flame increases and the flame length decreases as the inflow velocity increases. For a fixed inflow velocity, the flame stand-off distance, flame thickness, and flame length of the envelope flame increase with the fuel ejection velocity.

4.3.2 Lift-off Flame under Front Half Cylinder Fuel-Ejection

A special feature is evident in region IV, where the fuel ejection velocity is between 2.91 and 3.14 cm/s. Performing the same experimental procedure as in the previous three regions causes the flame lift-off phenomenon. For example, when fuel ejection velocity equals 3.02 cm/s, an envelope flame with a yellow tail appears when the inflow velocity is 0.41 m/s (Fig. 37 (a)) because much unreacted fuel is carried downstream, leading to fuel-rich burning there. At an initial inflow velocity of 0.41 m/s, the flame stand-off distance is 2mm, measured from the base surface of cylinder, as presented in Table X (d). Continuously increasing the velocity to 1.00 m/s reduces the flame stand-off distance to 0.8 mm; the flame thickness is also almost invariant. The downstream flame becomes longer and extends into the exhaust part of the wind tunnel because the increased fuel supply makes the combustion more intense. Consequently, no flame length data are available for this case. At U_{in} = 1.39 m/s, the flame front suddenly blows-off from the forward stagnation region, resulting in a wake flame with an attached angle of 118°. Maintaining the same inflow velocity for a short time causes the flame to lift away from the rear surface of the cylinder by visualization, as shown in Fig. 37 (e). Figure 37 (e) includes ten pictures taken at

different times with fixed inflow and fuel ejection velocities. These pictures reveal the characteristics of a turbulent flame with a slightly back-and-forth oscillation. Eventually, the flame drops back to the surface of the cylinder and is converted into a wake flame (termed as a late wake flame) again, whose attached angle is 118° , too. After such a wake flame is stabilized, increasing the inflow velocity slightly to 1.43 m/sec does not alter the wake flame configuration, and no flame lift-off occurs.

In summary, as the inflow velocity increases, the envelope, wake, lift-off, and late wake flame appear in order in this region. However, the surviving inflow velocity domain of the lift-off flame is quite narrow for a given fuel ejection velocity, as shown in Fig. 38.

4.4 Full Cylinder Fuel-Ejection Burner (S=360°)

In this section, the fuel ejection completely covers the cylinder surface rather than the front half, as considered in the preceding section. The test procedures are exactly the same as those in S=180°. Figure 38, like Fig. 33, plots the flame configuration map as functions of inflow and fuel ejection velocities. However, the curve consists of only two regions, regions V and VI.

In region V (v_w = 1.01 to 1.34 cm/s), selects the fuel ejection velocity 1.23cm/s to analyze the flame behaviors. Figure 39 displays photographs of each flame with various inflow velocities. An envelope flame with a yellow tail, depicted in Figs. 39 (a) and (b), exists when the inflow velocity is under 0.8m/s. The fuel on the downstream side is not expected to mix well with air since fuel is supplied through the whole

surface. Therefore, combustion at the downstream tail is fuel-rich burning. The flame stand-off distance declines as the inflow velocity increases, and the flame thickness remains almost constant (Table XI (a)). The combustion becomes more intense since the fuel supply rate is increased, making the flame tail longer and causing it to extend into the exhaust part. As in Table X (d), no flame length data are available, too.

The wake flame appears when the velocity equals 0.8m/s (Fig. 39 (c)). From Table XI (a), the attached angle also increases with inflow velocity (101° at U_{in} = 0.8 m/s and 108° at U_{in} = 1.0 m/s).

The lift-off flame commences to appear when the inflow velocity reaches 1.05 m/s. The base of the lift-off flame can stay longer above the cylinder surface than in region IV in Fig. 33 (Fig. 39 (e-1)). Therefore, the lift-off height can be clearly defined as 2.5mm (Table XI (a)). The height then oscillates for a short period without a predictable frequency (Figs. 39 (e-2) to (e-6)) and finally it stabilizes (Fig. 39 (e-7)) at the stated same lift-off height. The downstream flame includes an inner yellow zone surrounded by a blue zone.

The above flame behaviors are retained as the inflow velocity is increased to 1.21 m/s, before which, the lift-off height is found to be raised (Table XI (a)), and the oscillation frequency increases with the inflow velocity. At U_{in} = 1.21 m/s, the inner yellow zone disappears, and the flame is entirely blue (Fig. 39 (f)).

When U_{in} exceeds 1.21 m/s, both the lift-off height and the frequency decline gradually as the inflow velocity increases. As U_{in} reaches 1.63 m/s, the lift-off flame base drops back to the cylinder again

and becomes a late wake flame. Further increasing the inflow velocity does not cause the lift-off flame to reappear.

The main difference between region VI (Fig. 38), where the fuel ejection velocity ranges from 1.4 to 1.68 cm/s, and region V is that the lift-off flame directly appears after the envelope flame in region VI. Restated, no wake flame is observed between the envelope and lift-off flames in region VI. However, the late wake flame still follows the lift-off flame, as illustrated in Fig. 40, in which the flame configuration changes as a function of the inflow velocity at a fixed fuel ejection velocity of 1.4 cm/s. The envelope flame with a yellow tail is present when the inflow velocity is below 1.06 m/s (Figs. 40 (a)-(c)). Its flame stand-off distance decreases as the inflow velocity increases, but the flame thickness remains almost constant (Table XI (b)) either. When inflow velocity exceeds 1.06 m/s, the envelope flame is broken, and the flame front is directly lifted over the surface of the cylinder without a wake flame's appearance as that in region VI. Thereafter, the process and the variation of lift-off flame are similar to those in region V. When the inflow velocity is increased to 1.24 m/s, the lift-off flame is turned completely blue. The lift-off flame drops back to the cylinder again as the inflow velocity increases to 1.63 m/s.

Another difference is evident between regions V and VI in Fig. 38. The critical velocity to transform into the lift-off flame in region V declines as the fuel ejection velocity increases, but follows an opposite trend in region VI. However, a careful examination of the demarcation line between the envelope and lift-off flames in region VI reveals that this line seems to be extended from the demarcation line of the envelope and

wake flames in region V. Figure 33 verifies this behavior, showing that the critical inflow velocity at which the envelope flame transforms into the wake flame increases with fuel ejection velocity.

4.5 Explanation of Lift-off Flame Behavior

The above observation indicates that the lift-off flame eventually appears irrespective of whether the full or half cylinder fuel ejection is used. Prediction result clarifies that a pair of vortices exist behind the cylinder when the flame is an envelope or a wake flame. The stabilization of a wake flame is well known to depend strongly on the existence of such a vortex. As the inflow velocity increases, the attached angle of the wake flame becomes large, moving the two flame fronts closer together. Accordingly, the high pressures generated in these two reaction zones (or flame fronts) depress the vortices and eventually destroy them. The lift-off flame then appears. The corresponding simulation also shows that no vortex exists when the lift-off flame appears. Apparently, the lift-off flame is a premixed flame, in which the fuel and air are mixed upstream. The position of the lift-off flame front is governed by the balance between the speed of the flame (that propagates toward the rear surface of the cylinder) and velocity of the local fresh mixture that flows in the direction of the air flow. However, the lift-off flame oscillates back-and-forth without a predictable frequency because the balance position changes continuously due to the unavoidable disturbance in the flow field.

From Table XI, the lift-off height increases with the inflow velocity. When the height is sufficiently large the flame front is further away from

the cylinder surface, the vortices are again generated behind the cylinder. Then, the somewhat unstable lift-off flame front is dropped back by the recirculation flow to become a wake flame again (late wake flame).

The fuel supply can be directly ejected into the lift-off flame of the full cylinder fuel-ejection burner. Therefore, its survival domain is much greater than that of the front half cylinder fuel-ejection burner.

4.6 Comparisons with Other Studies

Tsuji and Yamaoka (1967, 1969, and 1971) were the most famous group to study a series of flame behaviors over a porous cylinder. The dimensions of their test section were 18x12x3 cm^3 and the burner diameters were 1.5, 3.0, 4.5, and 6.0 cm; the burner was 3 cm long. The fuels used were propane, city gas, and methane. They focused on flame behaviors in the forward stagnation region of the cylinder and the blow-off mechanisms that convert envelope flames into wake flames as inflow velocity increased. However, they did not continue to increase further the inflow velocity to generate the lift-off flame, which was emphasized in this study.

Table XII compares the critical non-dimensional fuel ejection rate ($-f_w=(v_w/U_{in})*(R_e/2)^{1/2}$) at a specified flame stretch rate ($2U_{in}/R$). Recall that the Reynolds number ($Re=U_{in}R/\nu$) is related to viscosity (ν), which depends strongly on temperature. Tsuji (1982) did not state his chosen value of viscosity. Thus, the present study deduces this value from the available described and measured data from his papers. Table XII indicates that the critical value of $-f_w$ for blow-off in this study is always a little less than that obtained by Tsuji (1982). The difference increases as

the flame stretch rate declines. The possible reasons for the discrepancies might be as follows. The burner and test section in this work are longer and larger than those used by Tsuji (1982). However, the mass flow rate controller for methane supply used here is digital and has a microprocessor; it should be much more precise than an analogue one, especially in a low flow rate regime.

Wang (1998) first identified a lift-off flame over a cylindrical burner. He used a 4 cm long uncoated burner (S=360°) with a diameter of 0.96 cm and LPG as fuel. The fuel ejection velocity was from 0.15 to 1.25 cm/s, and the inflow velocity was up to 5.7 m/s. Although the dimensions of the cylindrical burner and the fuel used in this study differ from those in Wang (1998), the trend, which the critical velocity to transform into the lift-off flame is declined with an increase of fuel ejection velocity for lift-off flame appearance (region V in Fig. 38), is exactly the same in both studies. Also, the flame configurations and the order of appearance in the fuel ejection velocity range of 0.3 to 0.7 cm/s considered by Wang (1998) are the same as those in region V of Fig. 38 in this study. When the fuel ejection velocity exceeds 0.7 cm/s in Wang (1998), the variation trend is similar to that on the left half part of region VI in Fig. 38 in this work. However, Wang (1998) did not further extend the fuel ejection velocity to the right part of region VI in Fig. 38.

4.7 Comparison with Numerical Simulation

The corresponding simulation employs two parameters, inflow velocity and fuel ejection area (S=180°, 270°, and 360°), to elucidate flame lift-off. The result shows that a greater fuel ejection area yields a

wider range of flame lift-off inflow velocity. The experiment determines the same results (Figs. 33 and 38). Figure 41 (U_{in} = 1.03m/sec, v_w = 1.12cm/sec, and S=360 °) shows oscillation of the lift-off flame, with a lift-off height of around 0.55D. As time passes, the wake flame and the lift-off flame appear in turn. Similar results can be clarified in Fig. 41, which is the corresponding transient simulation of Fig. 41. Besides, the oscillation period of the numerical calculation is 0.01sec, which is shorter than that, 0.11sec, experimentally observed. The lift-off height in Fig. 42 is approximately 0.15D, lower than the experimental observation. The predicted phenomena are qualitatively consistent with the observations, but quantitative discrepancies exist between the predicted and observed flame lift-off heights and oscillation frequencies, because the simulation assumes laminar flow, whereas the lift-off flame exhibits turbulent characteristics.

CHAPTER 5 CONCLUSIONS

This study modifies the combustion model developed by Chen and Weng (1990), using a four-step chemical reaction mechanism instead of one-step overall kinetics and a finer distribution of grid cells to catch up the flame lift-off phenomena over a Tsuji burner. Besides, the corresponding experimental apparatus consists of a wind tunnel and a porous sintered cylindrical burner. The wind tunnel is open-circuit and orientated vertically upwards. It is designed to provide a laminar, uniform oxidizing flow over the porous cylindrical burner, from the surface of which fuel is ejected. The burner is designed with inner and outer parts. A digital video, fixed at an appropriate position, records the various flame profiles. The parameters of interest are the inflow air velocity (U_{in}) and fuel-ejection area (S). This report emphasizes occurrence of the lift-off flame, which was unidentified in Chen and Weng (1990) but observed in the experiments of Wang (1998).

The modified combustion model is validated first by comparing the predicted results with the corresponding measurements of Tsuji (1982) and the simulation results of Chen and Weng (1990). Then, it is compared with the related measurements and calculations of Dreier et al. (1986). Generally, the present simulation yields a much better prediction than that of Chen and Weng (1990), implying that the prediction obtained using a four-step chemical mechanism is indeed better than that obtained using a one-step overall chemical mechanism. Also, the proposed combustion model can reproduce the data measured

experimentally by Dreier et al. (1986): the agreement is much better than that of their own numerical results.

In the simulation, as the inflow velocity increases, the envelope, wake, lift-off, and wake flame appear in that order before the flame is completely extinguished. The two wake flames have similar structures but different transformation processes: one is transformation from the envelope flame and the other is transformation from lift-off flame. Envelope flame, which is diffusion flame, exists when the inflow velocity is less than 0.9m/sec. Above that velocity, the flame front breaks away from the front stagnation streamline and retreats along the surface until a certain condition is met that it can be stabilized on the rear part of the cylinder. The flame then becomes a wake flame, whose flame front shows the feature of a premixed flame and which is positioned ahead of the rear stagnation point.

When the inflow velocity increases further to 1.05m/sec, the wake flame is abruptly transformed into a lift-off flame, whose flame front is not attached to but far from the rear surface of the cylindrical burner. The maximum lift-off height is found to be 1.7D when the inflow velocity (U_{in}) is 1.05 m/sec. This height is maintained up to U_{in} = 1.09 m/sec. Then, the height declines gradually as the inflow velocity is increased. No recirculation flow occurs behind the cylindrical burner for these lift-off flames, unlike for the envelope and wake flames. When U_{in} reaches 1.13 m/sec, the vortex starts to reappear. However, the flame front remains behind the rear stagnation point with a lift-off height of 0.6D. The transition process from the lift-off to the wake flame occurs from 1.13 to 1.15 m/sec. The flame during the transition exhibits

some of the features of both flames. Finally, when the inflow velocity reaches 1.16 m/sec, the wake flame fully reappears. Eventually, the flame is completely extinguished at U_{in} > 2.12 m/sec. The entire process from the envelope to wake, then lift-off, and back to wake flame is verified by this experimental observation, made using a flow visualization technique.

In the experiment, the flame behaviors are separated into four regions (I-IV) at S=180°, whereas for S=360°, they are categorized into two regions (V and VI). In regions I, II, and III, at an initial inflow velocity of 0.41 m/s, an envelope diffusion flame is generated around the porous cylinder. For a fixed fuel ejection velocity, the flame stand-off distance decreases and the flame length increases as the inflow velocity increases, due to the enhanced flame stretch effect. The flame thickness of the envelope flame is found to be almost constant. Increasing the inflow velocity to a critical value causes the envelope flame to be blown-off and transformed into a wake flame, whose flame front exhibits premixed flame characteristics and whose downstream part exhibits features of a diffusion flame. The flame length is shortened and flame attached angle increased as inflow velocity increases. The major difference among these three regions is the color of the flames.

In region IV, the envelope flame turns into a wake flame as the inflow velocity increases. Maintaining the same inflow velocity for a short period allows the flame to be lifted away from the rear surface of the cylinder. As the inflow velocity increases, the attached angle of the wake flame increases, moving the two flame fronts closer together. The high pressures generated at these two flame fronts depress the vortices,

and eventually destroy them. Then, the lift-off flame appears. It can maintain a lift-off height over a porous cylinder because of the balance between the speed of the flame toward the rear surface of the cylinder and the velocity of the local fresh mixture in air flow direction. In the experiment, some back-and-forth oscillations of the lift-off flame were observed because the local balance position changes continually. When the inflow velocity exceeds the critical value, the vortices are again present behind the cylinder, and the flame lift-off height gradually declines. Finally, the lift-off flame drops back to a wake flame (late wake flame) again.

In full cylinder fuel-ejection (S=360°), the transformation from the envelope to the wake flame in region V is similar to that in front half cylinder fuel-ejection (S=180°). However, fuel downstream of the envelope flame is not expected to mix well with air, which results in fuel-rich burning in the downstream tail. As inflow velocity increases further, the lift-off flame is generated. The base of lift-off flame can stay longer above the cylinder surface than that in region IV.

In region VI, no wake flame is observed between the envelope and lift-off flames. Another difference between region V and VI is that the critical velocity to transform into the lift-off flame in region V is decreased as the fuel ejection velocity increases, but it follows the opposite trend in region VI. The fuel supply can be directly ejected into the lift-off flame in the case of full cylinder fuel-ejection; consequently, the survival domain is much greater than that of the front half cylinder fuel-ejection.

The formation of a lift-off flame is described briefly. When the inflow velocity exceeds the local flame speed, the wake flame front must

retreat downstream to a new stable position. However, it cannot move inward into the recirculation zone since this zone is full of combustion products. Consequently, the flame front must then leave the surface and shift further downstream. At this moment, no recirculation flow exists. A reaction-frozen zone now exists between the burner and the flame front. When the inflow velocity increases, more oxidizer is supplied to mix with the un-reacted fuel in the reaction-frozen zone to form a flammable mixture in front of the flame front. Therefore, the flame front can propagate upstream with a higher flame speed. The reduction of lift-off height, or flashback, is not so abrupt because it results from a stronger opposed flow. The flashback process continues as the inflow velocity increases until the lift-off flame front reaches the rear surface of the burner to form the wake flame again.

Finally, some suggestions are offered for future extensions of this study. The flow pattern of the flame could be observed by introducing particles (magnesium oxide particles) into the uniform air stream and incorporating a LASER system. This approach would help to visualize the flow field behind the cylinder and confirm the controlling mechanism described above. The temperature distribution should also be measured. One more porous cylinder would be inserted into the test section to study flame interference/interaction phenomena. The flame strength could be quantified by heat release rate, according to the oxygen consumption calorimetry principle.

References

Andrews, J. R. and Biblarz, O. (1981) Temperature Dependence of Gas Properties in Polynomial Form, NPS67-81-001, Naval Postgraduate School, Monterey, California.

Bilger, R. W., Esler, M. B., and Starner, S. H. (1991) On Reduced Mechanisms for Methane-air Combustion, in Reduced Kinetic Mechanisms and Asymptotic Approximations for Methane-air Flames, Chapter 5, p. 86, Springer-Verlag, Berlin.

Chen, C.-H. and Weng, F.-B. (1990) Flame Stabilization and Blowoff Over a Porous Cylinder, *Combustion Science and Technology*, **73**, 427-446.

Chen, W.-S. (1993) Interphase Exchange Phenomena of a Convective Liquid Droplet (Canonical Droplet Theory), Ph. D. Dissertation, National Cheng Kung University, Taiwan.

Chiu, H. H. and Huang, J. S. (1996) Multiple-state Phenomena and Hysteresis of a Combusting Isolated Droplet, *Atomization and Sprays*, **6**, 1-26.

Dixon-Lewis, G., David, T., Gaskell, P. H., Fukutani, S., Jinno, H., Miller, J. A., Kee, R. J., Smooke, M. D., Peters, N., Effelsberg, E., Warnatz, J., and Behrendt, F. (1984) Calculation of the Structure and Extinction Limit of a Methane-Air Counterflow Diffusion Flame in the Forward Stagnation Region of a Porous Cylinder, Twentieth Symposium (International) on Combustion, The Combustion Institute, Pittsburgh, p. 1893-1904.

Dreier, T., Lange, B., Wolfrum, J., Zahn, M., Behrendt, F., and Warnatz, J. (1986) Comparison of CARS Measurements and Calculations of the Structure of Laminar Methane-Air Counterflow Diffusion Flames, *Ber. Bunsenges. Phys. Chem.*, **90**, 1010-1015.

Figliola, R. S., and Beasley, D. E. (1995) Theory and Design for Mechanical Measurements, 2nd Ed., John Wiley and Sons, Canada.

Fox, R. W., and McDonald, A. T. (1994) Introduction to Fluid Mechanics, John Wiley and Sons, Canada.

Gollahalli, S. R. and Brzustowski, T. A. (1973) Experimental Studies on the Flame Structure in the Wake of a Burning Droplet, Fourteenth Symposium (International) on Combustion, The Combustion Institute, Pittsburgh, p. 1333.

Holman, J. P. (1989) Experimental Methods for Engineers, 5th Ed., McGraw-Hill, New York.
Huang, J.-S. (1995) Canonical and Renormalized Theory of Droplets: States, Structures and Laws of Isolated and Interacting Droplets, Ph. D. Dissertation, National Cheng Kung University, Taiwan.
Huang, J.-S. and Chiu, H.-H. (1997) Multistate Behavior of a Droplet in Dilute Sprays, *Atomization and Sprays*, **7**, 479-506.
Jiang, T. L., Chen, W. S., Tsai, M. J., and Chiu, H. H. (1995) A Numerical Investigation of Multiple Flame Configurations in Convective Droplet Gasification, *Combustion and Flame*, **103**, 221-238.
Kalghatgi, G. T. (1984) Lift-off Heights and Visible Lengths of Vertical Turbulent Jet Diffusion Flames in Still Air, *Combustion Science and Technology*, **41**, 17-29.
Kee, R. J., Rupley, F. M., Miller, J. A., Coltrin, M. E., Grcar, J. F., Meeks, E., Moffat, H. K., Lutz, A. E., Dixon-Lewis, G., Smooke, M. D., Warnatz, J., Evans, G. H., Larson, R. S., Mitchell, R. E., Petzold, L. R., Reynolds, W. C., Caracotsios, M., Stewart, W. E., and Glarborg, P. (1999A) Chemkin-III: A Software Package for the Analysis of Gas-phase Chemical and Plasma Kinetics, Reaction Design, San Diego.
Kee, R. J., Rupley, F. M., Miller, J. A., Coltrin, M. E., Grcar, J. F., Meeks, E., Moffat, H. K., Lutz, A. E., Dixon-Lewis, G., Smooke, M. D., Warnatz, J., Evans, G. H., Larson, R. S., Mitchell, R. E., Petzold, L. R., Reynolds, W. C., Caracotsios, M., Stewart, W. E., and Glarborg, P. (1999B) The Chemkin Thermodynamic Database, Reaction Design, San Diego.
Kline, S. J., and Mcclintock, F. A. (1953) Describing Uncertainties in Single-Sample Experiments, *Mechanical Engineering*, **75**, 3-8.
Lee, B. J., Kim, J. S., and Chung, S. H. (1994) Effect of Dilution on the Liftoff of Non-premixed Jet Flames, Twenty-fifth Symposium (International) on Combustion, The Combustion Institute, Pittsburgh, p. 1175.
Miller, J. A., Kee, R. J., Smooke, M. D., and Grcar, J. F. (1984) The Combustion of the Structure and Extinction Limit of a Methane-Air Stagnation Point Diffusion Flame, Western States Section, The Combustion Institute, Paper WSS/CI 84-10.
Moffat, R. J. (1982) Contributions to the Theory of Single-Sample Uncertainty Analysis, *Journal of Fluid Engineering*, **104**, 50-260.
Nakabe, K., Mcgrattan, K. B., Kashiwagi, T., Baum, H. R., Yamashita, H., and Kushida, G. (1994) Ignition and Transition to Flame Spread over

a Thermally Thin Cellulosic Sheet in a Microgravity Environment, *Combustion and Flame*, **98**, 361-374.
Paczko, G., Lefdal, P. M., and Peters, N. (1986) Reduced Reaction Schemes for Methane, Methanol and Propane Flames, Twenty-first Symposium (International) on Combustion, The Combustion Institute, Pittsburgh, p. 739-748.
Peters, N. and Kee, R. J. (1987) The Computation of Stretched Laminar Methane-air Diffusion Flames Using a Reduced Four-step Mechanism, *Combustion and Flame*, **68**, 17-29.
Rogg, B. (1991) Sensitivity Analysis of Laminar Premixed CH_4-air Flames Using Full and Reduced Kinetic Mechanisms, in Reduced Kinetic Mechanisms and Asymptotic Approximations for Methane-air Flames, Chapter 8, p. 159, Springer-Verlag, Berlin.
Rogg, B. (1993) Systematically Reduced Kinetic Mechanisms: Sensitivity Analysis, in Dynamics of Gaseous Combustion, p. 202, American Institute of Aeronautics and Astronautics, Washington D.C..
Seshadri, K. and Peters, N. (1990) The Inner Structure of Methane-air Flames, *Combustion and Flame*, **81**, 96-118.
Sick, V., Arnold, A., Diebel, E., Dreier, T., Ketterle, W., Lange, B., Wolfrum, J., Thiele, K. U., Behrendt, F., and Warnatz, J. (1990) Two-dimensional Laser Diagnostics and Modeling of Counterflow Diffusion Flames, Twenty-third Symposium (International) on Combustion, The Combustion Institute, Pittsburgh, p. 495-501.
Smooke, M. D. and Giovangigli, V. (1991) Formulation of the Premixed and Nonpremixed Test Problems, in Reduced Kinetic Mechanisms and Asymptotic Approximations for Methane-air Flames, Chapter 1, p. 1, Springer-Verlag, Berlin.
Sung, C. J., Liu, J. B., and Law, C. K. (1995) Structural Response of Counterflow Diffusion Flames to Strain Rate Variations, *Combustion and Flame*, **102**, 481-492.
Tsuji, H. and Yamaoka, I. (1967) The Counterflow Diffusion Flame in the Forward Stagnation Region of a Porous Cylinder, Eleventh Symposium (International) on Combustion, The Combustion Institute, Pittsburgh, p. 979.
Tsuji, H. and Yamaoka, I. (1969) The Structure of Counterflow Diffusion Flame in the Stagnation Region of a Porous Cylinder, Twelfth Symposium (International) on Combustion, The Combustion Institute, Pittsburgh, p. 997.

Tsuji, H. and Yamaoka, I. (1971) Structure Analysis of Counterflow Diffusion Flames in the Forward Stagnation Region of a Porous Cylinder, Thirteenth Symposium (International) on Combustion, p. 723.
Tsuji, H. (1982) Counterflow Diffusion Flame, *Progress in Energy and Combustion Science*, **8**, 93.
Vanquickenborne, L. and Van Tiggelen, A. (1966) The Stabilization Mechanism of Lifted Diffusion Flames, *Combustion and Flame*, **10**, 59-69.
Wang, J.-Y. (1998) The Effect of Interaction Between Two Porous Flame Mechanism with Nitrogen Ejector, M. S. Thesis, National Taiwan University, Taiwan.
Warnatz, J. (1984) Rate Coefficients in the C/H/O System, in Combustion Chemistry, Chapter 5, p. 197, Springer-Verlag, New York.
Weng, F.-B. (1989) Diffusion Flame Stabilization and Blowoff over a Porous Cylinder, M. S. Thesis, National Chiao Tung University, Taiwan.
Wohl, K., Gazley, C., and Kapp, N. (1949) Diffusion Flames, Third Symposium on Combustion, Flame, and Explosion Phenomena, p. 288.
Yang, J. C., Donnelly, M. K., Prive, N. C., and Grosshandler, W. L. (1999) Dispersed Liquid Agent Fire Suppression Screen Apparatus, NISTIR 6319, National Institute of Standards and Technology.
Zhao, J., Li, C., and Yang, S. (1997) Measurements of Temperature Distribution in a Counterflow Diffusion Flame by USED CARS, *Laser Technology*, **21**, 4, 218.

Table I

Transformed governing equations

$$\frac{\partial}{\partial x}\left(\rho u\phi - \Gamma_\phi \frac{\partial \phi}{\partial x}\right) + \frac{\partial}{\partial y}\left(\rho v\phi - \Gamma_\phi \frac{\partial \phi}{\partial y}\right) = S_\phi(x, y)$$

Equation	ϕ	Γ_ϕ	S_ϕ
continuity	1	0	0
x-momentum	u	$\frac{\mu}{Re}$	$-\frac{y_\eta}{J}\frac{\partial P}{\partial \xi} + \frac{y_\xi}{J}\frac{\partial P}{\partial \eta} + SPU$
y-momentum	v	$\frac{\mu}{Re}$	$-\frac{x_\xi}{J}\frac{\partial P}{\partial \eta} + \frac{x_\eta}{J}\frac{\partial P}{\partial \xi} + SPV$
energy	T	$\frac{\mu}{Re\ Pr}$	0

$$SPU = \frac{\partial}{\partial \xi}\left[\frac{\mu}{3Re}\frac{y_\eta}{J}\left(\frac{\partial U}{\partial \xi} + \frac{\partial V}{\partial \eta}\right) - \frac{\mu}{Re}v_\eta\right] + \frac{\partial}{\partial \eta}\left[\frac{\mu}{3Re}\frac{-y_\xi}{J}\left(\frac{\partial U}{\partial \xi} + \frac{\partial V}{\partial \eta}\right) + \frac{\mu}{Re}v_\xi\right]$$

$$SPV = \frac{\partial}{\partial \xi}\left[\frac{\mu}{3Re}\frac{-x_\eta}{J}\left(\frac{\partial U}{\partial \xi} + \frac{\partial V}{\partial \eta}\right) + \frac{\mu}{Re}u_\eta\right] + \frac{\partial}{\partial \eta}\left[\frac{\mu}{3Re}\frac{x_\xi}{J}\left(\frac{\partial U}{\partial \xi} + \frac{\partial V}{\partial \eta}\right) - \frac{\mu}{Re}u_\xi\right]$$

Table II

Rate coefficient parameters for methane oxidation reactions

No	Reaction	$\overline{B}$	$\overline{n}$	$\overline{E}$
1	$CH_4+H \rightarrow CH_3+H_2$	2.2×10	3.0	36676.4
2	$CH_4+OH \rightarrow CH_3+H_2O$	1.6×10^3	2.1	10257.7
6	$CHO+H \rightarrow CO+H_2$	2.0×10^{11}	0.0	0.0
7	$CHO+M_T \rightarrow CO+H+M_T$	7.14×10^{11}	0.0	70338.2
8	$CHO+O_2 \rightarrow CO+HO_2$	3.0×10^9	0.0	0.0
9	$CO+OH \quad CO_2+H$	4.4×10^3	1.5	-3098.2
10	$H+O_2 \quad OH+O$	1.2×10^{14}	-0.91	69165.9
14	$H+O_2+M_T \rightarrow HO_2+M_T$	2.0×10^{15}	-0.80	0.0
15	$H+OH+M_T \rightarrow H_2O+M_T$	2.15×10^{19}	-2.0	0.0
16	$H+HO_2 \rightarrow 2OH$	1.5×10^{11}	0.0	4186.8
17	$H+HO_2 \rightarrow H_2+O_2$	2.5×10^{10}	0.0	2888.9
18	$OH+HO_2 \rightarrow H_2O+O_2$	2.0×10^{10}	0.0	0.0

$$\overline{k} = \overline{BT}^{n} \exp\left(-\frac{\overline{E}}{R^{\circ}\overline{T}}\right)$$

Table III

Grid test results

The peak temperature in the whole computational domain (unit: K)

	62×27	164×85	218×115	402×221	864×501
Case B1	1989	1992	1948	1947	1947
Case B2	1899	1918	1902	1899	1900
Case B3	1870	1877	1895	1894	1895
Case B4	1872	1861	1888	1890	1885
Case B5	1859	1862	1867	1867	1867
Case B6	1858	1850	1863	1854	1853
Case B7	1884	1844	1856	1851	1850
Case B8	1877	1822	1849	1851	1848
Case B9	1875	1822	1837	1843	1844

Table IV

Summary of uncertainty analysis

Parameters	Uncertainty
D_i, D_o, L, a, b	±0.5 mm
A	±1.267%
A_{Burner}	±2.084%
$\boldsymbol{n}$	±0.09%
$\boldsymbol{r}_{air}$	±0.201%
$\overline{T}$	±0.5 ℃
$\overline{P}$	±1 torr
Q_{air}	±2.2%
Q_{fuel}	±1%
V_{air}	±2.54%
V_{fuel}	±2.31%
R_e	±3.04%

Table V

The experimental repeatibility

Fuel ejection velocity (cm/s)	Envelope flame transforms into wake flame (1^{st} measured) (m/s)	Envelope flame transforms into wake flame (2^{nd} measured) (m/s)	Envelope flame transforms into wake flame (3^{rd} measured) (m/s)	Average value of three times (m/s)	Error (%)
0.9	0.58	0.55	0.56	0.56	5.33
1.01	0.6	0.56	0.60	0.59	6.82
1.12	0.7	0.6	0.71	0.67	16.42
1.23	0.72	0.65	0.73	0.70	11.43
1.34	0.76	0.75	0.76	0.76	1.32
1.4	0.78	0.77	0.8	0.78	3.83
1.46	0.81	0.79	0.83	0.81	4.94
1.57	0.85	0.82	0.85	0.84	3.57
1.68	0.95	0.84	1.00	0.93	17.20
1.79	0.98	1.01	1.02	1.00	3.99
1.9	1.03	1.04	1.04	1.04	0.96
2.02	1.06	1.05	1.08	1.06	2.82
2.13	1.09	1.07	1.10	1.09	2.76
2.24	1.12	1.09	1.14	1.12	4.48
2.35	1.15	1.13	1.17	1.15	3.48
2.46	1.21	1.16	1.21	1.20	4.19
2.58	1.25	1.22	1.24	1.24	2.43
2.69	1.27	1.25	1.26	1.26	1.59
2.8	1.29	1.28	1.31	1.29	2.32

Table VI

Property values

Name	Symbol	Value	Unit
Ambient Temperature	$\overline{T}_a$	300	K
Reference Temperature	T^*	1250	K
Density (reference)	ρ^*	0.2835	Kg/m^3
Kinematic Viscosity (reference)	υ^*	1.69E-4	m^2/sec
Thermal Diffusivity (reference)	α^*	2.36E-4	m^2/sec
Specific Heat (reference)	C_p^*	1.351	KJ/(Kg×K)
Cylinder surface temperature	$\overline{T}_w$	400	K
Oxidizer velocity	U_{in}	variable	m/sec
Fuel-ejection velocity	v_w	0.065	m/sec
Cylinder radius	R	0.015	m
Air molecular weight (reference)	M_{air}	28.97	Kg/Kmole
Atmospheric pressure at STP condition	$\overline{P}_{rc}$	101325	Pa

Table VII

Comparison of inflow velocity regions for various flame appearances (unit: m/sec)

	Present Study	Chen and Weng (1990)
Envelope flame	< 0.9	< 1.07
Side flame	—	1.07~1.30
Wake flame	0.9~1.04	1.31~1.99
Lift-off flame	1.05~1.15	—
Late Wake flame	1.16~2.12	—
Extinction	2.13	2.00

Table VIII

The surviving range of lift-off flame

	The inflow air velocity that caused the wake flame to lift (Unit: m/sec)	The inflow air velocity that caused the lift-off flame to drop back (Unit: m/sec)
Front half side cylinder surface fuel-ejection case (S=180°)	1.05	1.14
Front three quarter cylinder surface fuel-ejection case (S=270°)	1.03	1.31
Full cylinder surface fuel-ejection case (S=360°)	1.01	1.39

Table IX

Flame lift-off height at various fuel-ejection area (U_{in}=1.05 m/sec)

	Flame lift-off height
Front half side cylinder surface fuel-ejection case (S=180°)	1.7D
Front three quarter cylinder surface fuel-ejection case (S=270°)	1.3D
Full cylinder surface fuel-ejection case (S=360°)	1.3D

Table X

The characteristics of each kind of flame for S=180°

(a) v_w = 1.12 cm/s

Inflow velocity (m/s)	Stand-off distance (mm)	Flame thickness (mm) or Attached angle	Flame length (D=diameter of cylinder)	Flame type
0.41	1.7	1.7mm	2D	Blue envelope
0.51	0.8	1.7mm	2.7D	Blue envelope
0.66		100°	2.4D	Blue wake
1.00		105°	1.6D	Blue wake
2.06		118°	0.4D	Blue wake

(b) v_w = 1.23 cm/s

Inflow velocity (m/s)	Stand-off distance (mm)	Flame thickness (mm) or Attached angle	Flame length (D=diameter of cylinder)	Flame type
0.41	1.7	2mm	2.1D	Blue envelope
0.62	0.9	2mm	2.6D	Blue envelope
0.76		100°	3.5D	Yellow wake
0.89		102°	3.2D	Yellow wake
1.04		105°	2.3D	Blue wake
1.28		110°	1.1D	Blue wake
2.35		120°	0.2D	Blue wake

(c) v_w = 2.46 cm/s

Inflow velocity (m/s)	Stand-off distance (mm)	Flame thickness (mm) or Attached angle	Flame length (D=diameter of cylinder)	Flame type
0.41	1.9	2mm	5.8D	Yellow envelope
1.0	0.8	2mm	6D	Yellow envelope
1.2		102°	6.2D	Yellow wake
1.25		104°	5.2D	Blue wake
1.58		118°	1.7D	Blue wake
3.10		118°	1D	Blue wake

(d) v_w = 3.02 cm/s

Inflow velocity (m/s)	Stand-off distance (mm)	Flame thickness (mm)	Attached angle or Lift-off flame height (H, mm)	Flame type
0.41	2.0	2.4		Yellow envelope
0.62	1.5	2.4		Yellow envelope
0.71	1.1	2.3		Yellow envelope
1.00	0.8	2.3		Yellow envelope
1.39			118°, 3mm	Lift-off flame after wake flame
1.43			124°	Blue wake
3.00			123°	Blue wake

Table XI

The characteristics of each kind of flame for S=360°

(a) v_w = 1.23 cm/s

Inflow velocity (m/s)	Stand-off distance (mm)	Flame thickness (mm) or Attached angle	Lift-off flame height (H, mm)	Flame type
0.41	1.7	2mm		Yellow envelope
0.51	1.0	2mm		Yellow envelope
0.8		101°		Yellow wake flame
1.0		108°		Yellow wake flame
1.05			2.5mm	Yellow lift-off flame
1.21			5mm	Blue lift-off flame
1.63			125°	Late wake flame

(b) v_w = 1.4 cm/s

Inflow velocity (m/s)	Stand-off distance (mm)	Flame thickness (mm)	Lift-off flame height (H, mm)	Flame type
0.41	1.7	2.1		Yellow envelope
0.51	1.1	2.1		Yellow envelope
0.84	1.0	2.0		Yellow envelope
1.06			2mm	Yellow lift-off flame
1.24			6mm	Blue lift-off flame
1.63			130°	Late wake flame

Table XII

Comparisons with Tsuji' s flame blow-off study (1982)

	Present study	Tsuji' s study	
Flame stretch rate (sec^{-1})	$-f_w$	$-f_w$	Difference (%)
141.33	0.1307	0.1565	16.49
145.33	0.1359	0.1581	14.04
149.33	0.1410	0.1597	11.71
153.33	0.1460	0.1613	9.49
160	0.1496	0.164	8.78
165.33	0.1543	0.1661	7.10
168	0.1596	0.1672	4.55
172	0.1642	0.1688	2.73

Flame stretch rate = $\frac{2U_{in}}{R}$

Nondimensional fuel-ejection rate, $-f_w=\left(\frac{v_w}{U_{in}}\right)\sqrt{\frac{\mathrm{Re}}{2}}$, $\mathrm{Re}=\frac{U_{in}R}{\nu}$

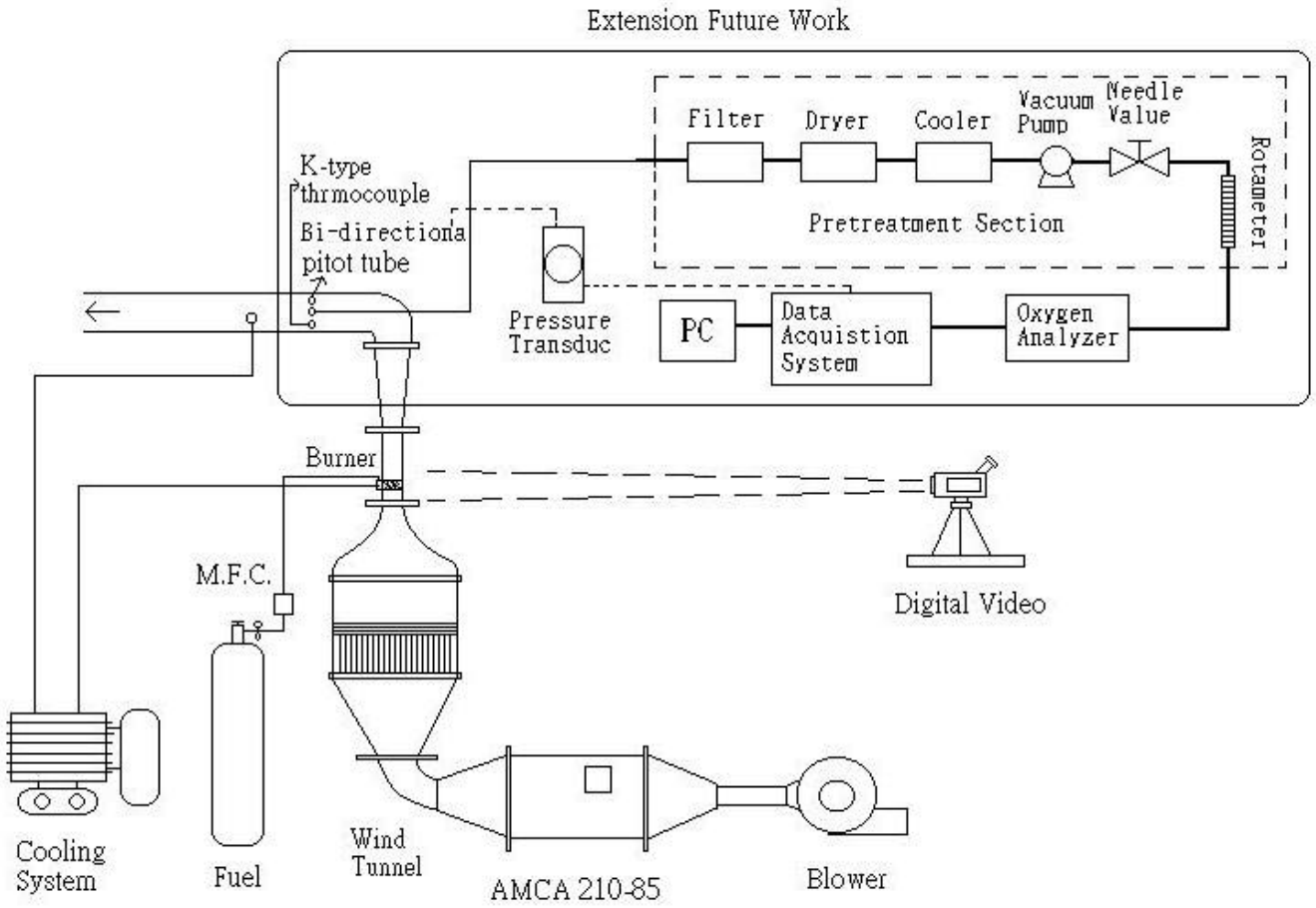

FIGURE 1 Schematic drawing of overall experimental system

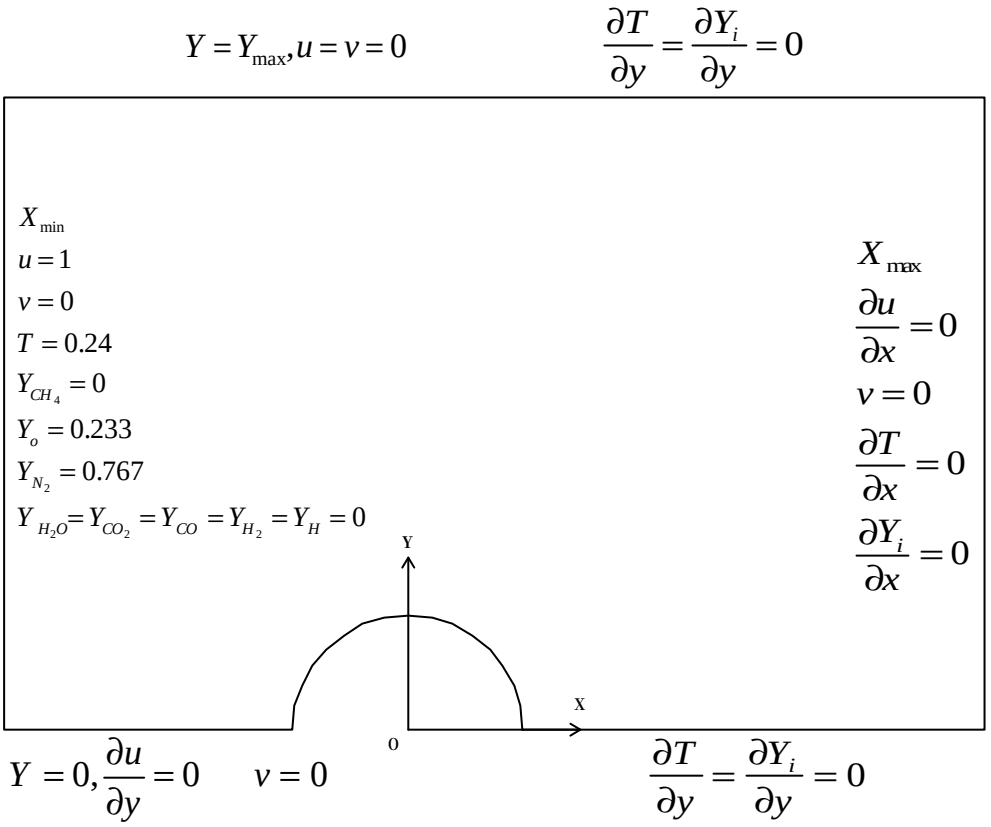

FIGURE 2 Boundary conditions of the physical domain

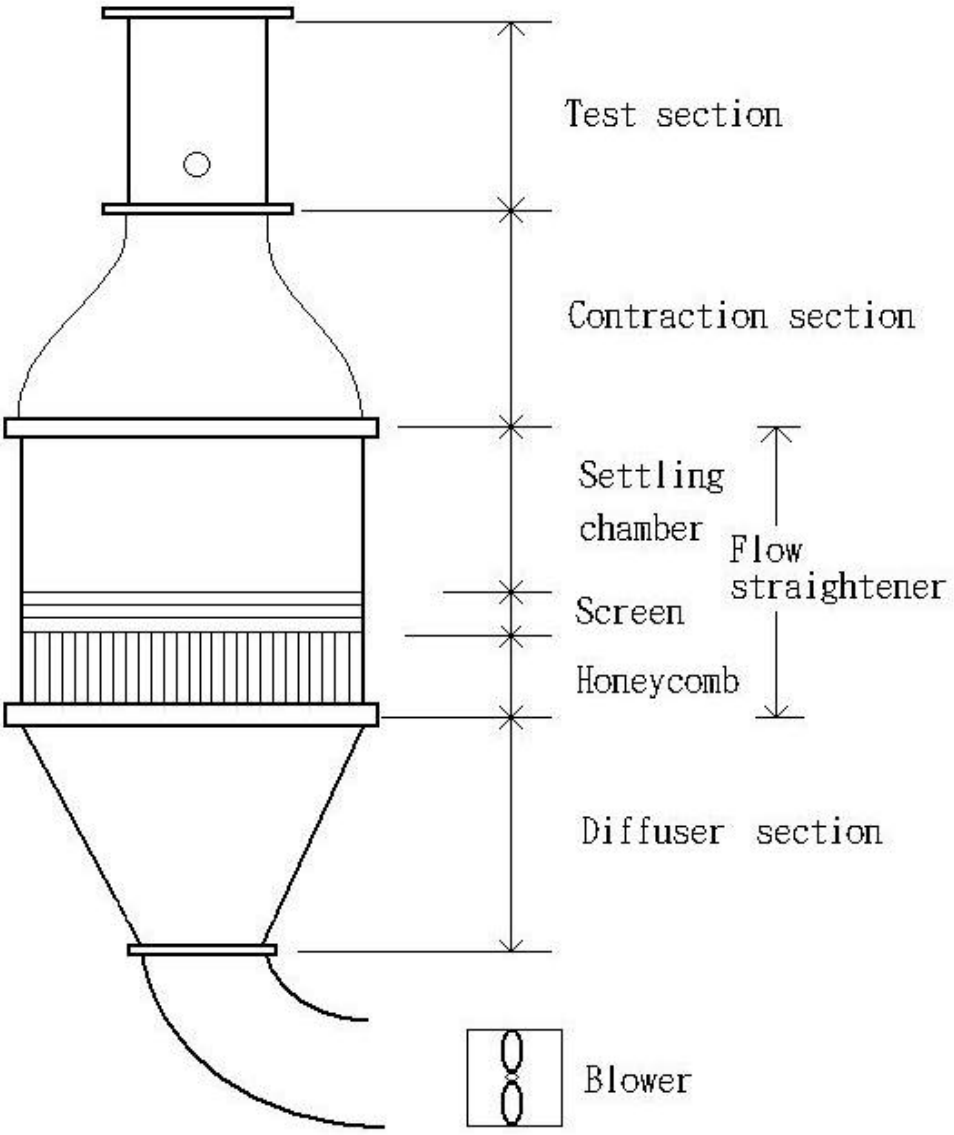

FIGURE 3 Schema of the wind tunnel

FIGURE 4 The picture of AMCA 210-85 standard in wind tunnel

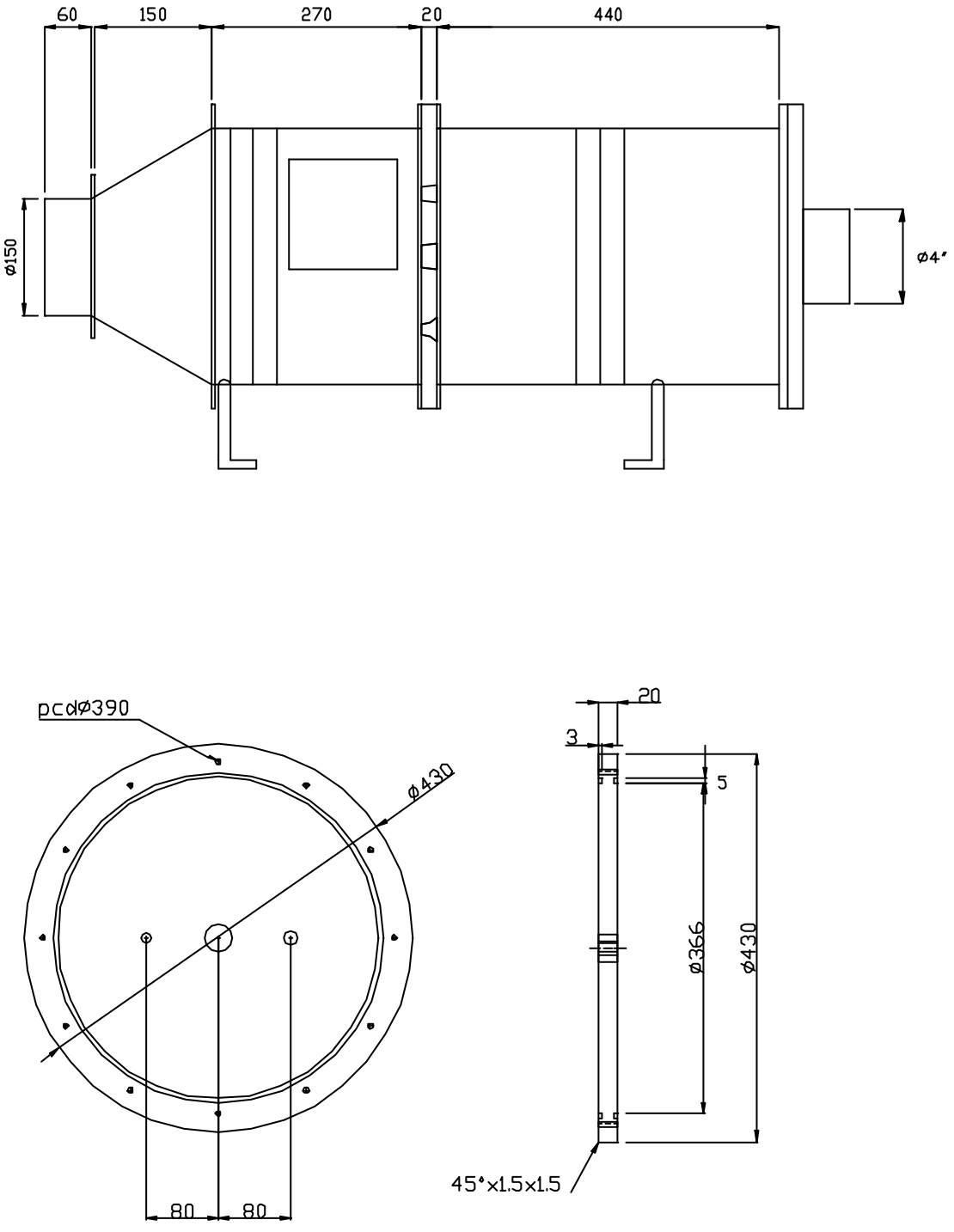

FIGURE 5 The design figure of AMCA 210-85 standard

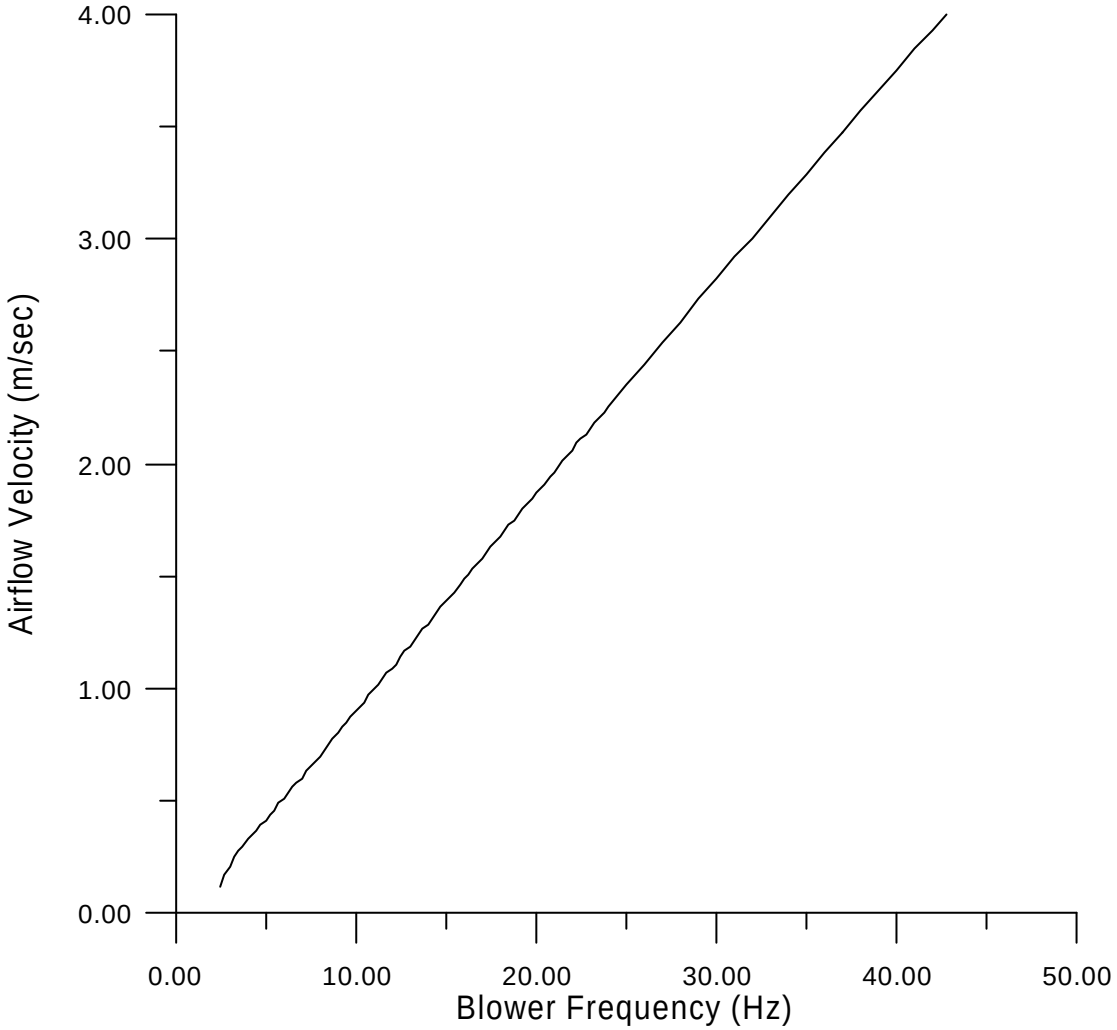

FIGURE 6 The relation figure of blower frequency and airflow velocity

FIGURE 7 The connecting of blower and tunnel

FIGURE 8 The picture of cooling system

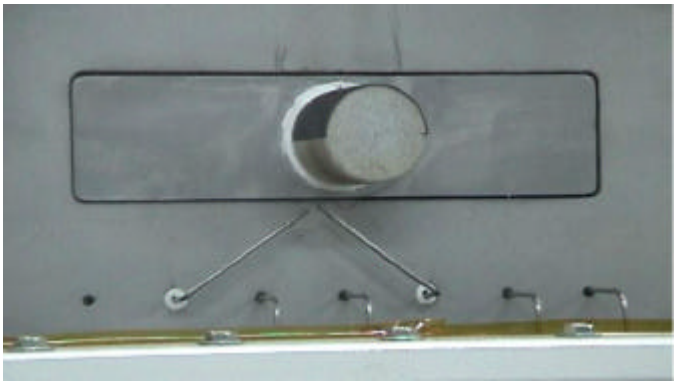

FIGURE 9 The pitot tube in test section

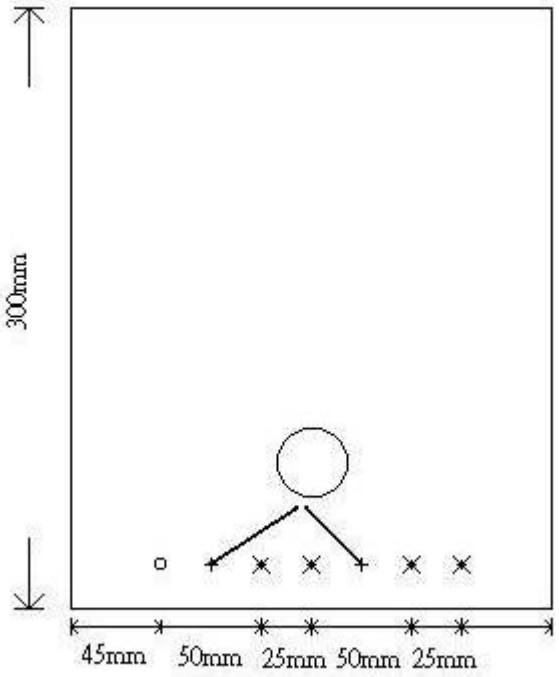

FIGURE 10 The position of pitot tube in test section

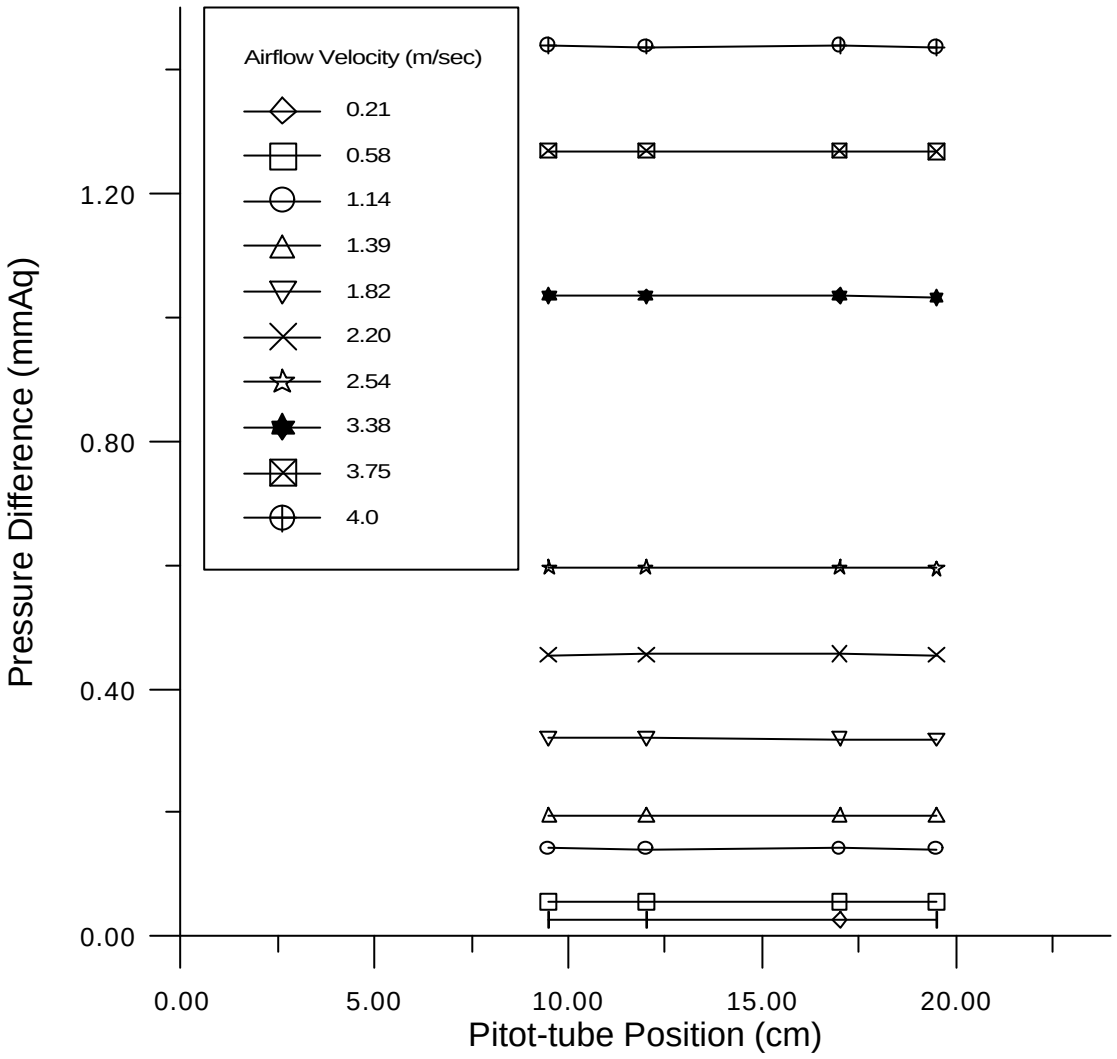

FIGURE 11 Pressure difference at different position in test section

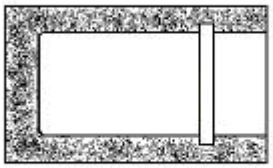

FIGURE 12 Porous sintered stainless steel cylinder

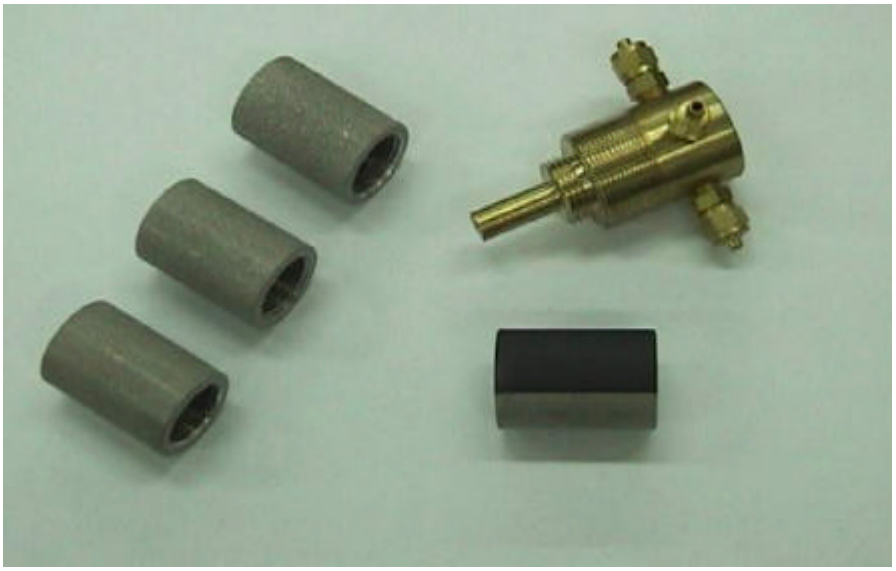

FIGURE 13 The picture of burner

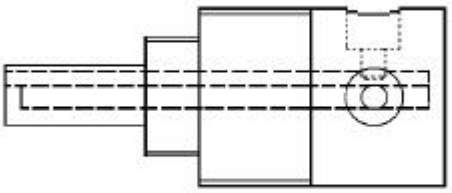

FIGURE 14 Cylindrical brass rod

FIGURE 15 The digital mass flow controller

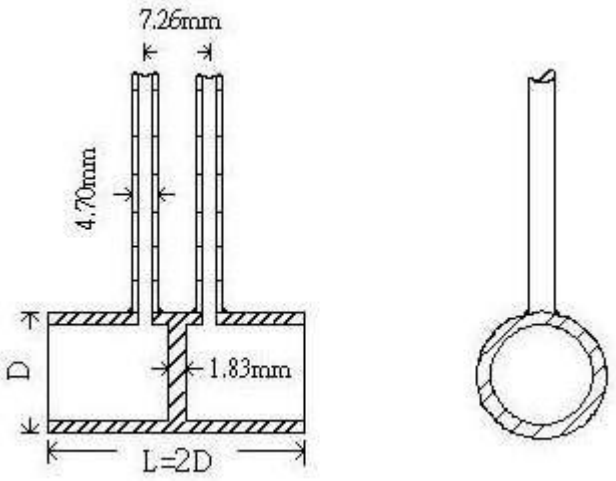

FIGURE 16 The design figure of bi-directional pitot tube

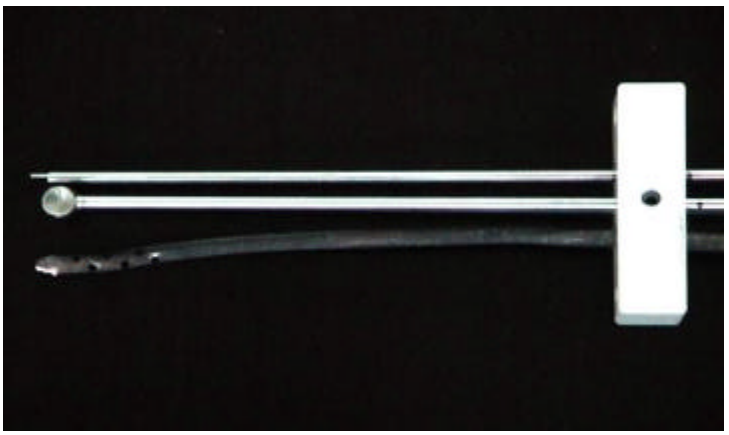

FIGURE 17 The picture of bi-directional pitot tube

FIGURE 18 The picture of O_2 analyzer

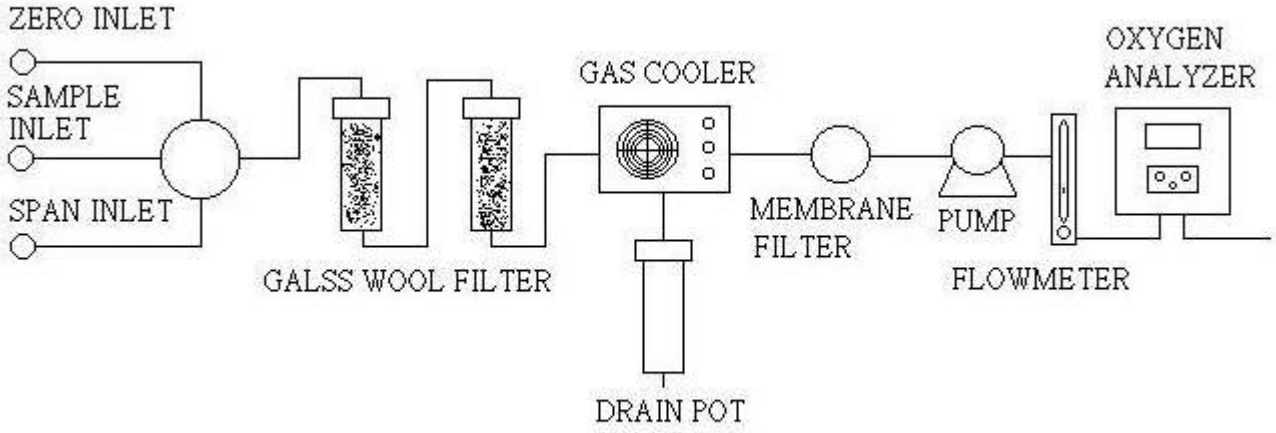

FIGURE 19 The connecting path in the pretreatment system

FIGURE 20 The picture of the pretreatment system

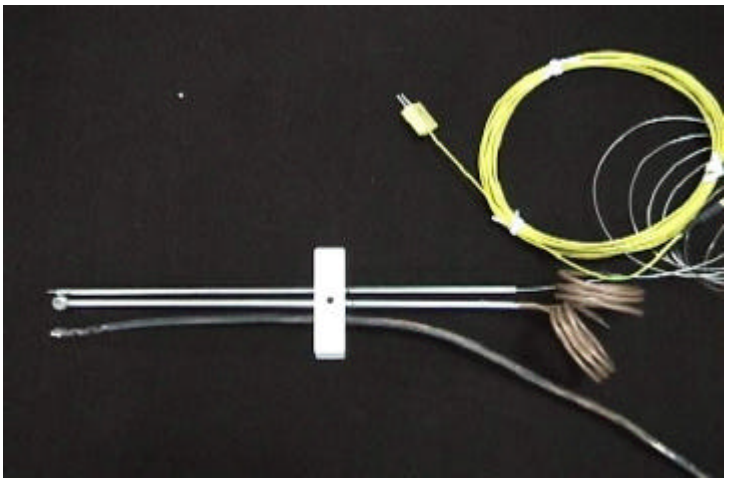

FIGURE 21 The measuring probes in the vent

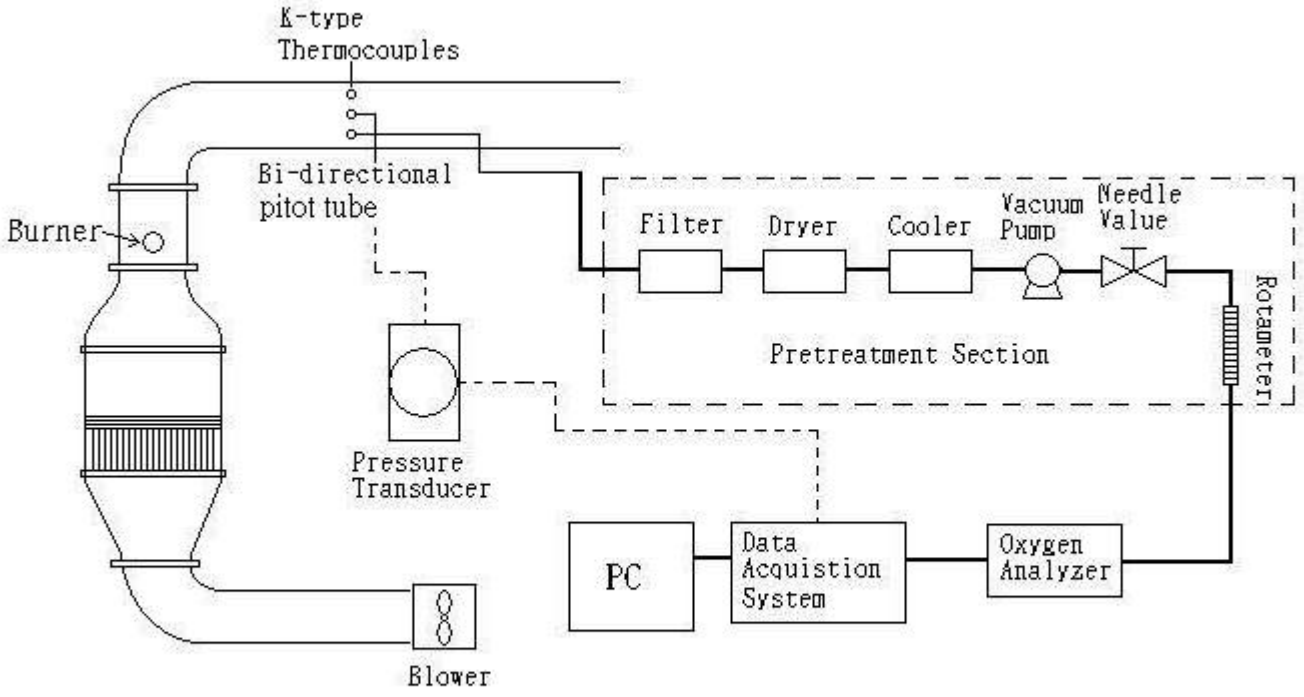

FIGURE 22 Schema of instruments building

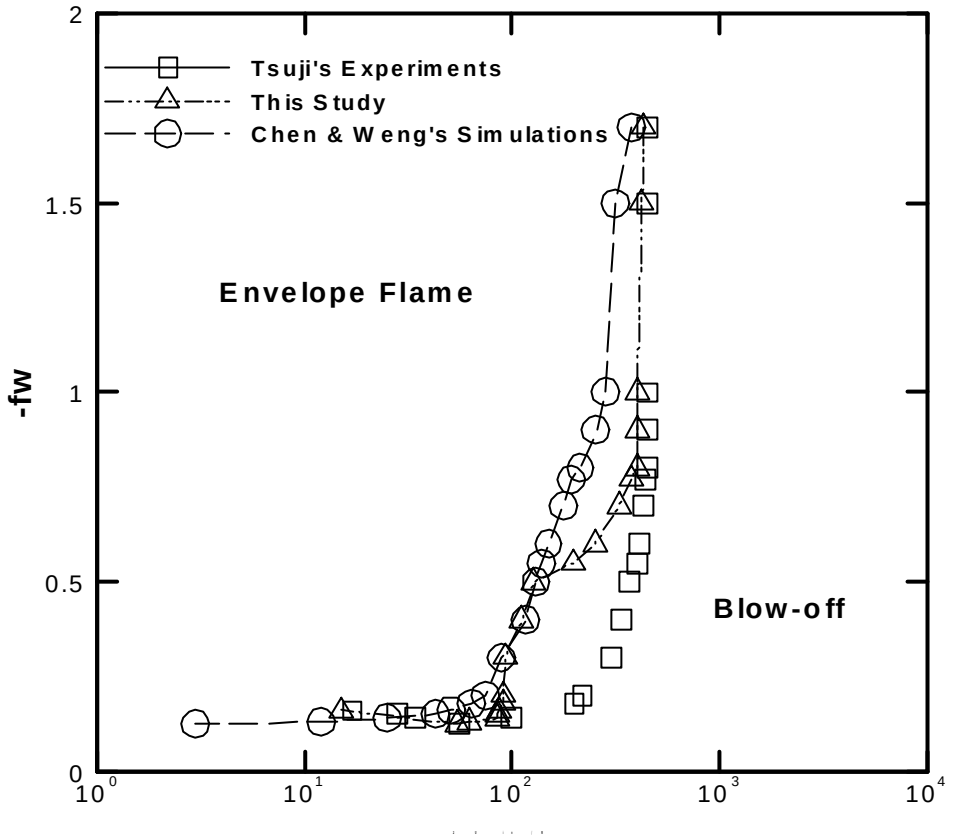

FIGURE 23 Flame blow-off curves for counterflow diffusion flame in the forward stagnation region of a porous cylinder (R=1.5cm, and the fuel is methane)

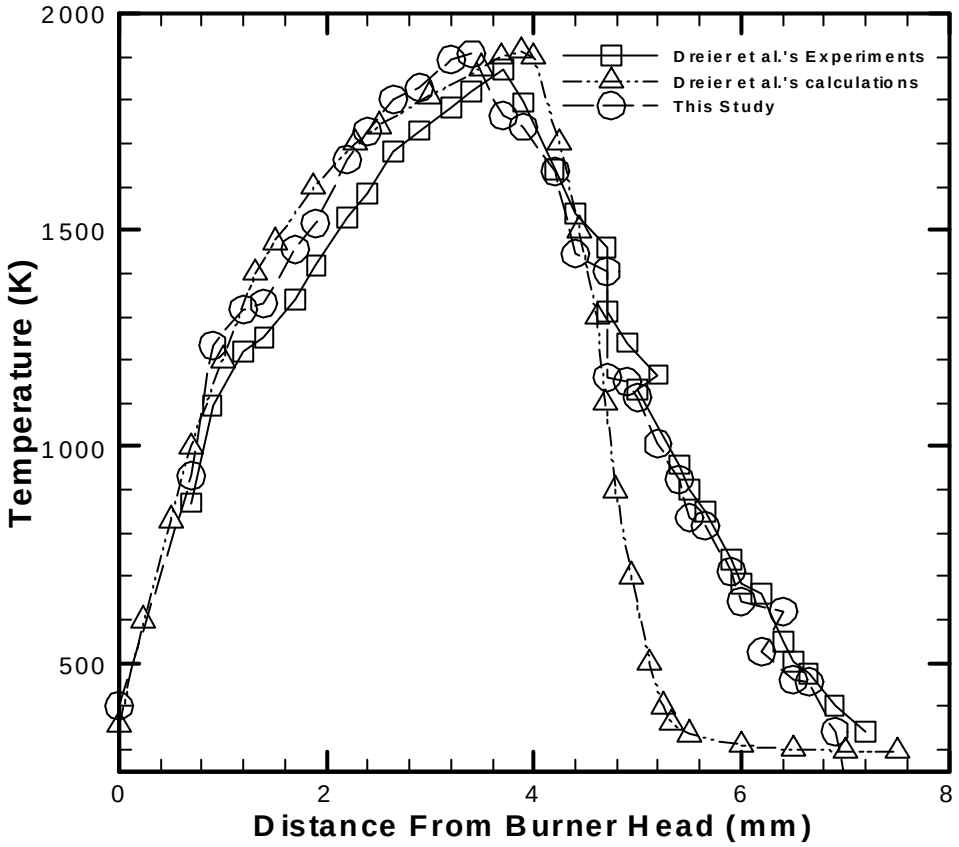

FIGURE 24 Temperature distributions through the flame front of a Tsuji burner with R=0.02m, U_{in}=0.15m/sec, and $-f_w$=0.318. The solid line and its corresponding squares are the CARS measurements of Dreier et al. (1986), the dash-dot-dot line and its corresponding triangles are the numerical results of Dreier et al. (1986), and the dashed line and its corresponding circles are the numerical results of the current study.

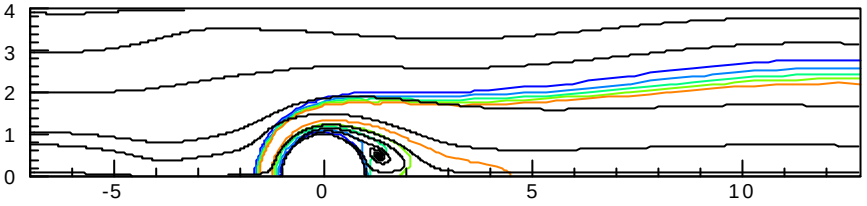

(A1) U_{in} = 0.75m/sec (k_s=100 sec^{-1}) (Chen and Weng, 1990)

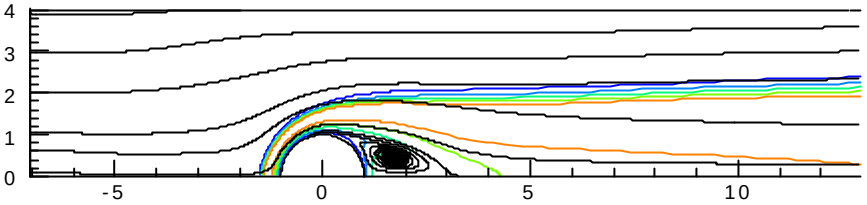

(B1) U_{in} = 0.75m/sec (k_s=100 sec^{-1})

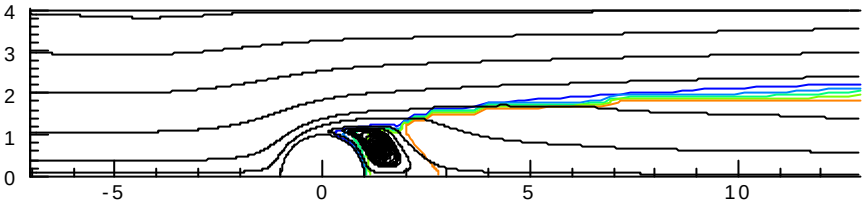

(B2) U_{in} = 0.9m/sec (k_s=120 sec^{-1})

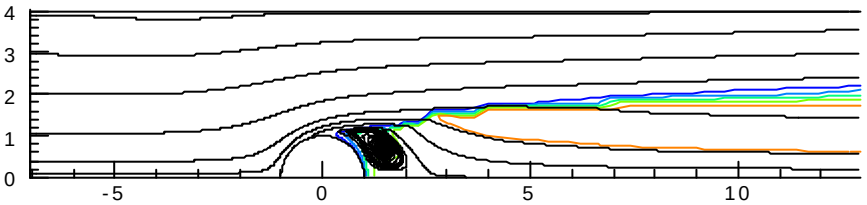

(B3) U_{in} = 1.04m/sec (k_s=138.67 sec^{-1})

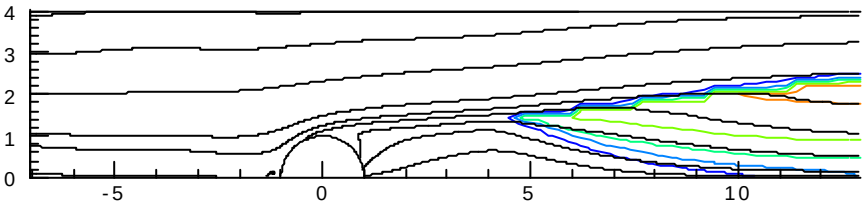

(B4) U_{in} = 1.05m/sec (k_s=140 sec^{-1})

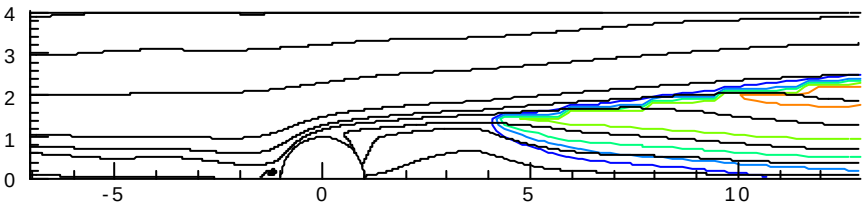

(B5) U_{in} = 1.1m/sec (k_s=146.67 sec^{-1})

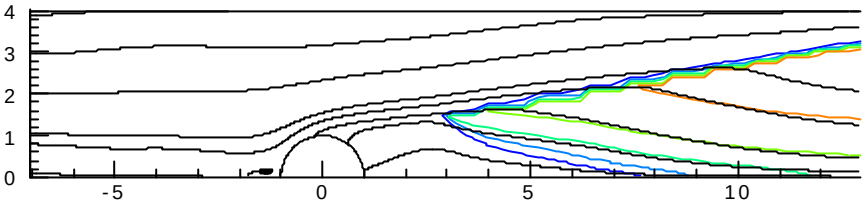

(B6) U_{in} = 1.12m/sec (k_s=149.33 sec^{-1})

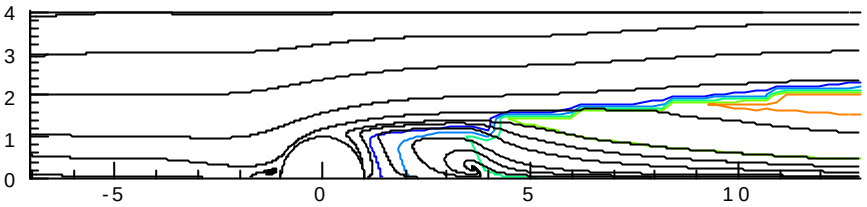

(B7) U_{in} = 1.13m/sec (k_s=150.67 sec^{-1})

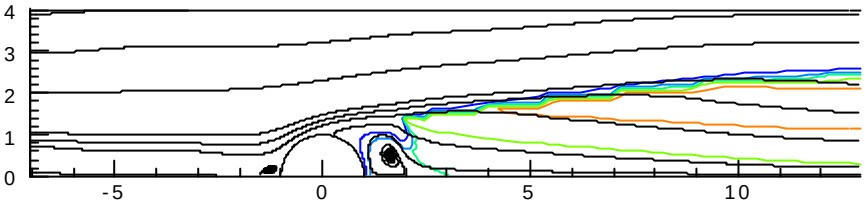

(B8) U_{in} = 1.14m/sec (k_s=152 sec^{-1})

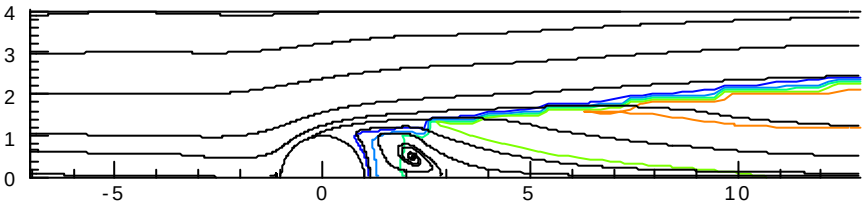

(B9) U_{in} = 1.15m/sec (k_s=153.33 sec^{-1})

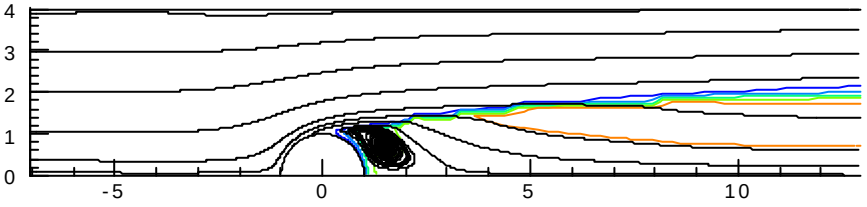

(B10) U_{in} = 1.16m/sec (k_s=154.67 sec^{-1})

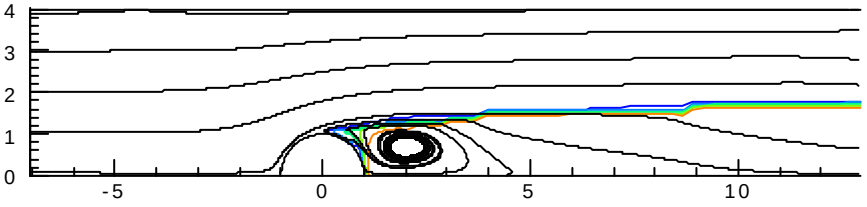

(B11) U_{in} = 2.12m/sec (k_s=282.67 sec^{-1})

FIGURE 25 Series of temperature contours and streamlines

(The orange, light green, dark green, light blue, and dark blue lines represent 1800, 1500, 1200, 900, and 600K temperature contours, respectively.)

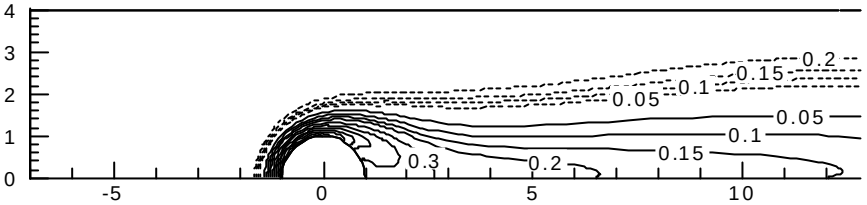

(A1) U_{in} = 0.75m/sec (k_s=100 sec^{-1}) (Chen and Weng, 1990)

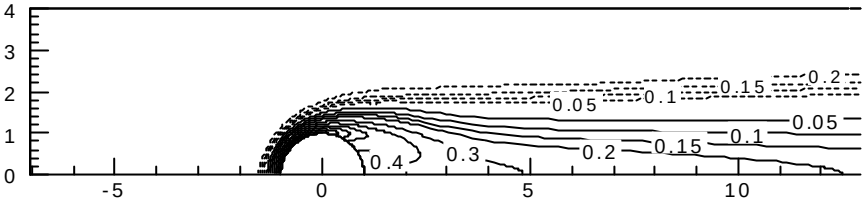

(B1) U_{in} = 0.75m/sec (k_s=100 sec^{-1})

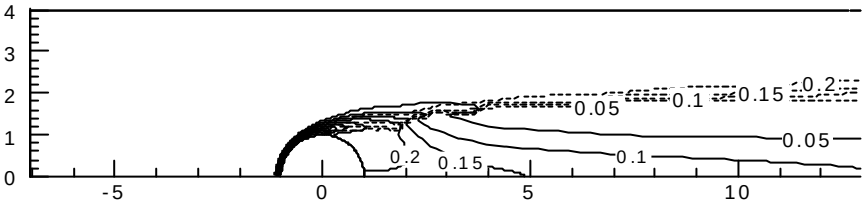

(B2) U_{in} = 0.9m/sec (k_s=120 sec^{-1})

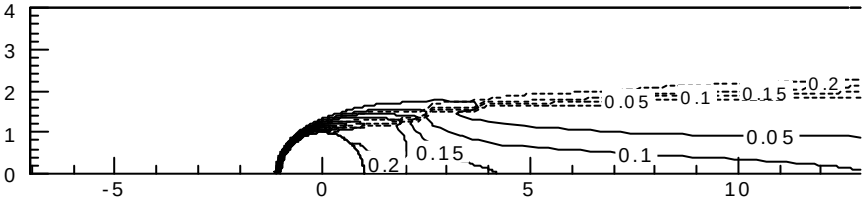

(B3) U_{in} = 1.04m/sec (k_s=138.67 sec^{-1})

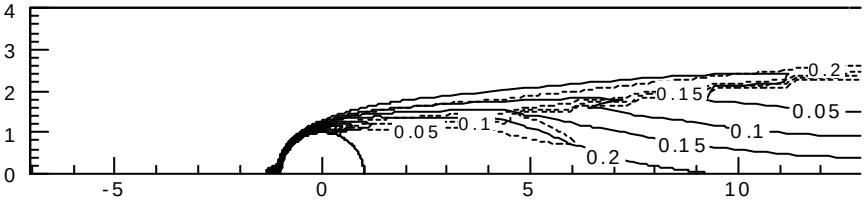

(B4) U_{in} = 1.05m/sec (k_s=140 sec^{-1})

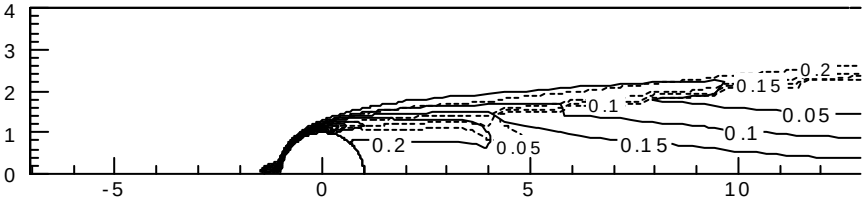

(B5) U_{in} = 1.1m/sec (k_s=146.67 sec^{-1})

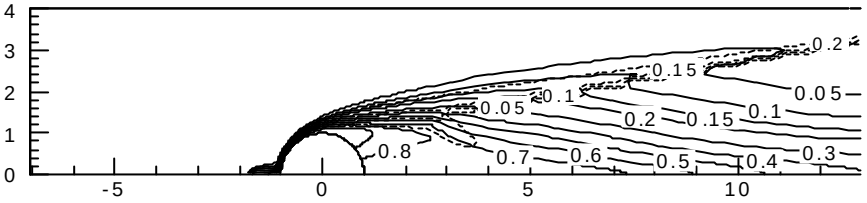

(B6) U_{in} = 1.12m/sec (k_s=149.33 sec^{-1})

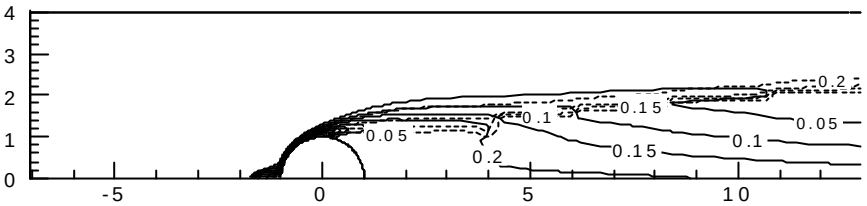

(B7) U_{in} = 1.13m/sec (k_s=150.67 sec^{-1})

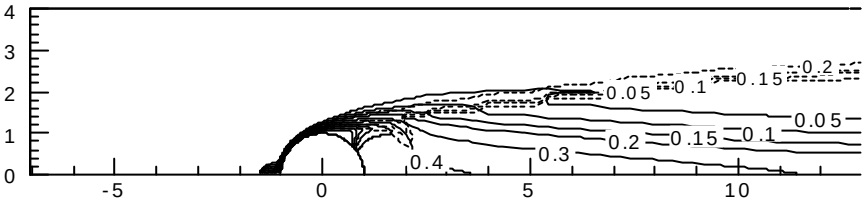

(B8) U_{in} = 1.14m/sec (k_s=152 sec^{-1})

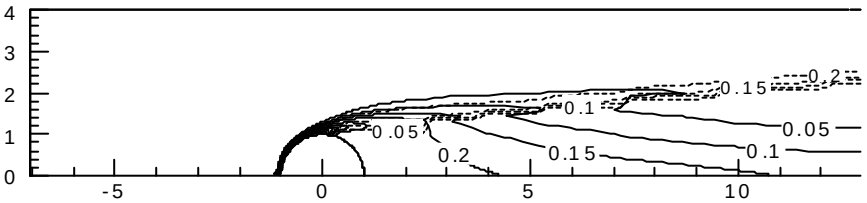

(B9) U_{in} = 1.15m/sec (k_s=153.33 sec^{-1})

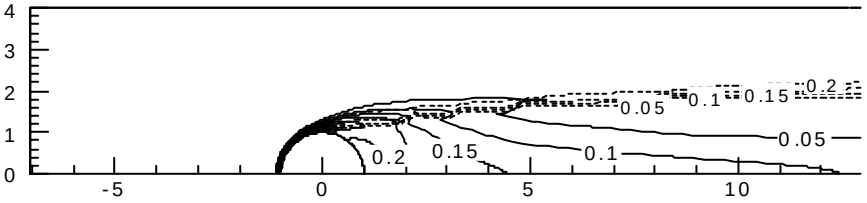

(B10) U_{in} = 1.16m/sec (k_s=154.67 sec^{-1})

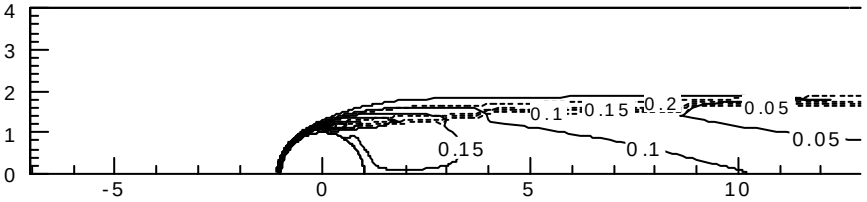

(B11) U_{in} = 2.12m/sec (k_s=282.67 sec^{-1})

FIGURE 26 Series of methane (solid lines) and oxygen (dashed lines) mass fraction contours

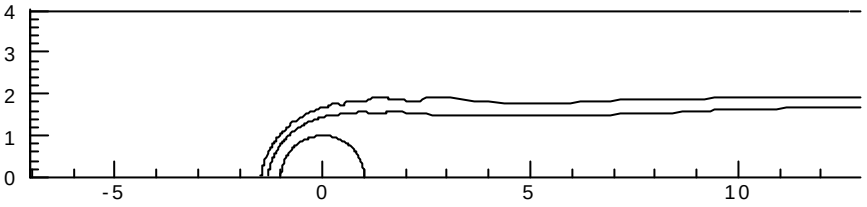

(B1) U_{in} = 0.75m/sec (k_s=100 sec^{-1})

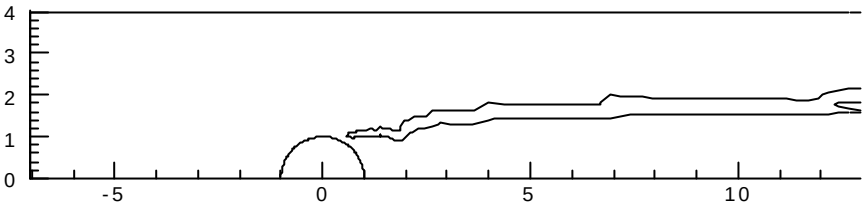

(B2) U_{in} = 0.9m/sec (k_s=120 sec^{-1})

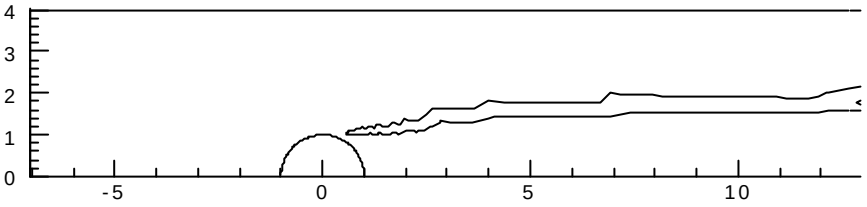

(B3) U_{in} = 1.04m/sec (k_s=138.67 sec^{-1})

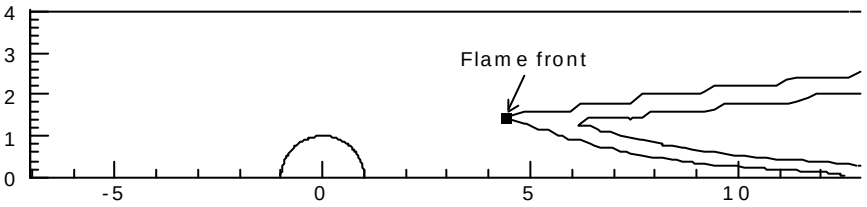

(B4) U_{in} = 1.05m/sec (k_s=140 sec^{-1})

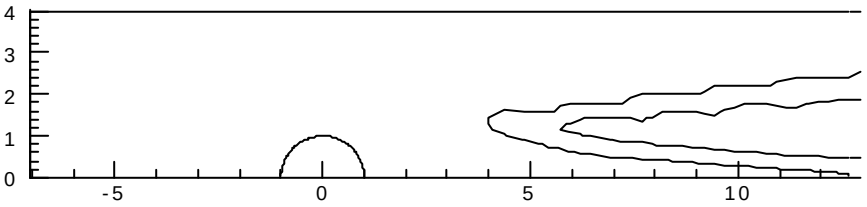

(B5) U_{in} = 1.1m/sec (k_s=146.67 sec^{-1})

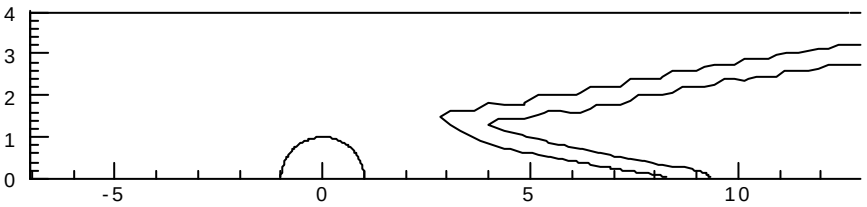

(B6) U_{in} = 1.12m/sec (k_s=149.33 sec^{-1})

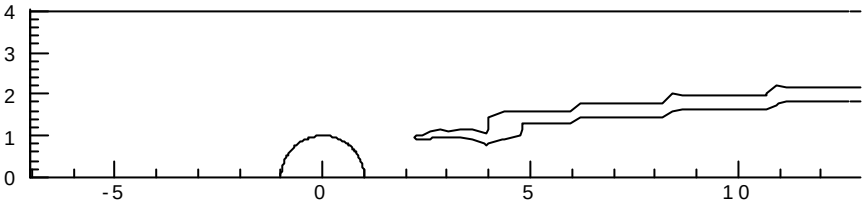

(B7) U_{in} = 1.13m/sec (k_s=150.67 sec^{-1})

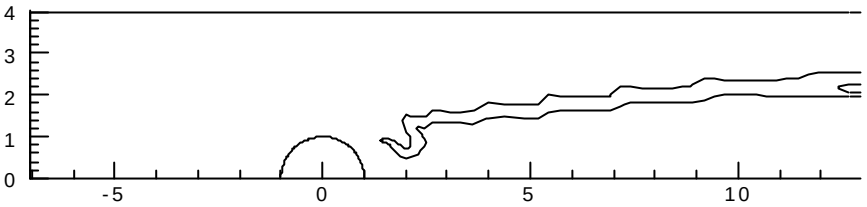

(B8) U_{in} = 1.14m/sec (k_s=152 sec^{-1})

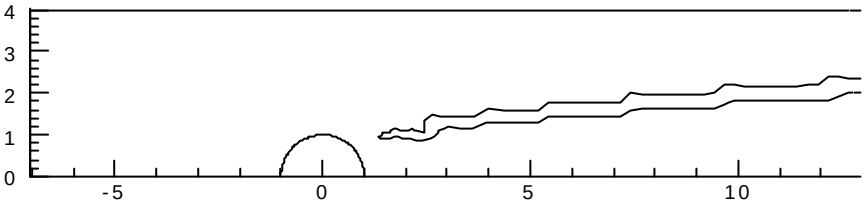

(B9) U_{in} = 1.15m/sec (k_s=153.33 sec^{-1})

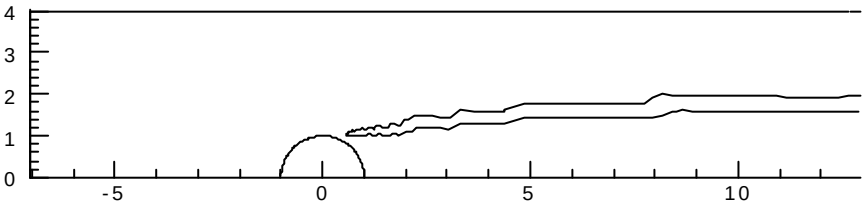

(B10) U_{in} = 1.16m/sec (k_s=154.67 sec^{-1})

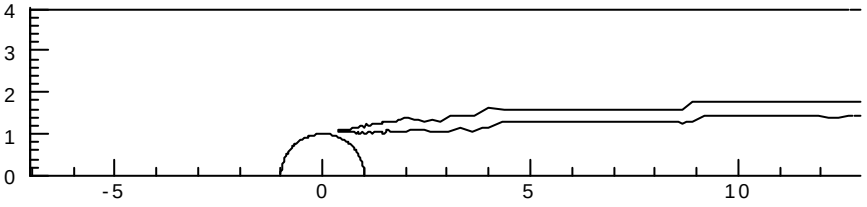

(B11) U_{in} = 2.12m/sec (k_s=282.67 sec^{-1})

FIGURE 27 Series of 10^{-4} g/(cm^3×sec) methane reaction rate contours

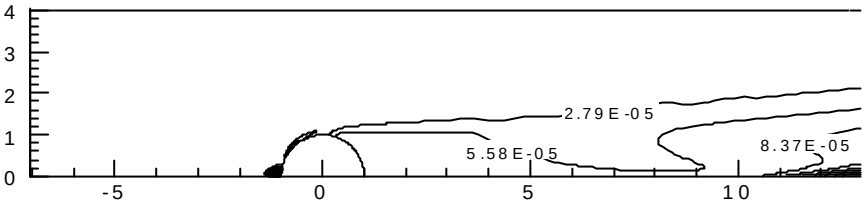

(B4) U_{in} = 1.05m/sec (k_s=140 sec^{-1})

FIGURE 28 The mass fraction contours of hydrogen for case B4

(C1) Envelope flame (U_{in}=1.0m/sec)

(C2) Wake flame (U_{in}=1.2m/sec)

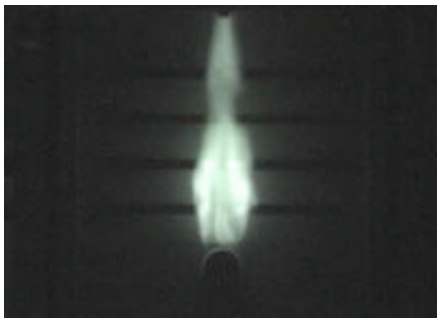

(C3) Lift-off flame (U_{in}=1.39m/sec)

(C4) Late wake flame (U_{in}=1.43m/sec)

(Night shot photograph)

FIGURE 29 The flame configurations for the experimental visualization ($-f_w$=0.201)

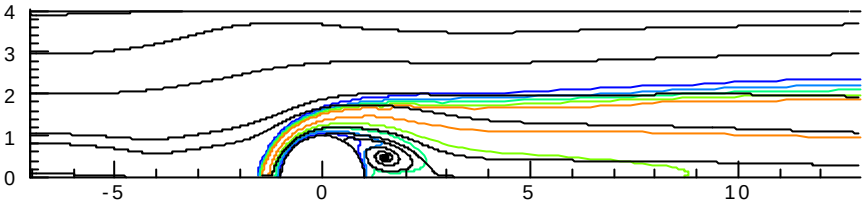

(C1) U_{in} = 0.75m/sec (k_s=100 sec^{-1})

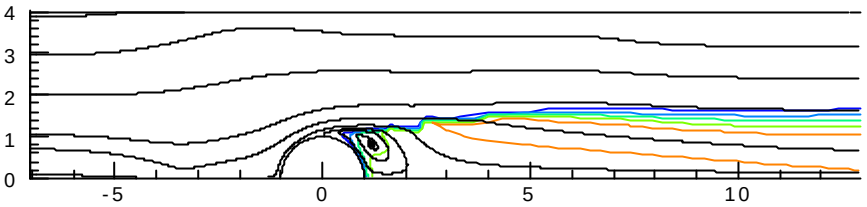

(C2) U_{in} = 1.0m/sec (k_s=133.33 sec^{-1})

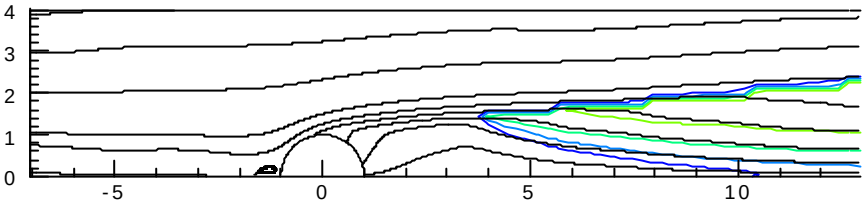

(C3) U_{in} = 1.05m/sec (k_s=140 sec^{-1})

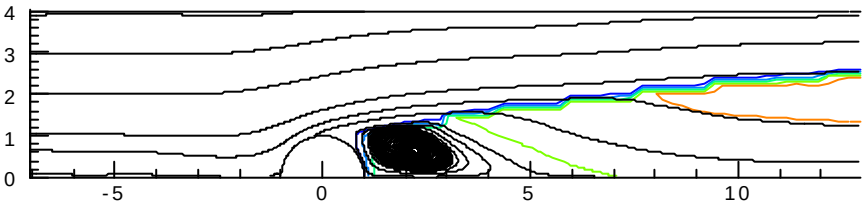

(C4) U_{in} = 1.32m/sec (k_s=176 sec^{-1})

FIGURE 30 Series of temperature contours and streamlines in the front three quarter side cylinder surface fuel-ejection condition (S=270°)

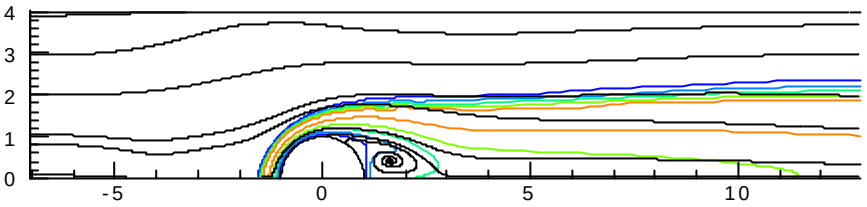

(D1) U_{in} = 0.75m/sec (k_s=100 sec^{-1})

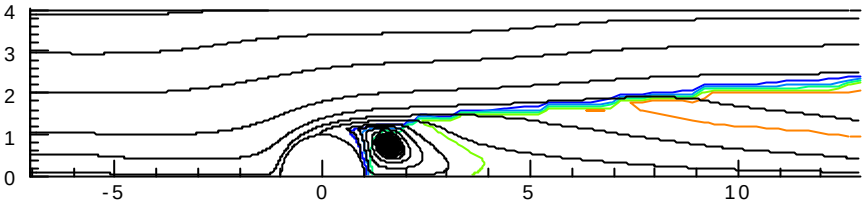

(D2) U_{in} = 1.0m/sec (k_s=133.33 sec^{-1})

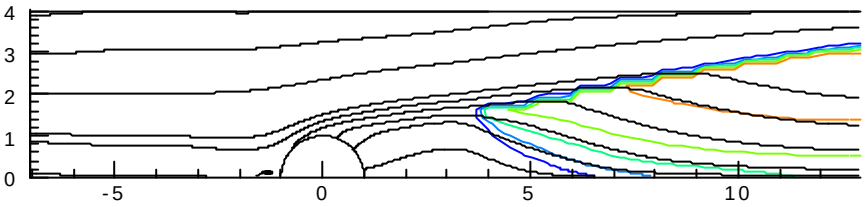

(D3) U_{in} = 1.05m/sec (k_s=140 sec^{-1})

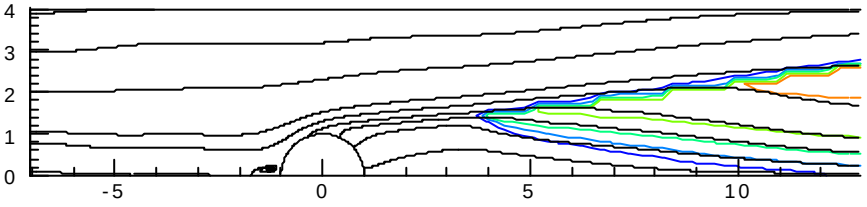

(D4) U_{in} = 1.15m/sec (k_s=153.33 sec^{-1})

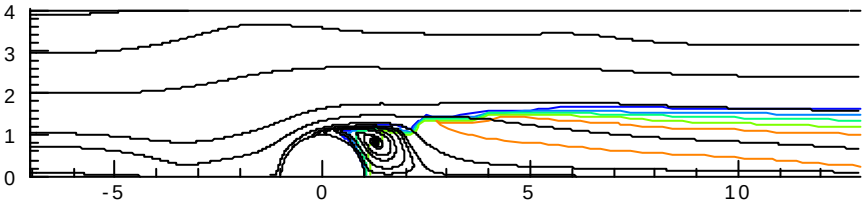

(D5) U_{in} = 1.4m/sec (k_s=186.67 sec^{-1})

FIGURE 31 Series of temperature contours and streamlines in the full cylinder surface fuel-ejection condition (S=360°)

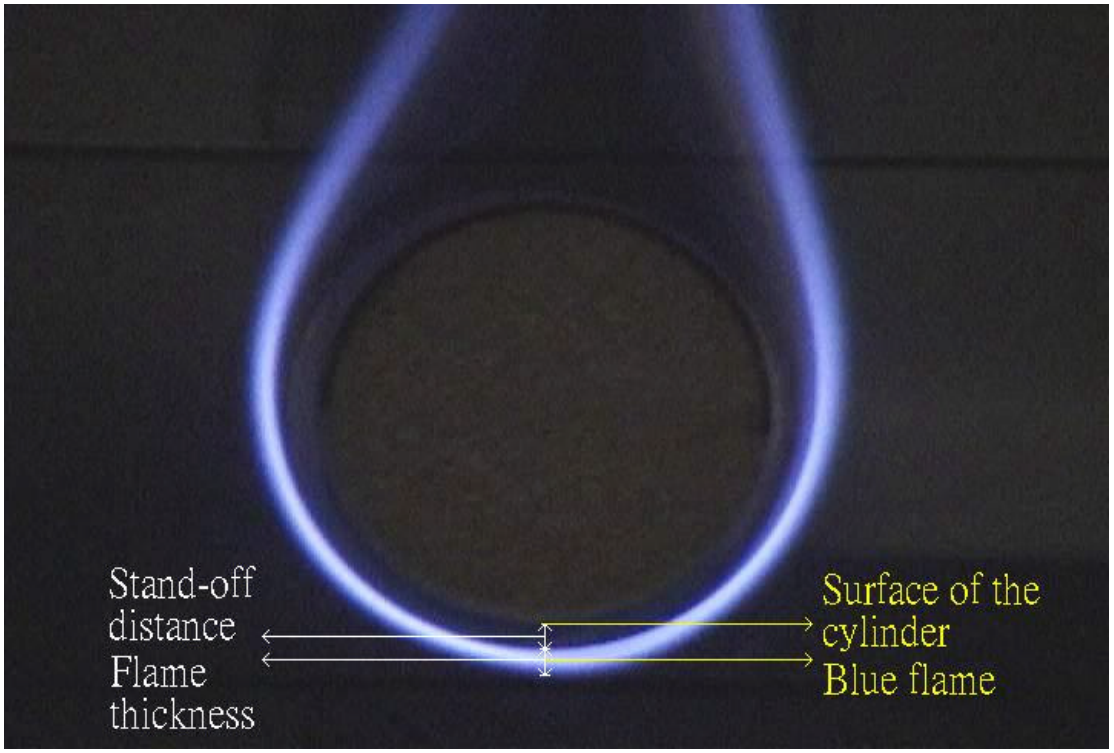

(a) Flame stand-off distance and flame thickness

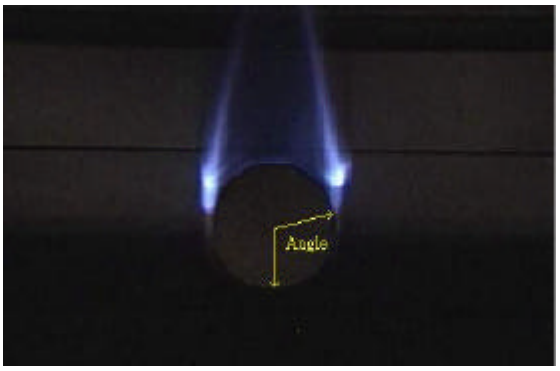

(b) Flame attached angle

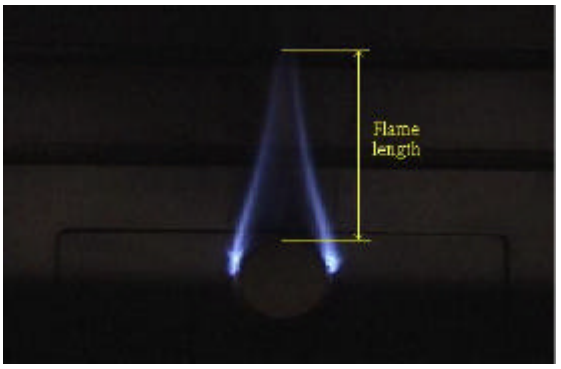

(c) Flame length

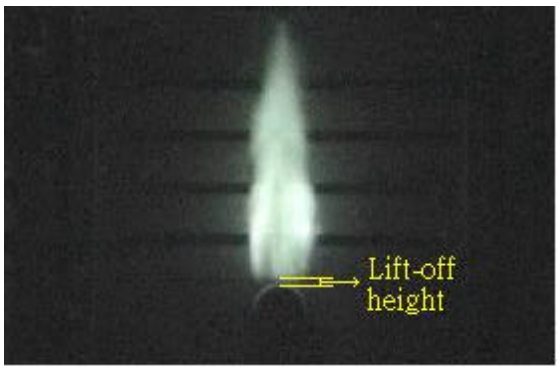

(d) Flame lift-off height (H)

FIGURE 32 Definitions of flame stand-off distance, flame thickness, flame attached angle, flame length, and flame lift-off height for each kind of flame

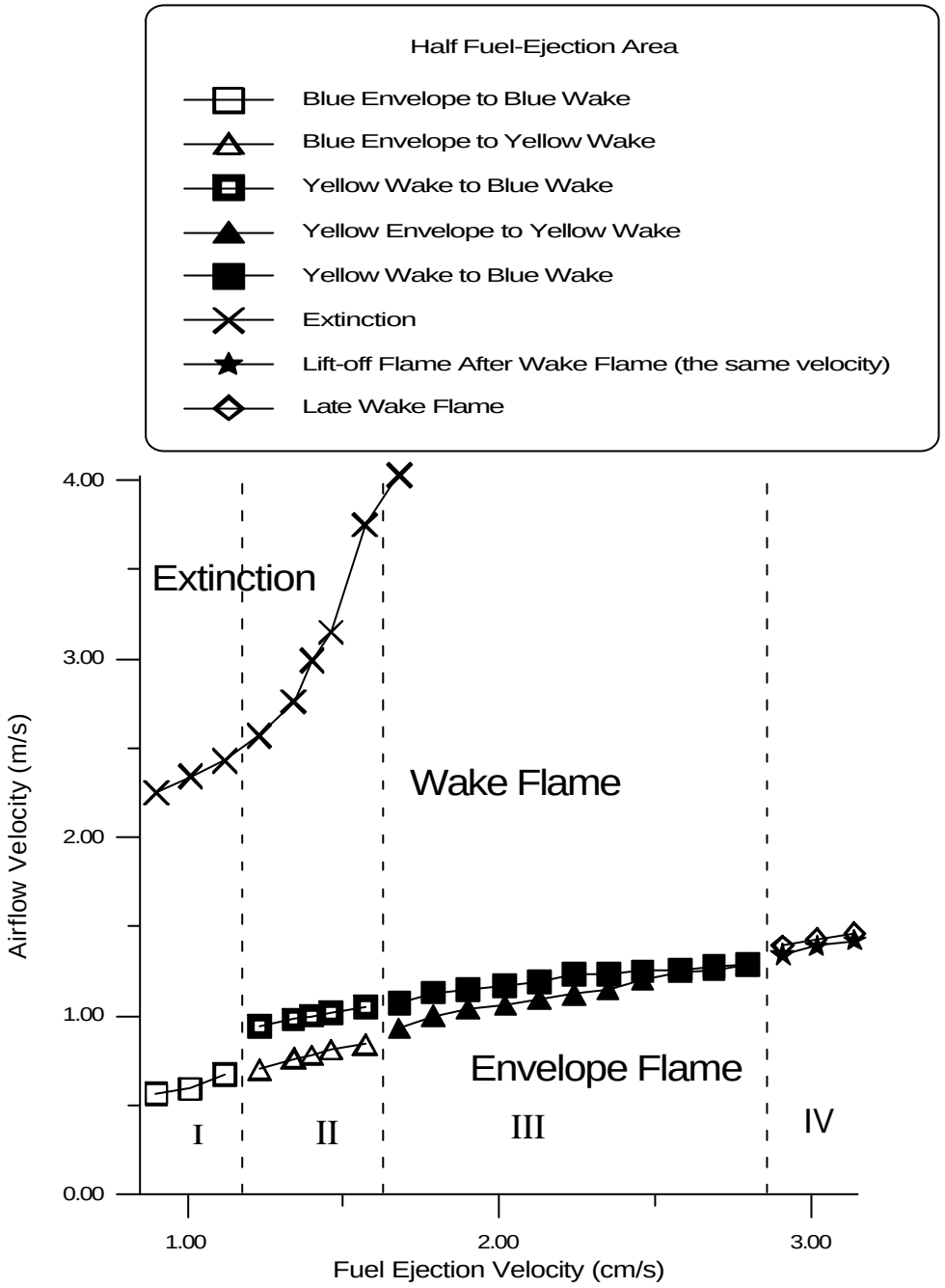

FIGURE 33 Various flame stabilization regions over a burner (S=180°)

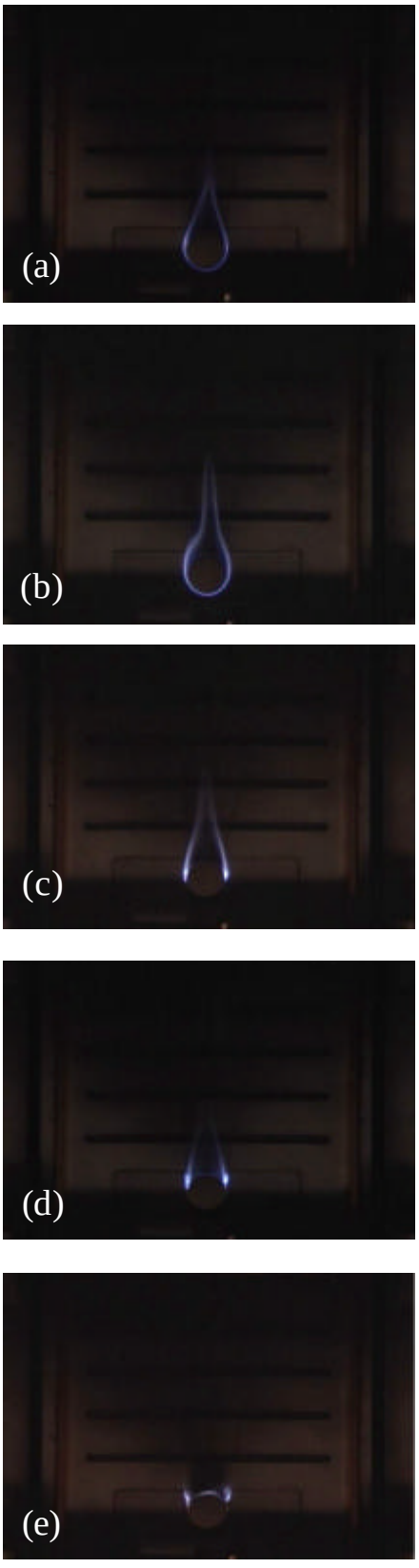

FIGURE 34 Series of flame configurations as a function of inflow velocity (v_w = 1.12cm/s and S = 180°), (a) U_{in} = 0.41m/s, (b) U_{in} = 0.51m/s, (c) U_{in} = 0.66m/s, (d) U_{in} = 1.00m/s, and (e) U_{in} = 2.06 m/s

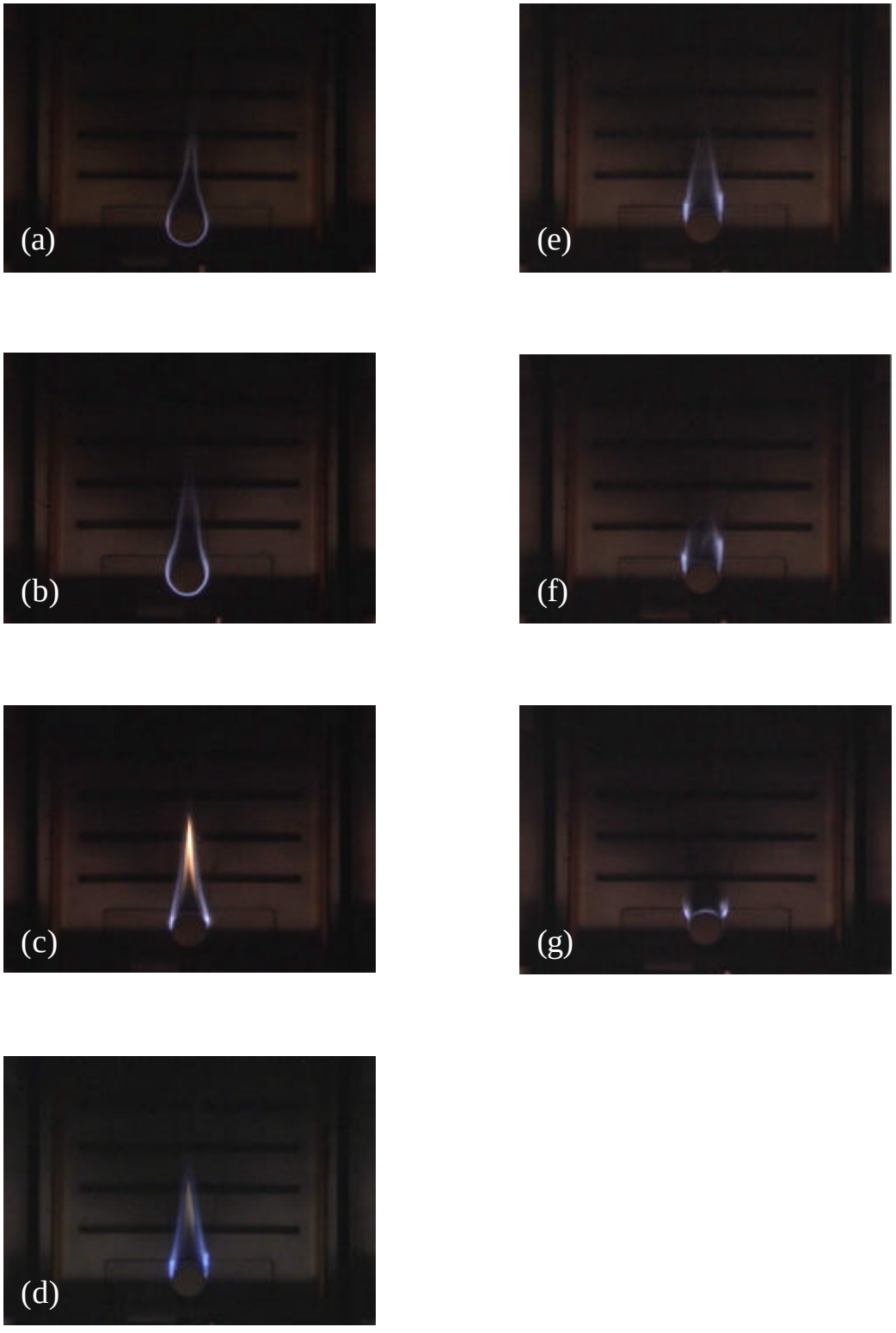

FIGURE 35 Series of flame configurations as a function of inflow velocity (v_w = 1.23cm/s and S = 180°), (a) U_{in} = 0.41m/s, (b) U_{in} = 0.62m/s, (c) U_{in} = 0.76m/s, (d) U_{in} = 0.89m/s, (e) U_{in} = 1.04 m/s, (f) U_{in} = 1.28m/s, and (g) U_{in} = 2.35m/s

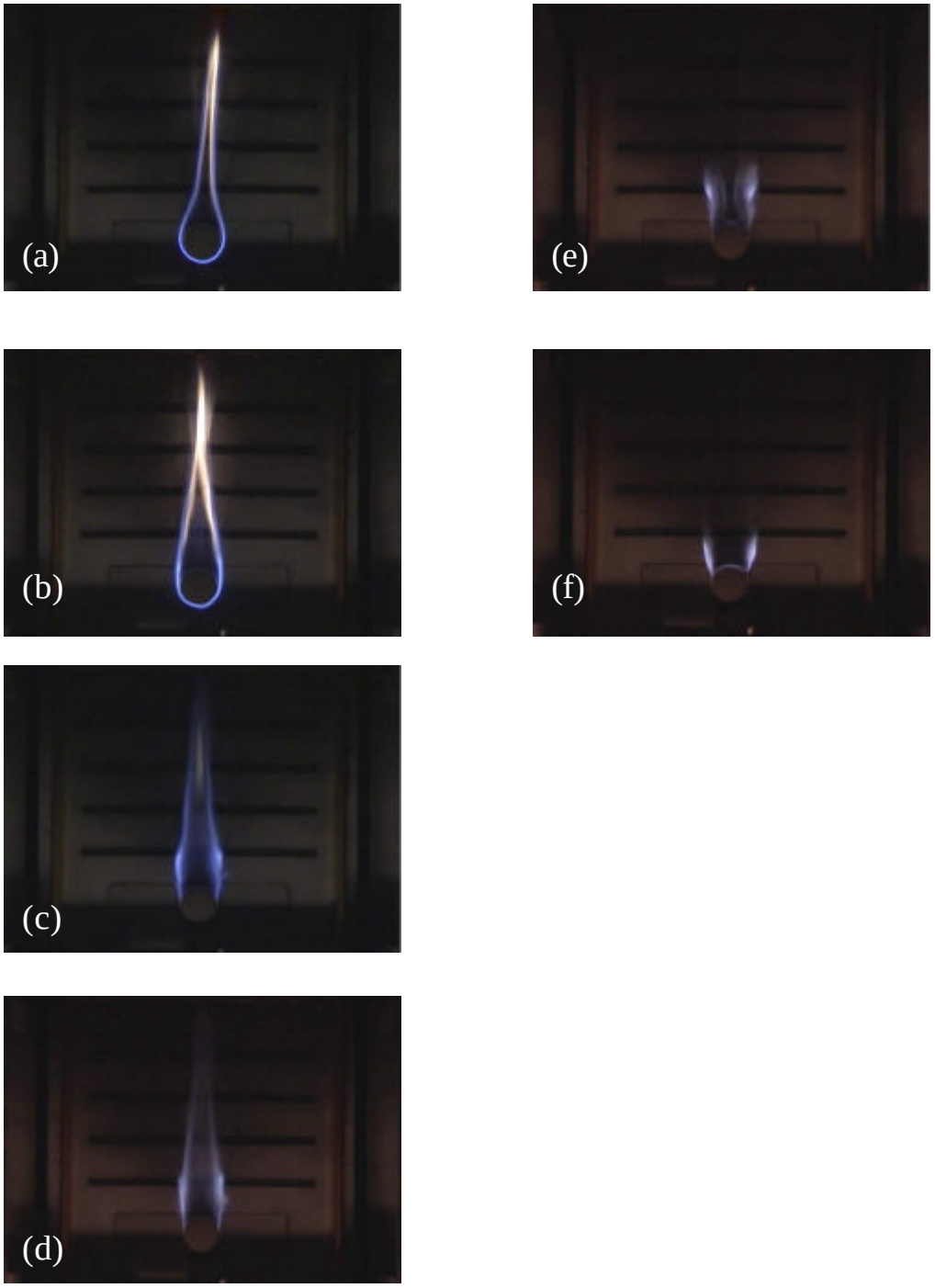

FIGURE 36 Series of flame configurations as a function of inflow velocity (v_w = 2.46cm/s and S=180°), (a) U_{in} = 0.41m/s, (b) U_{in} = 1.00m/s, (c) U_{in} = 1.2m/s, (d) U_{in} = 1.25m/s, (e) U_{in} = 1.58m/s, and (f) U_{in} = 3.10m/s

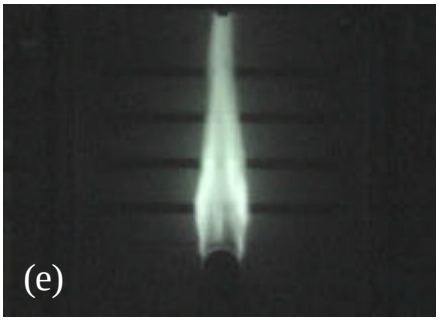

(1) t = 0 sec

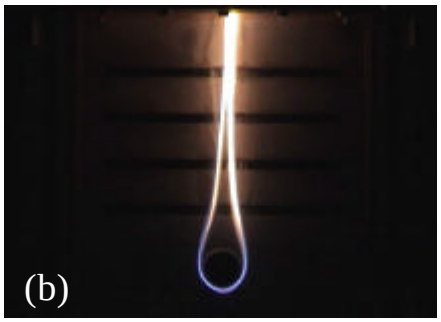

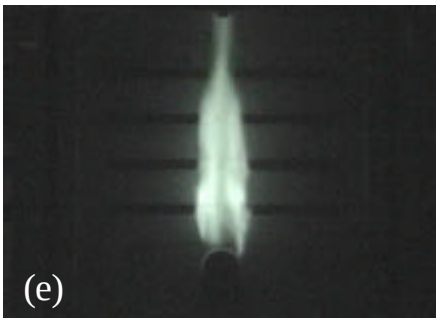

(2) t = 4 ms

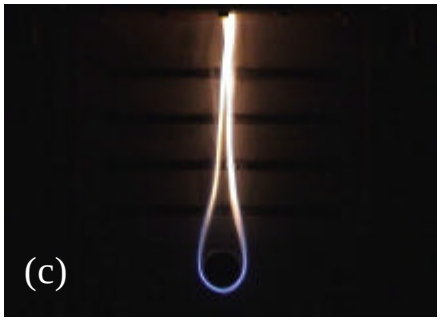

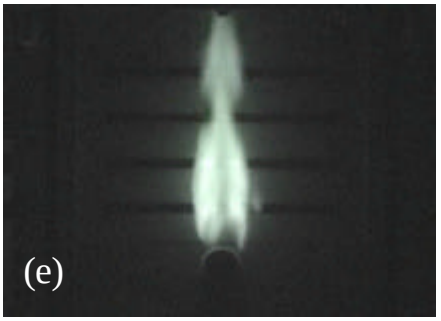

(3) t = 7 ms

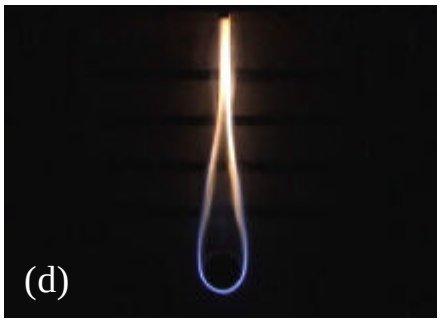

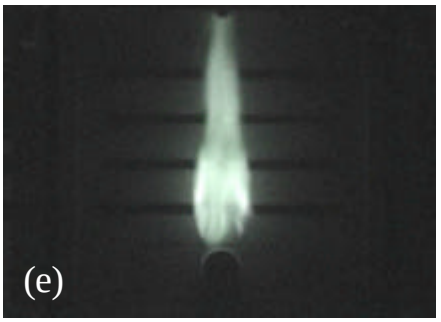

(4) t = 11ms

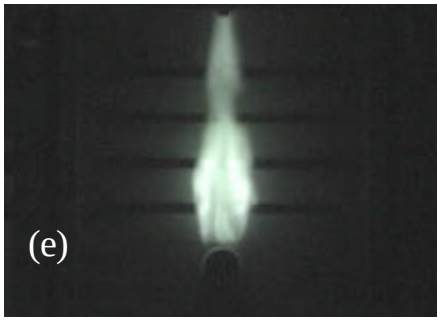

(5) t = 35 ms

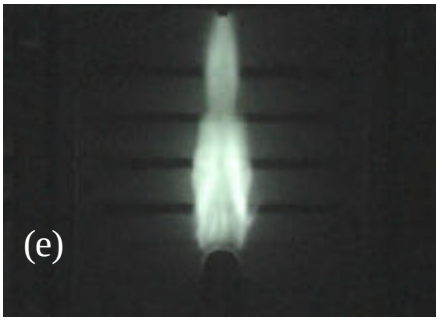

(9) t = 95 ms

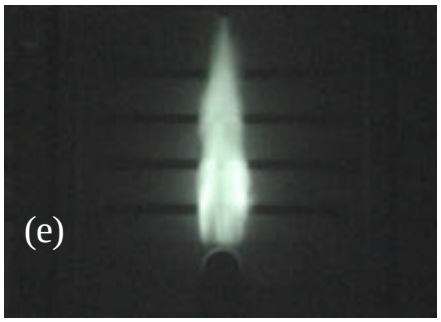

(6) t = 42 ms

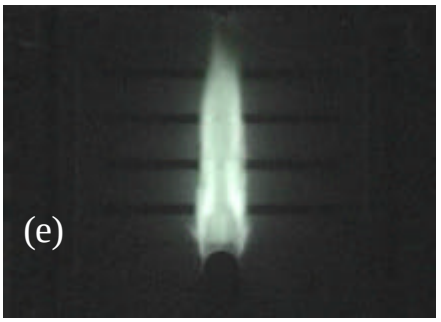

(10) t = 1 sec

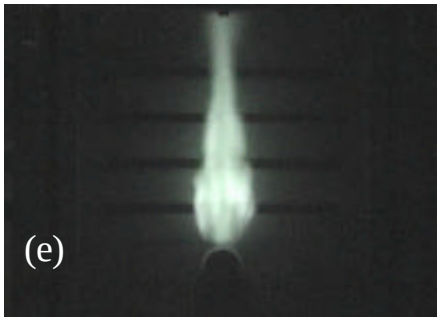

(7) t = 63 ms

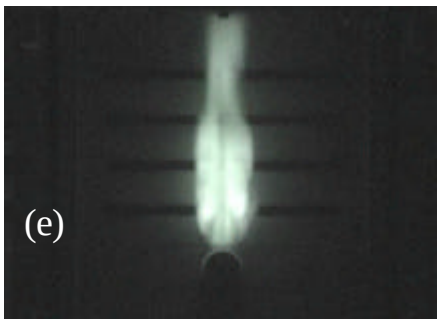

(8) t = 77 ms

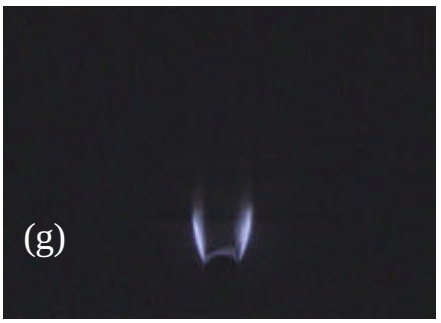

FIGURE 37 Series of flame configurations as a function of inflow velocity (v_w = 3.02cm/s and S = 180°), (a) U_{in} = 0.41m/s, (b) U_{in} = 0.62m/s, (c) U_{in} = 0.71m/s, (d) U_{in} = 1.00m/s, (e) U_{in} = 1.39m/s (Night shot photos), (f) U_{in} = 1.43m/s, and (g) U_{in} = 3.00m/s

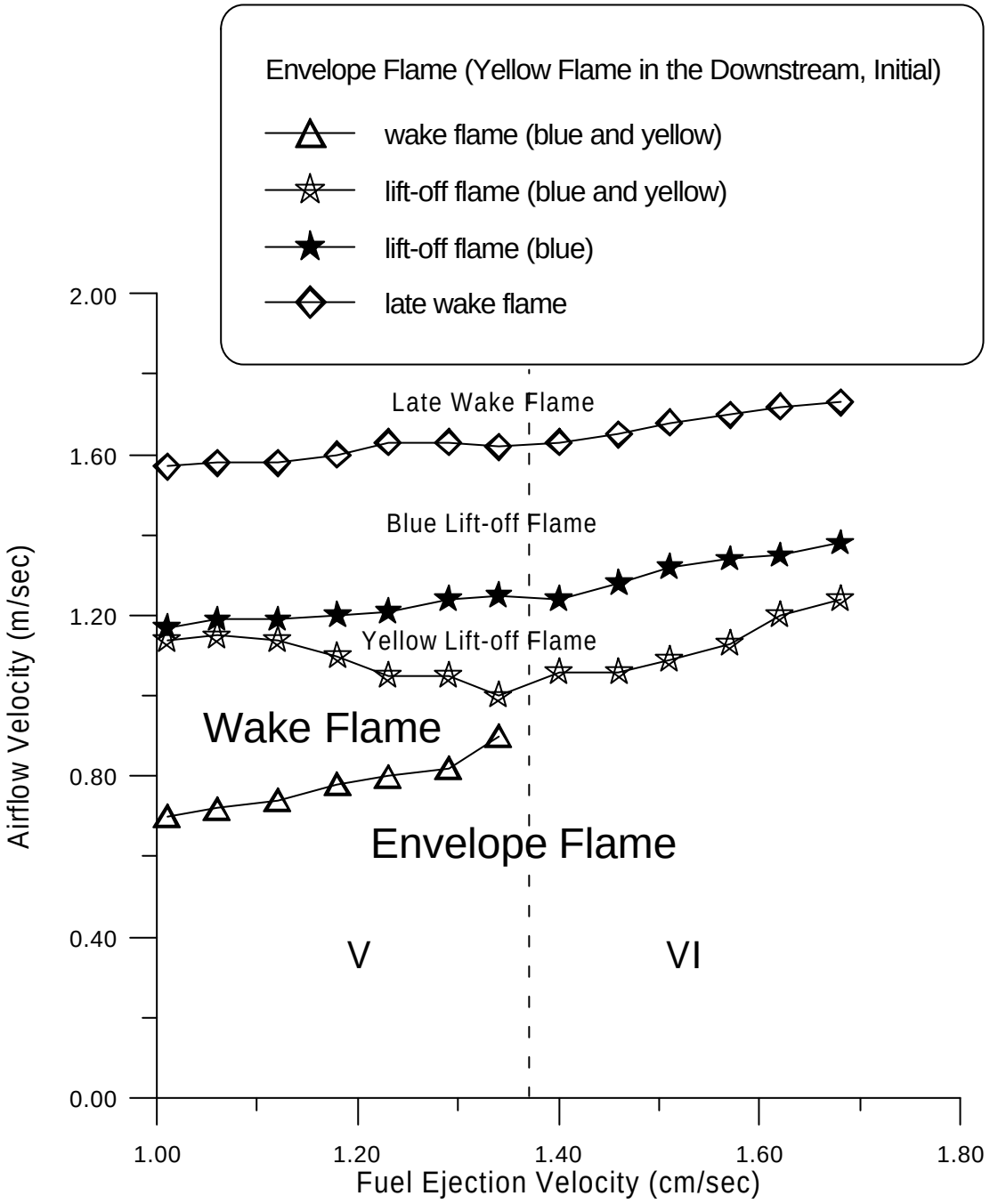

FIGURE 38 Various flame stabilization regions over a burner (S=360°)

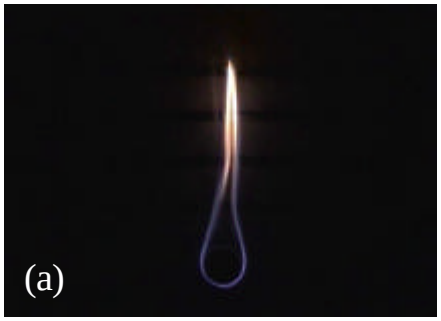

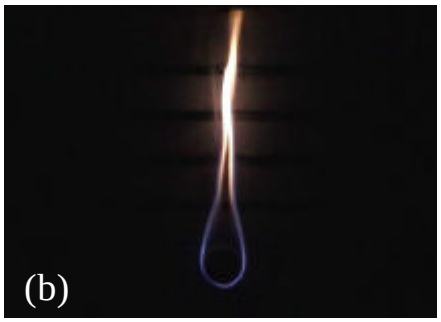

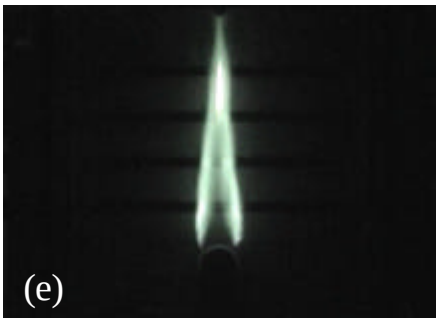

(1) t = 0 sec

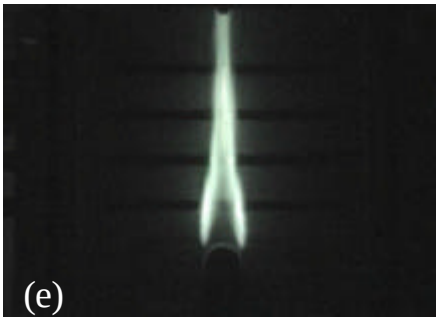

(2) t = 4 ms

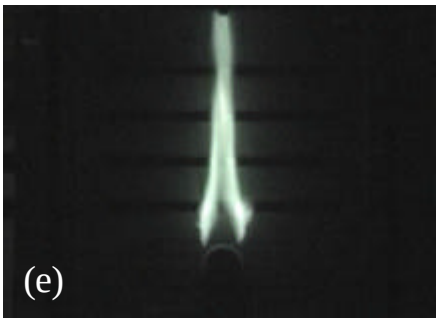

(3) t = 28 ms

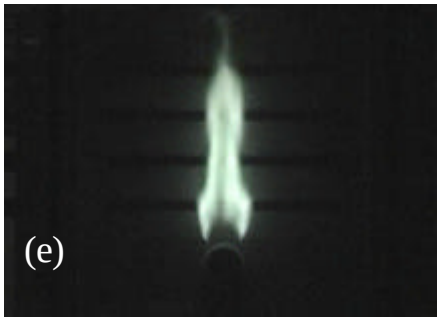

(4) t = 77 ms

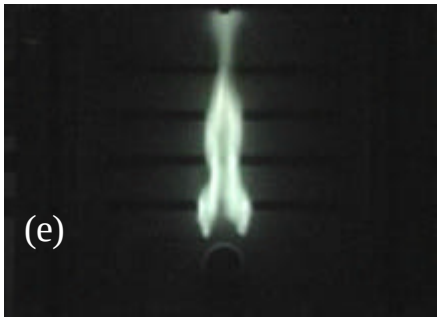

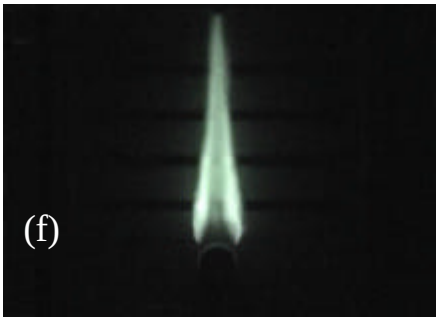

(5) t = 109 ms

Night shot photo

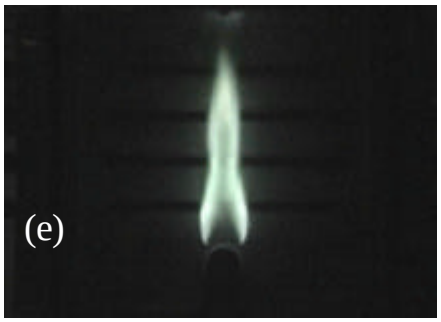

(6) t = 116 ms

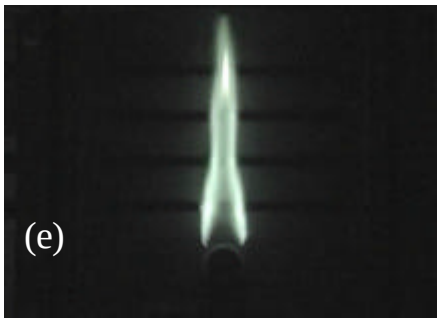

(7) t = 123 ms

FIGURE 39 Series of flame configurations as a function of inflow velocity (v_w = 1.23cm/s and S=360°), (a) U_{in} = 0.41m/s, (b) U_{in} = 0.51m/s, (c) U_{in} = 0.80m/s, (d) U_{in} = 1.00m/s, (e) U_{in} = 1.05m/s (Night shot photos), (f) U_{in} = 1.21m/s and, (g) U_{in} = 1.63m/s

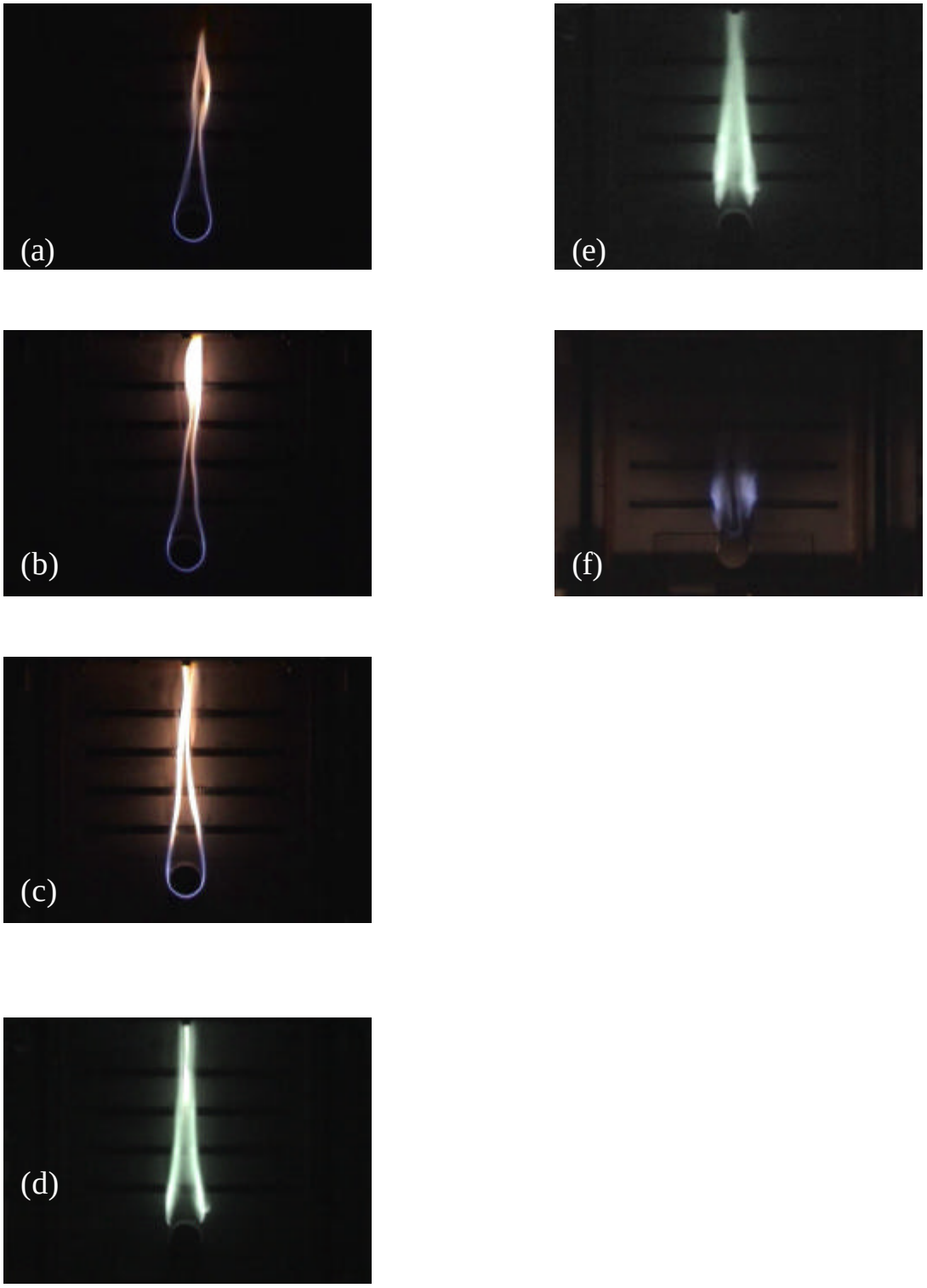

FIGURE 40 Series of flame configurations as a function of inflow velocity (v_w = 1.4cm/s and S=360°), (a) U_{in} = 0.41m/s, (b) U_{in} = 0.51m/s, (c) U_{in} = 0.84m/s, (d) U_{in} = 1.06m/s (Night shot photo), (e) U_{in} = 1.24m/s (Night shot photo), and (f) U_{in} = 1.63m/s

(1)

(2)

(3)

(4)

FIGURE 41 The transient oscillation photos of lift-off flame in U_{in} = 1.03m/sec and v_w = 1.12cm/sec (The number 1, 2, 3, and 4 represent the time sequence.) (Left photos are normal ones and right photos are night shot ones.)

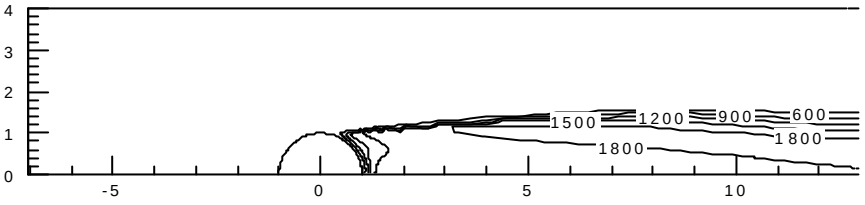

t = 0.065 sec

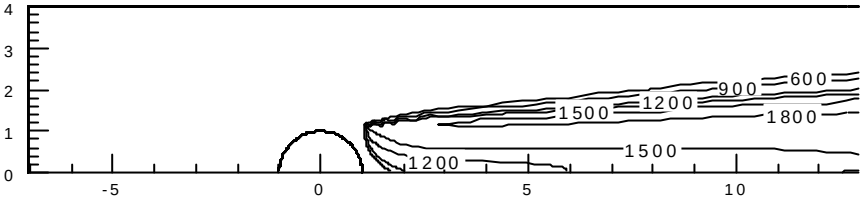

t = 0.07 sec

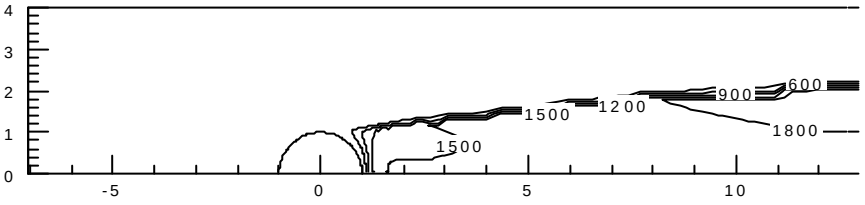

t = 0.075 sec

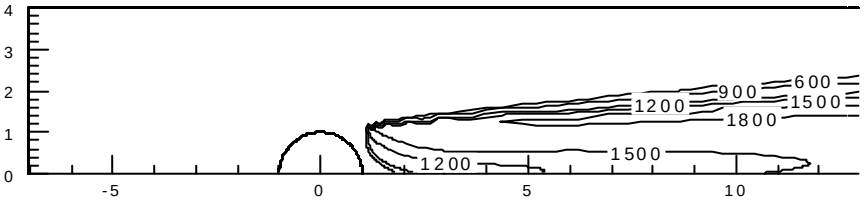

t = 0.08 sec

FIGURE 42 The predicted temperature contours of transient lift-off flame in U_{in} = 1.03m/sec and v_w = 1.12cm/sec (Unit: K)